Fakultät für Medizin

Institut für Molekulare Immunologie

Stat3 Prevents Mitophagy and Lysosomal Membrane Permeabilization in Intestinal Epithelial Cells to Suppress Adaptive Immunity during Tumorigenesis

Paul Konrad Ziegler

Vollständiger Abdruck der von der Fakultät für Medizin der Technischen Universität München zur Erlangung des akademischen Grades eines

Doctor of Philosophy (Ph.D.)

genehmigten Dissertation.

Vorsitzende: Prof. Dr. Agnes Görlach
Betreuer: Prof. Dr. Florian R. Greten

Prüfer der Dissertation:

1. Prof. Dr. Bernhard Holzmann
2. Prof. Dr. Thomas Korn
3. Prof. Dr. Thomas Kirchner

Die Dissertation wurde am 07.11.2018 bei der Fakultät für Medizin der Technischen Universität München eingereicht und durch die Fakultät für Medizin am 25.02.2019 angenommen.

Parts of the present work have been published in:

Ziegler, P. K., Bollrath, J., Pallangyo, C. K., Matsutani, T., Canli, Ö., De Oliveira, T., ... Greten, F. R. (2018). Mitophagy in Intestinal Epithelial Cells Triggers Adaptive Immunity during Tumorigenesis. **Cell**, 174(1), 88–10116.

Believe those who are seeking the truth. Doubt those who find it.

André Gide

Table of Contents

List of Figures

Abstract

Colorectal cancer is one of the leading causes of cancer-related death in humans. The presence of cytotoxic T cells within the tumor stroma is associated with a favorable prognosis, however, little is known about the underlying biology of T cell recruitment and activation by tumor cells. One potential therapeutic strategy for activation of anti-tumor immunity is to stimulate the antigen-presentation by tumor cells, marking these as potential targets for T cells. Using two mouse models of the Wnt-driven "classical pathway of colon tumorigenesis" we have identified a previously unrecognized pathway linking tumor cell metabolism and anti-tumor immunity. Experimental inhibition of the protein STAT3 in intestinal epithelial cells increases mitochondrial turnover by the autophagic-lysosomal pathway, which results in iron-accumulation in lysosomes, protease-rich organelles within the cells. Subsequently, lysosomes release proteases into the cytosol of the cells, which in turn triggers enhanced antigen-presentation. These antigens can be transferred onto Dendritic cells, cells of the immune system highly specialized in activating T cells, by a process termed cross-dressing. This results in enhanced activation of T cells against tumor cells, thus mitigating or abrogating tumorigenesis. In addition, we demonstrate the efficacy of pharmacological targeting of this pathway and we verified the negative correlation between STAT3 activation and presence of cytotoxic T cells in human patient specimen. Taken together, this work describes a previously unrecognized mechanism in anti-tumor-immunity and demonstrates its potential as a future therapeutic strategy in cancer treatment.

Zusammenfassung

Darmkrebs ist eine der häufigsten Krebserkrankungen des Menschen und für viele Todesfälle verantwortlich. Eine bessere Prognose haben Patienten mit hoher Dichte an zytotoxischen T Zellen innerhalb des Tumorgewebes, allerdings ist noch wenig über die biologischen Mechanismen bekannt, die zur Infiltration und Aktivierung von T Zellen in Krebsgewebe führen. In unserer Studie haben wir in zwei unterschiedlichen Mausmodellen für die Entstehung von Darmkrebs einen bisher unbekannten Mechanismus gefunden, der Stoffwechsel und Immunogenität von Tumorzellen verbindet. Durch experimentelle Inaktivierung des Proteins STAT3 in Darmepithelzellen während der Tumorentwicklung wird die Aktivität von Mitochondrien und deren Abbau durch Autophagie und Lysosomen, Zellorganellen reich an Proteasen, verstärkt. Dies führt zu einer Eisenüberladung der Lysosomen, die daraufhin ihre Proteasen ans Zytoplasma der Zellen abgeben, was wiederum die Antigen-Präsentation erhöht. Über einen als „cross-dressing“ bekannten Mechanismus können diese Antigene daraufhin an Dendritische Zellen übertragen werden, Zellen des Immunsystems spezialisiert auf die Aktivierung von T Zellen. Diese wirken daraufhin effektiv gegen Tumorzellen, was die Entstehung von Tumoren verzögert oder unterdrückt. Darüber hinaus zeigen wir, dass man diesen Mechanismus durch pharmakologische Substanzen nutzen kann und weisen die negative Korrelation von STAT3-Aktivierung und der Präsenz von T Zellen in Patientenproben nach. Zusammengefasst stellt diese Arbeit einen zuvor unbekannten Mechanismus der Tumorimmunität vor und zeigt seine mögliche Nutzung in der Krebstherapie auf.

Abbreviations

AOM	Azoxymethane
APC	Adenomatous polyposis coli
APC	Allophycocyanin
ATP	Adenosine triphosphate
BM	Bone marrow
c.a.	Constitutive active
CMS	Consensus molecular subtype
CRC	Colorectal cancer
DC	Dendritic cell
DAB	3, 3 -Diaminobenzidine
DAPI	4’,6-Diamidino-2-phenylindole
DFO	Deferoxamine
DMEM	Dulbecco's modified Eagle's medium
DTR	Diphteria toxin receptor
DTT	Dithiothreitol
EDTA	Ethylenediaminetetraacetic acid
EGTA	Ethylene glycol-bis(β-aminoethyl ether)-N,N,N’,N’-tetraacetic acid
EMT	Epithelial-mesenchymal transition
ERK	Extracellular signal-regulated kinases
FAP	Familial adenomatous polyposis
FCCP	Carbonyl cyanide-p-trifluoromethoxyphenylhydrazone
FITC	Fluorescein isothiocyanate
HIF1α	Hypoxia-inducible factor 1α
HPF	High-power field
IEC	Intestinal epithelial cell
IF	Immunofluorescence staining
IHC	Immunohistochemistry
JNK	c-Jun N-terminal kinases
MAPK	Mitogen-activated protein kinases
MFI	Mean fluorescence intensity
MHC	Major histocompatibility complex
MYC	Myelocytomatosis
OCR	Oxygen consumption rate
OVA	Chicken ovalbumin
PBS	Phosphate-buffered saline
PCR	Polymerase chain reaction
PE	R-phycoerythrin
PKCδ	Protein kinase Cδ
RIPA	Radioimmuno precipitation assay
scr	scrambled

SSA	Sessile serrated adenoma
TAP	Transporter associated with antigen-presentation
TCR	T cell receptor
TMRM	Tetramethylrhodamin-Methylester
TP53	Tumor suppressor p53
WCE	Whole cell extracts
WHO	World Health Organization
WT	Wildtype

1 Introduction

In 2012, 1,36 Million people worldwide were diagnosed with colorectal cancer (CRC) (WHO, 2014b) and about 700.000 women and men died from this disease (WHO, 2014c). These figures make CRC the third most frequent cancer worldwide accounting for 8,5 % of all cancer related deaths on a worldwide basis (WHO, 2014a) – a figure expected to rise to 10,3 % in 2030 (Forum and Health, 2011).

1.1 Biology of Colorectal Cancer

Consistent with its barrier function between the organism and food and microbes, the epithelial layer of the intestine undergoes a turnover on a weekly basis (turnover-time 4-6 days in mice and humans) (Barker et al., 2008). In order to maintain homeostasis within the tissue, intestinal epithelial cells are organized in a highly hierarchical system, with the intestinal stem cell compartment on top (Medema and Vermeulen, 2011). These stem cells located at the bottom of the crypt of Lieberkühn give rise to cells of various differentiation, including enterocytes specialized in absorbing nutrients, goblet cells mainly producing mucins and Paneth cells as a key source of anti-microbial proteins and factors critical for maintaining the stem cell niche within the crypt. The high proliferative activity together with environmental factors, including the presence of inflammatory cells in the intestinal wall, is probably the underlying reason for the frequent formation of neoplasms in the colon and rectum (Tomasetti et al., 2017).

1.1.1 *Aberrant Wnt-Signaling as the Early Molecular Driver in CRC*

On a molecular basis, the key driver of renewal of intestinal epithelium is the Wnt signaling pathway. This multicomponent pathway integrates the signaling of Wnt-ligands, cytokines that act as the main driver for intestinal stem cell division and

regeneration. In the absence of activating ligands binding to the cell surface, the protein APC promotes the phosphorylation and subsequent proteasomal degradation of the proto-oncogene β-Catenin. Binding of Wnt ligands to their receptor Frizzled on the outer surface of the cell result in inhibition of β-Catenin phosphorylation and degradation, therefore stochastically promoting the translocation of β-Catenin to the nucleus, where it can interact with the transcription factor TCF (T cell factor) to promote the expression of a number of target genes, including *CMYC*, *CCND1* (encoding CYCLIN D1), and many more (Figure 1.1).

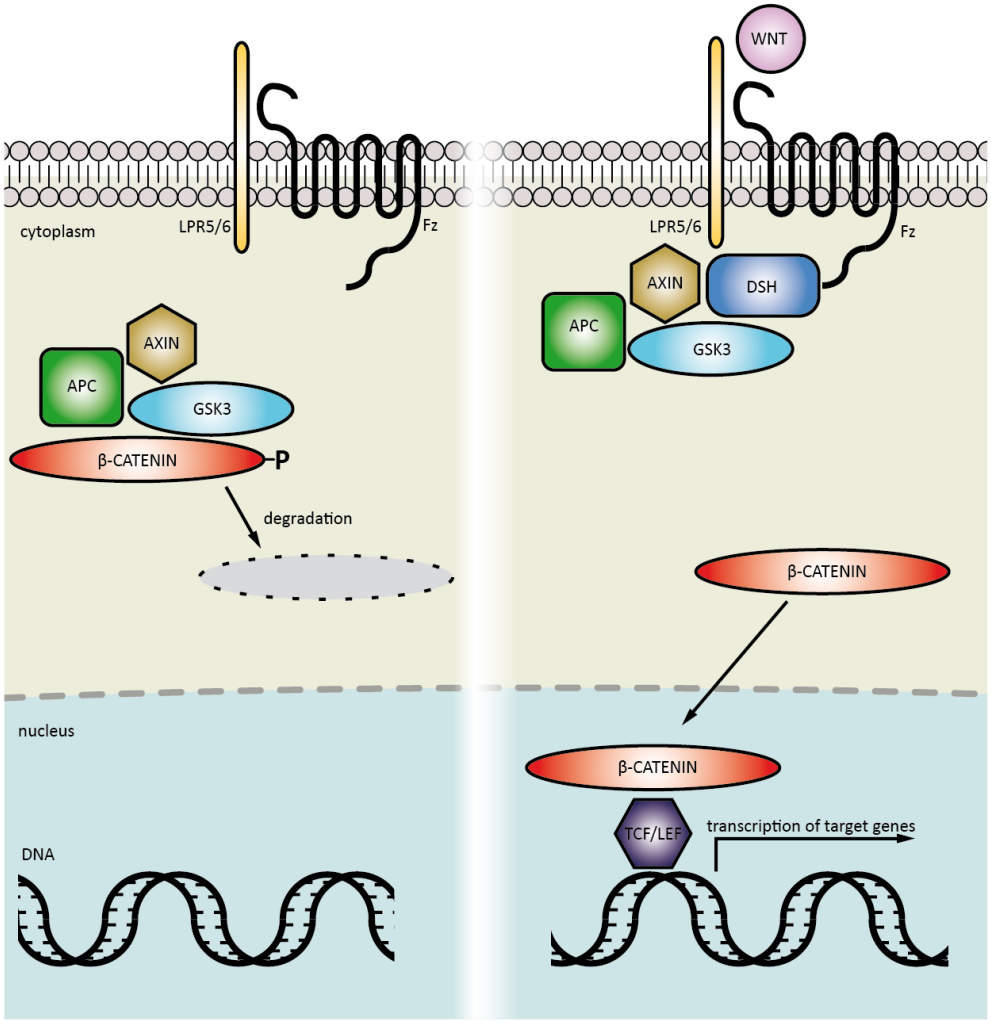

Figure 1.1: Wnt Signaling. In absence of Wnt-ligands, β-Catenin is being marked to degradation by phosphorylation by a multiprotein-complex (left). Upon binding of Wnt-ligands to their extracellular receptor Frizzled (Fz), the multiprotein-complex disintegrates and β-Catenin translocates to the nucleus, where it activates the transcription of target genes (right). Adapted from (Ziegler and Greten, 2015).

1.1.2 *Genetics of Colon Carcinogenesis*

The intestinal epithelium frequently develops protruding lesions termed polyps of various biological characteristics and histological appearance, including adenomatous polyps, hyperplastic polyps, traditional serrated adenomas (TSA), sessile serrated adenomas (SSA) and inflammatory polyps, among others. Adenomatous polyps are currently widely accepted as the main precursor lesion of CRC. Adenomas are characterized by dysplastic morphology and altered differentiation of epithelial cells (Fearon, 2011). Genetic analyses have revealed a high proportion (70-80%) of adenomas to harbor mutations in the *APC* gene, an 8.5 kb gene in the 5q21-22 locus (Fearon, 2011; Fearon and Vogelstein, 1990).

While most *APC* mutations appear to be of sporadic nature, FAP (familial adenomatous polyposis) patients harbor hereditary mutations in the *APC* gene. Affected individuals develop hundreds or thousands of adenomas throughout the colon and rectum, and eventually develop cancer unless their colon and rectum is removed by surgery. Numerous different mutations in that locus have been identified, however, frameshift mutations caused by deletions of the nucleotides 3183-3187 (ACAAA) or 3926-3930 (AAAAG) are most frequent and account for 11 and 17% of all germline mutations, respectively (Groden et al., 1993). Those codons are also frequently mutated in sporadic CRC cases (Fearon, 2011). The finding that *APC* mutations underlie adenoma formation in most cases has led to the nowadays widely accepted model of stepwise CRC development by the "adenoma-carcinoma sequence": Following the initial alterations in the Wnt pathway, dysplastic cells eventually acquire mutations of *KRAS* and *TP53*, among others, before displaying full malignant potential (Fearon, 2011; Fearon and Vogelstein, 1990; Vogelstein et al., 1988) (Figure 1.2). In addition to *APC* mutations, other genes critical for the

regulation of Wnt signaling have been identified as driver mutations for adenoma formation, such as *CTNNB1* (encoding β-Catenin) in approx. 8% of the cases investigated (Cancer Genome Atlas, 2012).

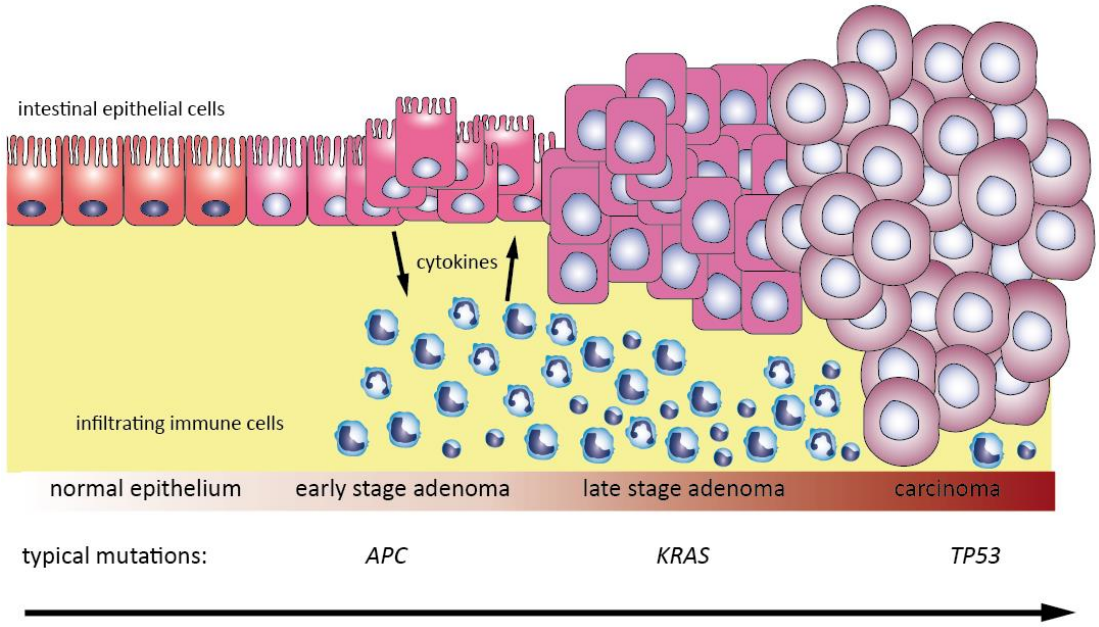

Figure 1.2: Adenoma-Carcinoma Sequence. Schematic depiction of the development of colorectal cancer from precursor lesions with stepwise acquisition of mutations. Adapted from (Ziegler and Greten, 2015).

In addition to the "classical adenoma-carcinoma sequence" arising from adenomatous polyps, other histological types of polyps can progress into tumors as well. Sessile serrated adenomas (SSA) are known to develop into cancer by the so-called "serrated pathway of neoplasia", named according to their unusual histological "serrated" appearance. Approximately 80% of SSA harbor mutations in the *Braf* proto-oncogene, while in hyperplastic polyps or traditional serrated adenomas *Kras* mutations are common as well (Chan et al., 2003; Yang et al., 2004). Serrated neoplasia is over-represented in the right-sided colon and accounts for up to 17% of neoplasms arising in that location according to a study (Noffsinger, 2009).

1.1.3 *Microenvironmental Factors in CRC Development*

Apart from genetic changes, tumor cells depend on the close interaction with their microenvironment (Grivennikov et al., 2010). Together with genomic instability, tumor promoting inflammation is nowadays being regarded as the "enabling characteristic" that enables the acquisition of further features dubbed "hallmarks of cancer" that allow cancer cells to survive, proliferate, and disseminate (Hanahan and Weinberg, 2011). One of the most important risk-factor to develop CRC is chronic inflammation in the colon as demonstrated by the finding that a longstanding history of chronic inflammation in colon and rectum increases the risk of developing CRC to 20 % after 30 years (Eaden et al., 2001). In addition, activation of key inflammation-linked transcription factors or alterations of the intestinal microbiome has been shown to fuel tumor development by affecting the genomic stability, EMT or the differentiation state of IEC (Schulz et al., 2014; Schwitalla et al., 2013a; Schwitalla et al., 2013b).

In addition, bioinformatic analyses have been used to group CRC cases by so-called consensus molecular subtypes (CMS) (Guinney et al., 2015). Four distinguished subtypes have been identified as following: (I) CMS1 termed "microsatellite instability immune", detected in 14% of CRC cases, is characterized by hypermutated, microsatellite unstable tumor cells exerting strong immune activation; (II) CMS2 ("canonical", 37% of CRC cases) with tumor cells showing marked WNT and MYC signaling activation; (III) CMS3 ("metabolic", 13%) consists of tumors with epithelial polarization, frequent activation of MAPK signaling and metabolic dysregulation; and (IV) CMS4 ("mesenchymal", 23%) comprises of tumors with pronounced activation of transforming growth factor-β, stromal invasion and angiogenesis. These findings demonstrate the remarkable heterogeneity of CRC in

both genetic and microenvironmental factors and their interdependence. Stratification of patients along those groups might be useful for future CRC therapy.

1.2 STAT3 as a Key Transcription Factor in CRC

Originally described in hepatocytes as a component of the acute phase response in inflammation, the STAT3 signaling pathway has been recognized as a major driving factor in tumorigenesis and its activation in a variety of tumors including CRC has been shown (Bollrath and Greten, 2009). STAT3 is activated by various cytokines including the IL-6 family of cytokines, comprised of IL-6, IL-11, ciliary neurotrophic factor (CNTF), leukemia inhibitory factor (LIF), oncostatin M (OSM), cardiotrophin 1 (CT-1), cardiotrophin-like cytokine (CLC), and IL-27 (Rose-John, 2018); members of the IL-10 protein family (Hutchins et al., 2013) and various growth factors, including hepatocyte growth factor (HGF), epidermal growth factor (EGF) and platelet derived growth factor (PDGF). Furthermore, non-receptor tyrosine kinases as SRC or ABL can as well promote the activation of STAT3 (Levy and Lee, 2002) (Figure 1.3).

1.2.1 *Activation of STAT3 Signaling*

Prototypically, cytokines of the IL-6 family transduce their signals through interactions of a cytokine specific receptor (membrane bound, or as in case of IL-6R-trans-signaling, as a soluble protein) with the transmembrane protein GP130. Upon receptor interaction, GP130 interacts with intracellular JAK proteins (most notably JAK1, JAK2 and TYK2), which in turn phosphorylate the Y705-domain of STAT3. This results in homodimerization of STAT3 proteins and their translocation to the nucleus, where they interact with DNA and bind to the promoter regions of target genes (Heinrich et al., 2003) (Figure 1.3).

In addition to the Y705 residue of STAT3, phosphorylation has been detected at the S727-residue of STAT3 as well. This appears to be the result of receptor engagement by various growth factors, such as EGF, and signal transduction via the ERK-, p38-, JNK- or PKCδ-pathways (Decker and Kovarik, 2000).

Target genes of STAT3 signaling in tumorigenesis include genes involved in cell cycle regulation (*c-Myc*, genes encoding Cyclin D1, Cyclin E,), apoptosis (Bcl-xL, Bcl-2, Survivin), EMT (Twist, Zeb1) and matrix remodeling (MMP-2 and -9) (Carpenter and Lo, 2014). In contrast, expression of dominant negative Stat3 in cancer cell lines increased the expression of pro-inflammatory cytokines including TNFα, IL-6, CCL5, CXCL10 and IFN-β (Wang et al., 2004), suggesting a role of the STAT3 signaling pathway in immune activation by tumors as well.

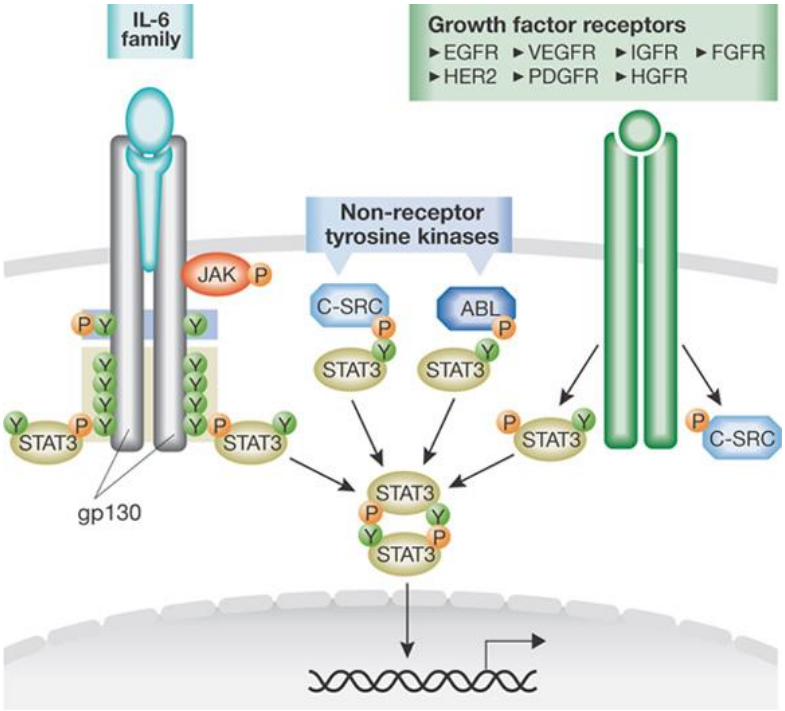

Figure 1.3: STAT3 Signaling. Upon ligand binding, GP130 interacts with of cytokine-specific receptors which causes dimerization, recruitment of JAK kinases and subsequent phosphorylation of the Y705-domain of STAT3. Dimerized STAT3 proteins translocate to the nucleus and activate the transcription of target genes. Taken from (Bollrath and Greten, 2009).

1.2.2 *STAT3 Signaling in Cancer*

The functional consequences of STAT3 signaling in tumorigenesis have been demonstrated in a mouse model of colitis-associated cancer: In case of conditional deletion of *Stat3* in IECs carcinogenesis has been markedly attenuated, while overactivation of STAT3 by introduction of a point-mutation in *Gp130* that blocks the binding of the natural STAT3-signaling inhibitor SOCS3, showed the opposite phenotype with enhanced tumorigenesis (Bollrath et al., 2009). Similar effects have been described for IL-6- and IL-11-signaling, with the latter seem to play a dominant role in colitis-associated cancer (Grivennikov et al., 2009; Putoczki et al., 2013).

Mechanistically, this study has identified STAT3 as a critical mediator of interaction between infiltrating inflammatory cells, especially of the myeloid lineage, and early stage tumor cells (Bollrath et al., 2009): Chemokine production by neoplastic epithelial cells drives the infiltration and activation of myeloid cells, and these produce factors like IL-6, IL-11, IL-1 or TNF-α, which in turn activate key pro-survival and pro-proliferation pathways in tumor cells, most notably the NF-κB- and STAT3-pathway, and enhance the expression of genes encoding e.g. Bcl-xL, Survivin, Cyclin D1 and RegIIIb (Figure 1.4).

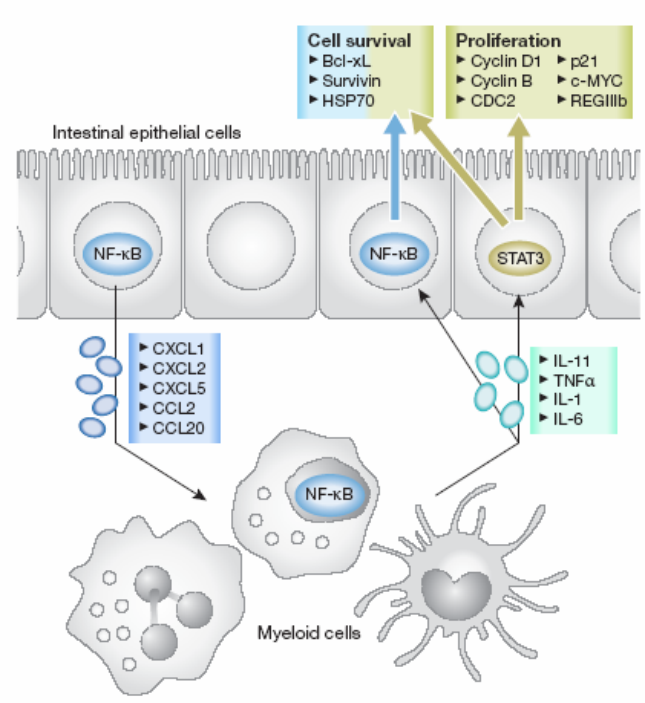

Figure 1.4: Tumor Microenvironment Promotes Tumorigenesis. Chemokines from tumor cells attract and activate infiltrating myeloid cells. Their cytokines in turn activate key pro-tumorigenic pathways in tumor cells. Taken from (Bollrath and Greten, 2009).

1.3 Tumor Cell Metabolism

Energy metabolism in mammalian cells consists of two distinct katabolic pathways, glycolysis and oxidative phosphorylation, the latter depending on mitochondrial activity. In glycolysis one molecule of glucose is metabolized to two molecules of pyruvate, yielding the equivalent of two molecules of ATP as intracellular energy carrier. In order to regenerate the thereby oxidized NADH molecules, pyruvate can be oxidized to lactate, which is routinely excreted from the cell. Under aerobic conditions pyruvate can be transported into the mitochondrial matrix where it is metabolized to acetyl-CoA and subsequently degraded in a stepwise process termed Krebs' cycle. Thereby, multiple electrons as energy equivalents of biochemical processes are transferred via NADH and $FADH_2$ to the enzyme complexes of the respiratory chain, which results in highly efficient energy metabolism compared to glycolysis (Lehninger et al., 2008) (Figure 1.5).

1.3.1 *Aerobic Glycolysis of Tumor Cells*

Since its discovery in 1924, the Warburg effect (Figure 1.5) describes the lack of mitochondrial respiration in cancer cells and their dependency on glycolysis despite availability of oxygen (Warburg et al., 1924). The initial observation has been reproduced in a variety of tumors and aerobic glycolysis is considered to be a hallmark of cancer cell metabolism (Hanahan and Weinberg, 2011; Moreno-Sanchez et al., 2007; Pavlova and Thompson, 2016). Moreover, this effect has fueled the development of ^{18}F-FDG-PET imaging widely used in cancer diagnostics (Monakhov et al., 1978; Som et al., 1980). Even though extensively studied in a variety of model systems its underlying biology remains largely unknown.

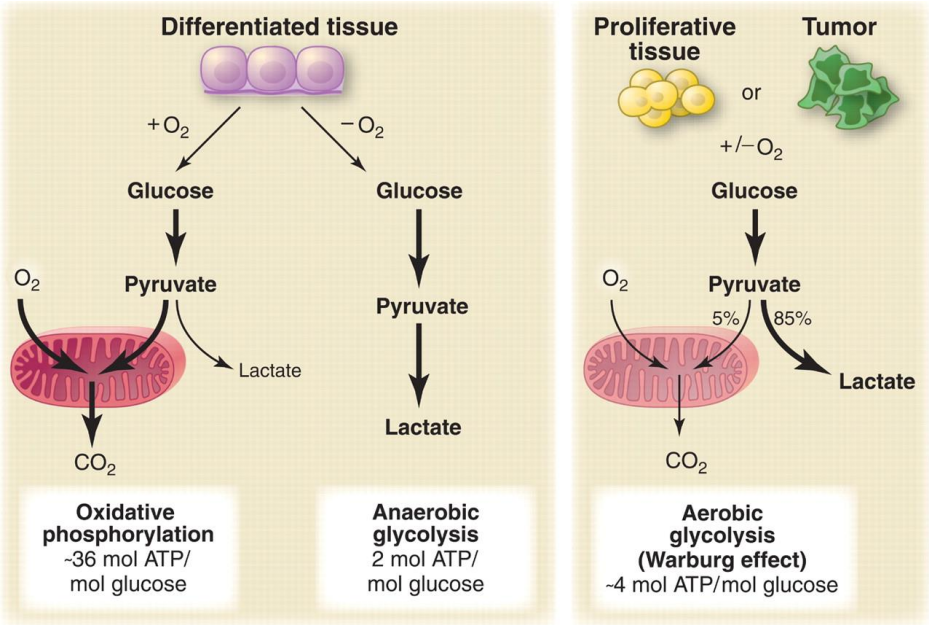

Figure 1.5: Energy Metabolism. Schematic depiction of oxidative phosphorylation, anaerobic glycolysis, and aerobic glycolysis (Warburg effect). Cells metabolize glucose to pyruvate via glycolysis, that results in pyruvate production. Under aerobic conditions differentiated (non-proliferating) use pyruvate as a substrate for oxidative phosphorylation, where oxygen is required as electron acceptor. Under anaerobic conditions cells can produce lactate from pyruvate thus recycling (reducing) 2 NADH molecules produced during glycolysis back to NAD^+. This process is very inefficient as it only produces 2 equivalents of ATP per glucose molecule in contrast to the (theoretical) 36 equivalents of ATP during oxidative phosphorylation (left). The Warburg effect describes the observation that cancer cells like (healthy) proliferating cells under aerobic conditions use most glucose for lactate production (aerobic glycolysis). In parallel, some oxidative phosphorylation continues in both cancer cells and normal proliferating cells (right). Taken from (Vander Heiden et al., 2009).

To date, several hypotheses on the fundamentals of the Warburg effect have been proposed, such as (I) tumor cells have irreversibly damaged mitochondrial enzymes (Warburg, 1956), (II) tumor cells use aerobic glycolysis in order to gain a comparative growth advantage over non-malignant cells nearby by "intoxicating" them with lactic acid (Gatenby and Gillies, 2004) or (III) metabolic reprogramming is used to evade mitochondrial cell death pathways (Gogvadze et al., 2008). Furthermore, it has been observed that aerobic glycolysis is not restricted to cancer cells but can also be observed in proliferating cells like T cells (Brand and Hermfisse, 1997; Lunt and Vander Heiden, 2011).

Therefore, in a current hypothesis (IV) it has been proposed that glycolysis should be viewed as a key part of complex anabolic metabolism of proliferating cells including cancer cells rather than a pathway to simply provide energy (ATP). In addition, several oncogenes or tumor suppressors commonly involved in cancer have been linked to metabolic reprogramming of tumor cells, like RAS, MYC, AKT, TP53 and the key regular of cellular response to hypoxia HIF1α (Hanahan and Weinberg, 2011; Pavlova and Thompson, 2016).

1.3.2 *Role of STAT3 in Metabolism*

In a study using mouse embryonic fibroblasts (MEFs) expression of constitutive active Stat3 mutant (Stat3C) induced a HIF-1α-dependent metabolic switch towards aerobic glycolysis (Demaria et al., 2010). This effect was demonstrated by increased expression of glycolysis-linked genes *Pdk1*, *Glut1*, *Pfkl*, *Eno1*, increased uptake of glucose, increased production of lactate and reduced mitochondrial activity. Treatment with the glycolysis-inhibitor 2-deoxyglucose (2-DG) increased cell death, demonstrating the dependency of cells on aerobic glycolysis.

Furthermore, serine-phosphorylated STAT3 has been found to regulate mitochondrial activity independent from DNA binding (Gough et al., 2009; Wegrzyn et al., 2009). pS727-STAT3 was required for enzymatic activity of complex I and II of the respiratory chain in cardiomyocytes and MEFs, or complex II and V in RAS-transformed tumor cells. These results demonstrate the importance of STAT3 for mitochondrial function as well as the context sensitivity of its actions.

1.4 Tumor Immunity

First hypothesized by Paul Ehrlich more than 100 years ago (Ehrlich, 1909), the importance of the immune system in controlling tumor growth is nowadays widely accepted. The immune system can be grouped into innate and adaptive immunity that cooperate in order to maintain host integrity and defend the organism against internal and external threats. Growing tumors in cancer patients can elicit a protective immune response, however, this immune response attenuates tumor growth to a degree highly variable between individuals (Fridman et al., 2011).

Cytotoxic T cells are being regarded as key components of anti-tumor immunity (Grivennikov et al., 2010). Infiltration of $CD8^+$ T cells into and increased *IFNG* expression within the tumor tissue have been found to confer a survival advantage to patients suffering from CRC (Figure 1.6), whereas high expression levels of IL-17a is linked to a poor survival (Galon et al., 2006; Tosolini et al., 2011). These findings highlight the importance of tumor-infiltrating T cells as well as demonstrate their remarkably variable biology. The clinical correlation between T cell infiltration and prognosis has resulted in the development of an immune score that can be employed to predict survival of CRC patients (Fridman et al., 2012), however, little is known

about the underlying cellular and molecular mechanisms resulting in T cell recruitment, activation and polarization in colorectal tumors.

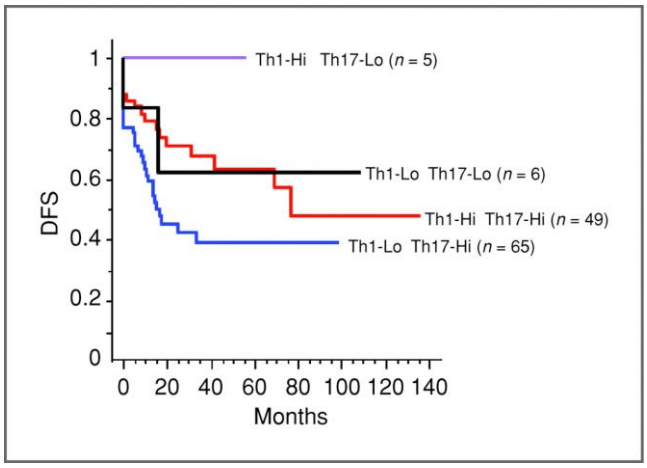

Figure 1.6: Prognosis of CRC Patients Depends on the Adaptive Immune System. Disease free survival (DFS) of colorectal cancer patients stratified according to the expression level of the gene from the Th1 cytotoxic gene cluster including *GZMB*, *CD8A*, *STAT1*, *IFNG* in combination with the genes from Th17 gene cluster including *RORC*, *IL17A*. Taken from (Tosolini et al., 2011)

1.4.1 *Activation of T Cells*

T cells are a central part of the adaptive immune system. They originate from lymphoid precursor cells in the bone marrow and mature in the thymus. Dependent on their surface marker expression, T cells can be divided into $CD4^+$ and $CD8^+$ cells. For activation, T cells usually require 3 distinct signals:

(I) Interaction of their T cell receptor (TCR) with their respective target antigen presented by MHC-I or -II.

(II) Binding of the CD28-receptor on their surface to either CD80 (B7.1) or CD86 (B7.2). These have been termed “co-stimulatory molecules” and are typically found on the surface of activated Dendritic cells (DC).

(III) In order to become fully activated, T cells require stimulation by inflammatory cytokines. IL-12, type-I interferons and IL-1-family cytokines have been identified to activate $CD8^+$ T cells (Cox et al., 2013; Freeman et al., 2012).

$CD4^+$ T cells have been termed helper T cells (T_h) and recognize antigen bound to MHC-II molecules on the surface of DC and other so-called antigen-presenting cells. Upon antigen contact T_h cells undergo a differentiation process depending on the cytokine milieu. So far, at least 7 different helper T cell subtypes have been identified (Golubovskaya and Wu, 2016). Each subtype is characterized by a specific cytokine profile that is released upon activation, most notably IFNγ released by T_h1, IL-4 by T_h2 and IL-17 by T_h17 cells. $CD4^+$ T cells also consist of regulatory T cells (T_{reg}) characterized by the expression of *Foxp3* and production of IL-10 and TGF-β, important mediators of immunotolerance. T_h cells functionally regulate immune reactions by controlling most other components of the immune system, including leukocyte trafficking, antibody production, activation of granulocytes and macrophages, antigen presentation, etc.

$CD8^+$ T cells have been termed cytotoxic T cells due to their ability to directly induce apoptosis in target cells. They interact with antigens bound to MHC-I molecules present on all cells of the organism (except erythrocytes) and produce cytokines like IFNγ, which is a potent activator of macrophages, stimulates antigen presentation and lymphocyte infiltration (Boehm et al., 1997). Furthermore, IFNγ can induce the expression of negative cell cycle regulators like p21 and p27 in cancer cells (Mojic et al., 2017). Apoptosis in target cells is induced by perforin and granzyme proteins: Perforin integrates into the plasma membrane of a target cell and builds pores for granzymes, serine proteases that selectively cleave pro-caspases or the pro-apoptotic protein BID (Voskoboinik et al., 2015). These properties make them a potential tool against cancer.

1.4.2 *Generation of T Cell Diversity*

T cells represent a highly heterogenous population of cells in mammalian organisms. They are characterized by the expression of a heterodimeric protein complex known as T cell receptor (TCR) on their surface. In most T cells the TCR consists of two subunits, the α- and the β-chain. TCR-αβ together with CD4 or CD8 molecules mediate the interaction of T cells with MHC-molecules on neighboring/target cells (Kindt et al., 2007), and the surface molecule CD3 acts as signal transducing element. A minority of T cells express TCR consisting of a γ-and δ-chain, whose ligand(s) remain elusive.

The TCRα locus contains C, V and J gene segments (Cα, Vα and Jα). The TCRβ locus, contains D gene segments (Dβ) in addition to Cβ, Vβ and Jβ gene segments. During T cells maturation in the thymus, the TCR gene loci undergo a rearrangement mediated among others by RAG1 and RAG2 proteins: In the TCR alpha locus, one Vα gene segment rearranges to one Jα gene segment to create a functional V-region exon that is post-transcriptionally spliced to Cα to generate the TCRα mRNA (Figure 1.7).

For the β chain the variable domain is encoded in three gene segments, Vβ, Dβ, and Jβ. Here either the Dβ1 gene segment rearranges to one Jβ1 segments or the Dβ2 gene segment to one Jβ2 segments. That generates a functional VDJβ-region exon that is post-transcriptionally spliced to Cβ to result in the TCRβ mRNA (Figure 1.7).

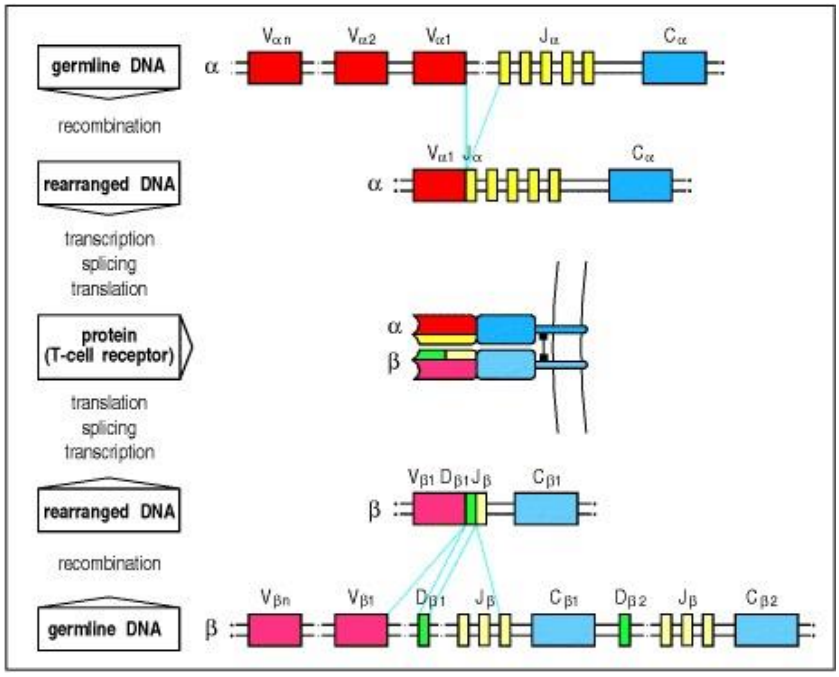

Figure 1.7: TCR Rearrangement. During thymic T cell maturation, the TCR loci undergo rearrangements to generate a highly diverse T cell pool. Taken from (Janeway et al., 2001).

In the human genome, the germline TCRα locus has one constant, 61 J and 54 V segments, the TCRβ locus has two C, two D, 14 J and 67 V gene segments, allowing a total of over 12 million possible combinations. Further variability is introduced by junctional flexibility and nucleotide insertion in the recombined TCRα and β VDJ sequences (Kindt et al., 2007). This results in excess of a trillion potential TCRαβ combinations capable of reacting to non-self (and self) peptides (Toor et al., 2016). Thymic selection pressure results in elimination of nascent T cells that (I) fail to recognize the self MHC-molecule (positive selection, see below) or, (II) that are reacting to self peptides (negative selection).

1.4.3 *Self-MHC Restriction of T Cells*

T cell function critically depends on the interaction of the TCR with MHC molecules. In a population, MHC-molecules are highly polymorphic, in humans the MHC (here also known as HLA) region is known to be the most polymorphic region of the genome (Williams, 2001). Likewise, several mouse strains are characterized by

distinct haplotypes of their H-2 region (expressing the α-chain of MHC-I) thus facilitating immunological studies. In 1974, following experiments on T cell-mediated cytotoxicity in murine lymphocytic choriomeningitis virus (LCMV) it has been observed that T cell mediated lysis of infected target cells requires presentation of antigen on haplo-identical MHC-molecules (Zinkernagel and Doherty, 1974). In addition, it has been observed that haplo-identical helper T cells were required for IgM to IgG-class switch by B cells demonstrating "self-MHC restriction of T cells" a general feature of adaptive immunity (Katz et al., 1973). The self-restriction of T cells is generated during T cell maturation, where nascent T cells are eliminated if they fail to bind to the self MHC molecule by the thymic epithelium in the process termed "positive selection".

1.4.4 *Antigen Presentation by MHC-I*

MHC-I molecules on the cell surface display 8- to 10-residue peptides usually derived from endogenous proteins, except in Dendritic cells as described in section 1.4.6. MHC-I consists of two molecules, the α-chain and β2-microglobulin, which are separately encoded and pair together during the maturation process in the ER of the cell (Kindt et al., 2007). These antigenic peptides are believed to be generated as side products of the continuous turnover of proteins in order to provide a constant "sampling" of the intracellular pool of proteins. MHC-I heterodimers are unstable and readily dissociate at physiological temperature, unless binding to an antigen that stabilizes the protein complex before being transported to cell surface (York and Rock, 1996).

Binding of an antigen to MHC-I depends on the formation of hydrogen bonds between conserved so-called anchor residues of the antigenic peptide with binding pockets, deep clefts on the surface of MHC-I molecules (Parham, 1992). One anchor

residue is located at the C-terminal end of the antigen (position 9) usually occupied by hydrophobic amino acids such as leucine or isoleucine. Another hydrogen bond is being formed between the N-terminal end (positions 2 and 3) and MHC-I. Analyses of peptides eluted from MHC-I molecules have shown that each MHC variant (haplotype) favors distinct anchor residues, thereby allowing predictions about the efficiency a peptide will bind to a certain MHC-I variant (Engelhard, 1994; Parham et al., 1988). Each class of MHC-I (A, B, C in human, B, K, L in mice) and their variants (e.g. H-2K^{b} or H2-K^{d}) preferentially bind to different peptides, a feature that likely contributes to the susceptibility of individuals to immune-linked diseases, e.g. autoimmune reactions (Singh, 2016).

Several cellular mechanisms exist to degrade protein, including the endosomal/lysosomal compartment and the cytoplasmic proteasome complex. Early work has identified the proteasome to be the primary source of antigenic peptides bound to MHC-I (York and Rock, 1996). This evidence originates from the observation that inhibitors of lysosomal proteases did not interfere with MHC-I presentation of the antigens studied while proteasome-inhibitors did, and artificial introduction of proteins into the cytosol facilitated their presentation on MHC-I. Moreover, the TAP system mediating the transport of cytosolic peptides (antigens) into the ER has been found to be crucial for MHC-I antigen presentation (York and Rock, 1996).

However, some exceptions for the proteasomal origin of MHC-I antigens have been found (Cruz et al., 2017; Rock et al., 2010). Octapeptides injected into the cytosol or expressed by minigenes do not require cleavage by proteases in order to stimulate T cells (Craiu et al., 1997). In addition, MHC-I molecules have been observed to undergo a recycling process by the endosomal-lysosomal pathway, where

their antigen is replaced and subsequently, after returning to the cell surface, these MHC molecules present “lysosomal” antigens processed likely by cathepsins (Yewdell et al., 2003). Furthermore, it has been shown that the lysosomal proteases cathepsin S and L are involved in antigen-presentation by MHC-II molecules in antigen-presenting cells, thymic cortical epithelial cells and, most notably, IEC (Beers et al., 2005; Honey et al., 2002; Nakagawa et al., 1998; Sevenich et al., 2010).

1.4.5 *Tumor Neoantigens*

T cells that react to self-antigens are eliminated in the process of negative selection (central tolerance). Therefore, detection of tumors by T cells requires one of two different classes of antigens. The first class consists of antigens the induction of central tolerance against fails, like proteins with restricted tissue expression pattern including proteins only present during embryonic development or exclusively expressed behind physiological barriers such as the blood-brain-barrier.

A second class of antigens capable of activating T cells consists of peptides that are entirely absent from the genome of that organism, so-called neoantigens. In tumors without a viral etiology neoantigens are considered to be created by tumor cell-specific DNA alterations that result in the formation of novel protein sequences (Schumacher and Schreiber, 2015). These neoantigens are of particular interest for novel therapeutic strategies as their effect is not affected by T cell tolerance. One major culprit, however, is the high inter-individual variability of neoantigens between patients (Alexandrov et al., 2013) as well as shifts in the neoantigen-formation within the same tumor over time (Verdegaal et al., 2016) or as a response to therapy (Anagnostou et al., 2017).

Furthermore, predictions of neoantigens based on genomic analysis of tumor cells tend to yield hits that fail to induce anti-tumor immune reactions. This discrepancy

can be explained by the observation that not all antigens are cross-presented by DC (see section 1.4.6) equally well. Another reason can be immunodominance, where one particular antigen induces a strong immune reaction while other antigens within the same tissue are being ignored. Though predictions on T cell reactivity towards a certain antigen can be made *in silico*, individuals differ substantially in their actual T cell reaction (Schumacher and Schreiber, 2015).

1.4.6 *Antigen Presentation by Dendritic Cells*

Dendritic cells (DC) are central regulators of the adaptive immune system in mammals and are present in high numbers in lymphoid organs, the blood and mucosal surfaces. They constantly scan their environment for the presence of danger signals by toll-like-receptors, purinergic receptors, immunoglobulin receptors (FcR), cytokine receptors and receptor-mediated endocytosis (Guermonprez et al., 2002). DC are members of the group of professional antigen presenting cells together with B cells and macrophages that are capable of interacting with $CD4^+$ T cells through expression of MHC-II molecules.

Activation of DC consists of (I) expression of MHC-peptide complexes on the cell membrane, (II) upregulation of the costimulatory molecules CD80/CD86, and (III) expression of cytokines that drive T cell proliferation and differentiation, e.g. IL-12, IL-1β, IL-6 and TNF; (Mellman and Steinman, 2001) and T cells depend on these signals for activation (see section 1.4.1). In DC, three distinct pathways for MHC-I presentation of antigens have been identified so far (Figure 1.8):

a) Direct presentation: As in any other cell, MHC-I molecules can bind to peptides derived from endogenously expressed proteins, including viral proteins in case of an infection.

b) Cross presentation: During this process antigens taken up from the external environment of the cell are being displayed on MHC-I on their surface. Both phagocytosis and pinocytosis can supply antigens for this process, the former commonly yields a stronger T cell activation than the latter. In the phagosome-to-cytosol-pathway, phagocytosed protein is being transferred from the endosomal compartment to the cytosol of the DC, where it is cleaved by the proteasome and then transferred into the ER by TAP in a similar fashion as described above.

Alternatively, a TAP- and proteasome-independent vacuolar pathway has been described (Cruz et al., 2017). In this pathway protein is cleaved within the endosomal compartment and loaded onto MHC-I molecules inside these vesicles. The lysosomal protease cathepsin S plays a critical role in this pathway (Shen et al., 2004).

c) Cross dressing: In addition to these pathways DC have been found to acquire preformed peptide-binding MHC-I complexes from neighboring cells, present them on their surface and activate $CD8^+$ T cells without any further peptide processing (Nakayama, 2014; Yewdell and Haeryfar, 2005). This has been implicated in anti-tumor immunity as well as anti-viral host defense (Dolan et al., 2006; Wakim and Bevan, 2011). The transfer is facilitated by trogocytosis (intercellular exchange of plasma membrane fragments between cells) in some studies, while in others exosomes are involved (Nakayama, 2014). Furthermore, in one study using a vaccination model, cross-dressed $CD8\alpha^+$ $CD103^+$ DC were found to efficiently activate naïve and memory T cells and cross-dressing induced an immune response to a similar extent as did cross-presentation (Li et al., 2012).

Given the fact that naïve T cells are frequently found only in lymphoid organs and (conventional) DC have the capacity to migrate between mucosal and lymphoid

tissue, both cross presentation and cross dressing probably evolved as a central mechanism in adaptive immunity.

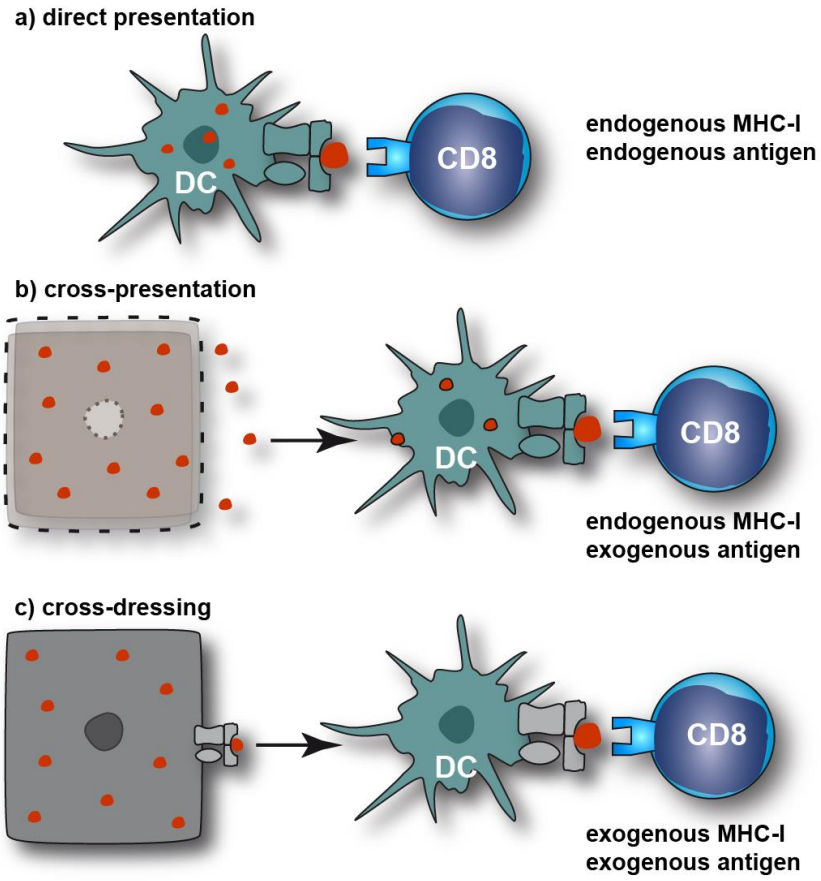

Figure 1.8: Antigen Presentation by MHC-I in DC. (a) In direct presentation DC present endogenous antigen on endogenous MHC molecules, whereas **(b)** in cross-presentation exogenous antigen is used. **(c)** Cross-dressing describes the uptake of exogenously assembled MHC-I-antigen-complexes and their presentation by DC.

1.4.7 *Function of DC within Tumors*

DC possess unique abilities to activate and orchestrate effective reactions by the adaptive as well as the innate immune system. However, in tumors DC have been found to be rather of immature, immunosuppressive biology. They tend to show low co-stimulatory molecule expression, blunted antigen cross-presentation and expression of regulatory molecules and receptors, like PDL-1, a molecules expressed

by tumor and various stromal cells inducing T cell anergy, or TIM-3, a factor known to suppress T_h1-cell function (Tran Janco et al., 2015).

A number of molecules found in the tumor microenvironment inhibit DC activation *in vitro*, including VEGF, prostaglandin E2, and IL-10 (Zong et al., 2016). Other factors likely suppressing DC function relate to the metabolic dysfunction within tumors as hypoxia and lactic acid suppress DC activation *in vitro*. During TLR-mediated activation DC undergo metabolic reprograming and this could be affected within tumors as well (Gardner and Ruffell, 2016).

1.4.8 *Immunosuppressive Mechanisms of Tumors*

Traditionally, tumor cells have been divided into highly, intermediate or poorly immunogenic based on the ability of recipient mice to reject those when transplanted. However, it has been discovered that a highly immunogenic tumor can progress in an immunocompetent mouse when autochthonously emerging rather than being transplanted to, even though tumor-specific $CD8^+$ T cells exist in the host (Willimsky and Blankenstein, 2005). One major cause of this phenomenon might be the fact that tumors emerge rather slow and therefore tumor-derived antigens can be present over long periods of time. Indeed, according to a study the fate of anti-tumor immunity is being determined already at the state of precursor lesions (Willimsky et al., 2008).

First recognized in viral host defense, chronic TCR stimulation results in dysfunctional T cells characterized by (I) the expression of inhibitory receptors on the surface like PD-1, CTLA-4, TIM-3, (II) downregulation of effector functions, e.g. loss of IL-2-, TNF-α- and IFN-γ-production, and (III) an altered gene expression pattern in pathways involved in chemotaxis, migration, and metabolism (Thommen and Schumacher, 2018).

In addition, the tumor microenvironment itself consists of several inhibitory features on T cell function, including

1. the expression of inhibitory receptors and their ligands, like PD-L1;
2. presence of immunosuppressive cell populations like regulatory T cells (T_{reg}) and myeloid-derived suppressor cells;
3. the expression of suppressive cytokines like IL-10 and TGF-β;
4. the release of metabolites and compounds, such as adenosine, prostaglandins, lactate and reactive oxygen species known to suppress T cell function; and
5. physiological changes such as hypoxia, low pH, and the deprivation of nutrients, like glucose or amino acids required for proper T cell function.

Recently, several therapeutic agents e.g. blocking antibodies against PD-1, PD-L1 or CTLA-4 have been developed for immunotherapy of cancer with promising results in some patients suffering from cancer entities like melanoma or lung carcinoma, while some patients do not respond to the agents available so far (Sukari et al., 2016).

1.5 Degradation of Mitochondria by Autophagy

Besides the aforementioned proteasome, cells consist of a second mechanism of protein degradation termed autophagy. This pathway is involved in a broad range of diseases, including cancer. Much attention has recently been paid on its highly diverse role as a response mechanism to cellular stress (e.g. during nutrient starvation) as well as a specific mechanism to degrade aged or damaged organelles, especially mitochondria.

During Autophagy (precisely: macroautophagy) proteins or organelles are being enclosed within vesicles termed autophagosomes, that subsequently fuse with lysosomes, protease-rich organelles where degradation of cargo takes place (Levine and Kroemer, 2008). Key elements of this process are proteins from the Atg-family and the proteins LC3 and p62. The Atg-family comprises of evolutionally conserved proteins that are responsible for autophagosome-formation in various steps (Figure 1.9).

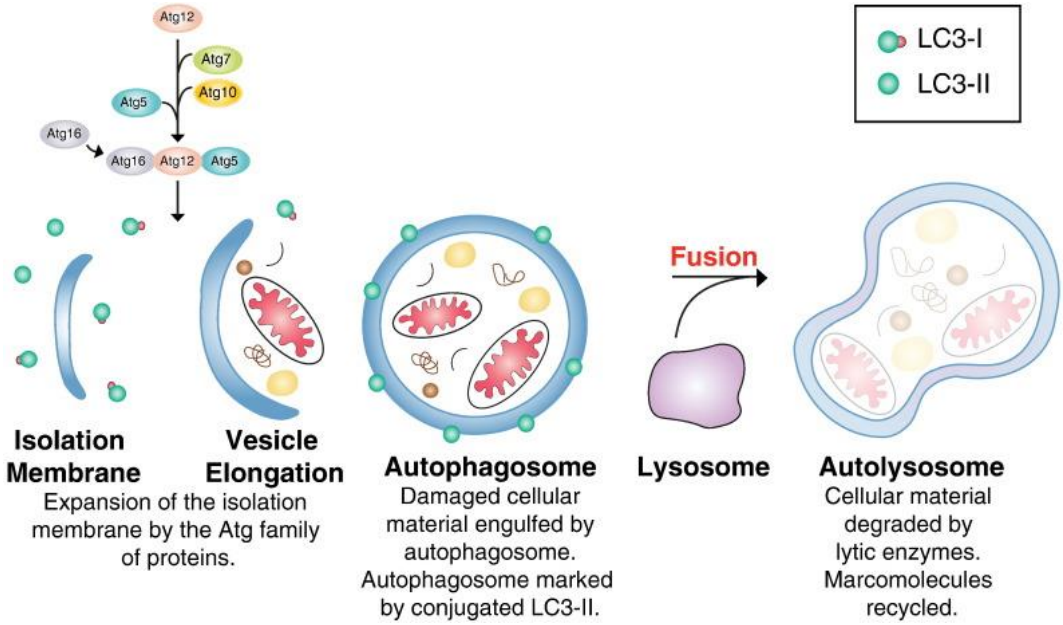

Figure 1.9: The Autophagic Pathway. The isolation membrane is formed in the cytosol and expanded by the conjugation of Atg proteins. Proteins subjected to turnover and damaged organelles are engulfed by the newly formed autophagosome, marked by LC3-II on the surface. The autophagosome fuses with lysosomes and its cargo is degraded by lysosomal hydrolyses. Taken from (Kotiadis et al., 2014).

1.5.1 *Molecular Mechanism of Autophagy*

Autophagosomes arise from pre-autophagosomal structures on the ER, where complex protein-lipid interactions create an Ω-like shape termed omegasome. This structure consists of an initiation membrane (IM) that is subsequently elongated and finally forms a closed structure separated from the ER, the autophagosome.

One critical protein in this step is microtubule-associated protein light chain 3 (LC3), an ubiquitin-like protein that is activated by the E1-ligase ATG7 (E1 enzyme), transferred to ATG3 (E2 enzyme) and finally covalently linked ("lipidated") to phosphatidylethanolamine, a major membrane phospholipid. Lipidated LC3 can be found on both the inner and outer membrane of autophagosomes and interacts with the receptor p62 (among others) for selective cargo incorporation into the autophagosome (Mizushima et al., 2011).

1.5.2 *Mitophagy: Selective Degradation of Mitochondria by Autophagy*

Mitochondria are organelles specialized in metabolism involving oxygen. Their dysfunction can endanger the integrity of the cell, especially by generation of reactive oxygen species or by uncontrolled caspase activation. Therefore, a selective degradation mechanism for aged or damaged mitochondria has evolved, the PINK1/Parkin-system.

PINK1 is a mitochondrial serine/threonine kinase that is degraded to undetectable levels in cells with healthy mitochondria. However, in mitochondria with reduced membrane potential, the driving force of mitochondrial respiration, PINK1 becomes stabilized on the outer mitochondrial membrane. PINK1 then promotes Parkin-mediated mitophagy by recruiting Parkin to mitochondria and promoting Parkin's E3 ligase activity, enabling the ubiquitylation of mitochondrial proteins (Ni et al., 2015). Ubiquitylated mitochondrial components are then engulfed in autophagosomes, putatively mediated by p62 as receptor (Youle and Narendra, 2011). In addition to Parkin-dependent mitophagy mitochondria can also be degraded by alternative means, e.g. by NIX-dependent autophagy during erythrocyte maturation.

Furthermore, mitochondria are highly dynamic organelles that have been found to constantly undergo fusion and fission as means to adapt to changing metabolic

requirements. Upon increasing metabolic needs mitochondria are known to undergo membrane fusion of the inner and the outer mitochondrial membrane (Mishra and Chan, 2016). Mitochondrial fission describes the breakup of mitochondrial pieces into smaller units suitable for mitophagy. In mammalian cells this process is mediated by the protein dynamin-related protein 1 (DRP1) as phosphorylated DRP1 can be recruited to the outer mitochondrial membrane and induces the constriction of the mitochondrion and its separation into two separate units (Ni et al., 2015).

1.6 Lysosomal Function in Cell Death

Lysosomes are membrane-enclosed organelles that can make up to 5% of intracellular volume. They contain a broad range of hydrolytic enzymes such as proteases, lipases, nucleases, glycosidases, phospholipases, phosphatases and sulfatases that contribute to the intracellular turnover of macromolecules (Boya and Kroemer, 2008; Luzio et al., 2007). A vacuolar ATPase within the lysosomal membrane maintains a proton gradient towards the cytoplasm with an intralysosomal pH of 4.6 to 5. Macromolecules for degradation are delivered to lysosomes by fusion of endosomes or autophagosomes by vesicular fusion (Luzio et al., 2007).

The high content of hydrolytic enzymes in lysosomes and its high proton concentration makes them potentially harmful to the cell and upon discovery, lysosomes have been termed “suicide bags” (de Duve, 1959; Turk and Turk, 2009). In particular, lysosomes have been found to be sensitive to oxidative stress, causing membrane destabilization resulting in apoptosis or necrosis (Antunes et al., 2001; Lin et al., 2010; Wei et al., 2008). In particular, the so-called Fenton type of reactions has been found to be critical for lysosomal membrane stability: As expressed in equation I, reaction of hydrogen peroxide (an uncharged molecule freely diffusible across

biological membranes) with bivalent (ferrous) iron forms highly reactive hydroxyl radicals (Terman et al., 2006).

$$H_2O_2 + Fe^{2+} \rightarrow OH^{\bullet} + OH^{-} + Fe^{3+} \quad \text{(I)}$$

In this context it is noteworthy that the lysosomal membrane contains the highest amount of the antioxidant vitamin E of biological membranes at concentrations over 30 times higher than microsomal membranes (Rupar et al., 1992). At the low pH within lysosomes the trivalent (ferric) iron produced can be reduced to bivalent iron by reducing agents such as the thiol group of cysteine, thus facilitating a chain reaction fueled by intralysosomal iron.

1.6.1 *Intralysosomal Iron*

Iron is a key element for mammalian life being the most abundant trace element in an organism with about 3.5 - 4.0 g in human adults (Linder, 2013). The list of iron-containing proteins can be divided grossly into two groups: (I) the heme protein family containing hemoglobin, myoglobin, and enzymes such as cytochromes, catalases, heme-peroxidase; and the group of (II) non-heme iron enzymes, containing e.g. ribonucleotide reductase, aconitase, isocitrate dehydrogenase, succinate dehydrogenase, NADH dehydrogenase (Geissler and Singh, 2011).

Apart from erythrocytes or muscle cells, cells predominantly use iron for synthesis of heme and iron-sulfur clusters in mitochondria, and most iron-containing enzymes of cells are indeed located within mitochondria, most notably the respiratory chain and TCA cycle enzymes (Wang and Pantopoulos, 2011). As mitochondria undergo autophagic degradation they are being transported into the lysosomal compartment, a major pathway for intralysosomal iron accumulation. Another source of intralysosomal iron is ferritin autophagy. Ferritin is a large protein complex consisting of 24 heavy- and light subunits used by cells to store and detoxify excess

intracellular iron within the cytosol. Lysosomal degradation following ferritin-autophagy is crucial for release of the iron stored (Asano et al., 2011; Zhang et al., 2010). In addition, iron can enter the lysosomal compartment via the endosomal uptake of extracellular iron bound to transferrin (Kurz et al., 2008).

1.6.2 *Lysosomotropic Agents*

As lysosomes are enclosed by a lipophilic membrane, unpolar substances can diffuse easily in and out the organelle, whereas for polar substances diffusion is restricted. The term “lysosomotropic substances” describes weakly basic amines that freely diffuse across membranes in their uncharged form but become trapped in their protonated (non-diffusible) form inside the acidic lysosome (de Duve et al., 1974). When these protonated bases accumulate at concentrations above a certain threshold they usually acquire detergent-like properties that can induce a potentially lethal destabilization of the lysosomal membrane (Boya and Kroemer, 2008).

1.6.3 *Lysosomal Membrane Permeabilization*

The term lysosomal membrane permeabilization (LMP) is used to describe the release of lysosomal proteases and protons into the cytosol through a damaged lysosomal membrane. Among others, the aforementioned Fenton reactions or accumulation of lysosomotropic agents can induce LMP (Boya and Kroemer, 2008). Released proteases can activate apoptotic effectors such as mitochondrial proteins and caspases.

1.7 Previous Work on the Immunogenicity of Stat3-Deficient Sporadic Tumors

The findings of reduced tumorigenesis associated with inflammation in Stat3-deficient mice (see above) prompted the evaluation of Stat3 in sporadic

carcinogenesis. Research conducted by Dr. rer.nat. Julia Bollrath in the laboratory of Univ.-Prof. Dr. med. Florian R. Greten has shown an important contribution of Stat3 in a model of intestinal hyperproliferation that closely resembles the early phase of human colon carcinogenesis in the classical, Wnt-dependent pathway (see section 1.1). Mice with a constitutive activation of Wnt-signaling in IEC due to a conditional, Cre-mediated truncation of the gene encoding β-Catenin (termed *β-cat*$^{c.a.}$) showed a prolonged survival when in addition Stat3 was deleted on the genetic level in IEC, termed *β-cat*$^{c.a.}$/*Stat3*$^{\Delta IEC}$ mice (Figure 1.10).

.

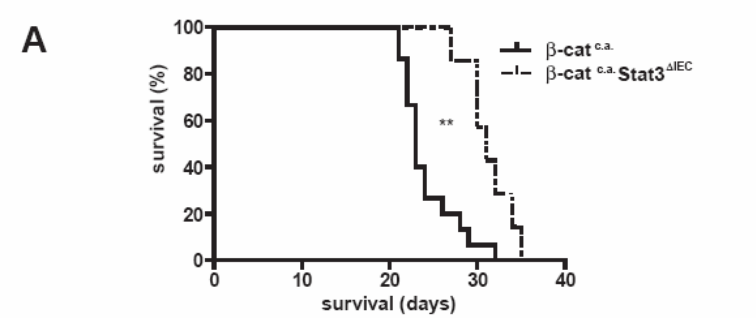

Figure 1.10: Lack of Stat3 in intestinal epithelial cells leads to prolongation of survival after conditional activation of β-Catenin by tamoxifen administration. Kaplan Meier-survival curves of *β-cat*$^{c.a.}$ (n=15) and *β-cat*$^{c.a.}$/*Stat3*$^{\Delta IEC}$ (n=7). **p<0,01 by log rank test. Figure taken from (Bollrath, 2010), original fig. 4.11A.

Intriguingly, proliferation of epithelial cells was indifferent between the groups of Stat3-proficient and -deficient *β-cat*$^{c.a.}$ mice and key regulators of cell cycle progression were unchanged (Figure 1.11), in stark contrast to the findings in colitis-associated carcinogenesis (Bollrath et al., 2009).

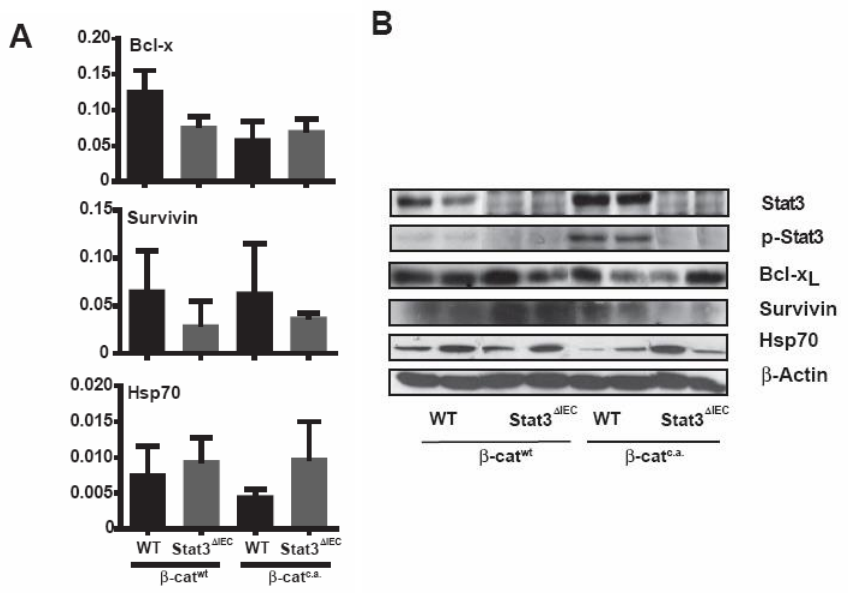

Figure 1.11: Molecular analysis of Stat3 target genes involved in regulation of apoptosis. (A) Relative expression levels of mRNA of apoptosis-related Stat3 target genes analyzed by real-time PCR. Data are mean ± SEM, n≥4. (B) Immunoblot analysis for the indicated proteins in lysates prepared from isolated small intestinal enterocytes from wildtype, *Stat3*$^{\Delta IEC}$, *β-cat*$^{c.a.}$ and *β-cat*$^{c.a.}$/*Stat3*$^{\Delta IEC}$ on day 15 after administration of tamoxifen. Figure taken from (Bollrath, 2010), original fig. 4.13A, B.

However, the intestines of *β-cat*$^{c.a.}$/*Stat3*$^{\Delta IEC}$ mice showed a marked infiltration of T cells and elevated IFNγ-production (Figure 1.12). This suggested the contribution of T cells to the observed deceleration of tumorigenesis. In a series of experiments it could be demonstrated that the survival advantage is completely abolished in case of disturbed adaptive immunity (Figure 1.13). Depletion of $CD8^+$ T cells by antibody injections, depletion of DC by employment of CD11c-DTR allele or genetic deletion of IFNγ in *β-cat*$^{c.a.}$ mice were all equally effective to block the survival advantage of *β-cat*$^{c.a.}$ /*Stat3*$^{\Delta IEC}$.

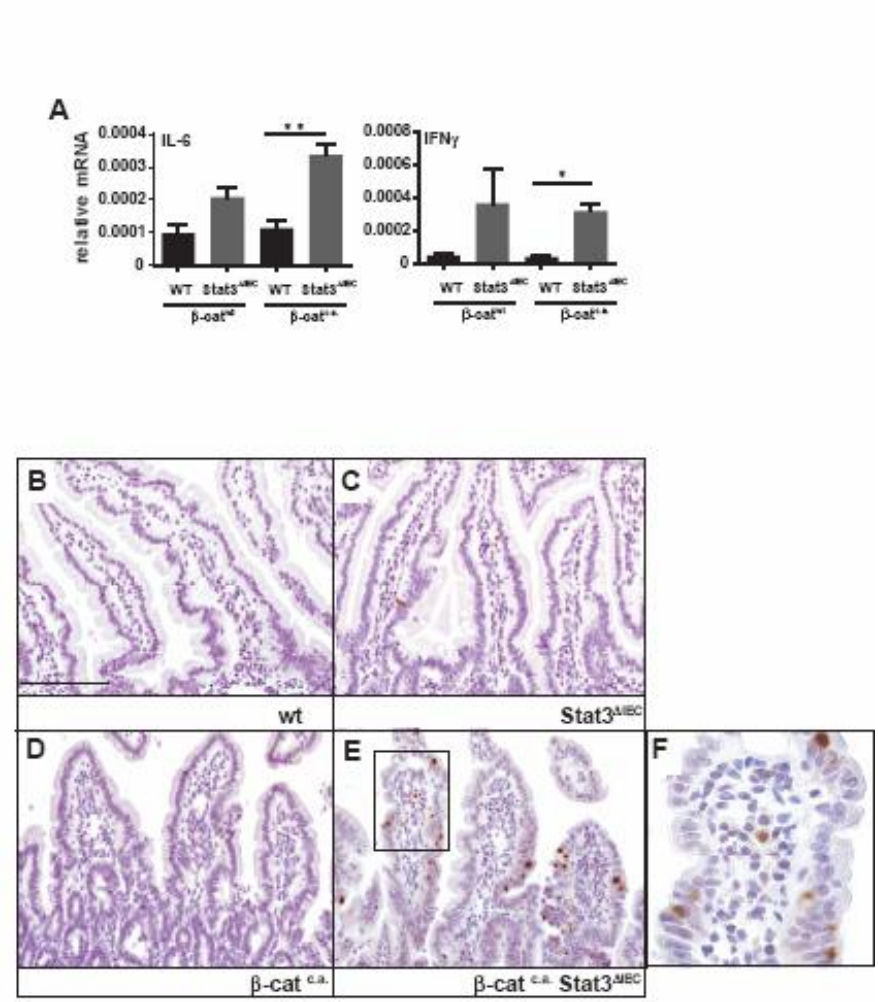

Figure 1.12: Intestinal Epithelial Deletion of Stat3 Leads to IFNγ Secretion in the Lamina Propria on Day 15 After β-Catenin Activation by Tamoxifen Administration. (A) Relative expression levels of mRNA encoding for IL-6 and IFNγ in the lamina propria in animals of the indicated genotype on day 15 of the model analyzed by real-time PCR. Data are mean ± SEM, n ≥4. *p<0,05, **p<0,01 by t-test. **(B-F)** Immunohistochemical analysis of IFNγ in sections of wildtype, *Stat3*$^{\Delta IEC}$, *β-cat*$^{c.a.}$ and *β-cat*$^{c.a.}$/*Stat3*$^{\Delta IEC}$ animals. (F) Magnified view of inset in (E). Scale bar= 100 μm. Figure taken from (Bollrath, 2010), original fig. 4.15A-F.

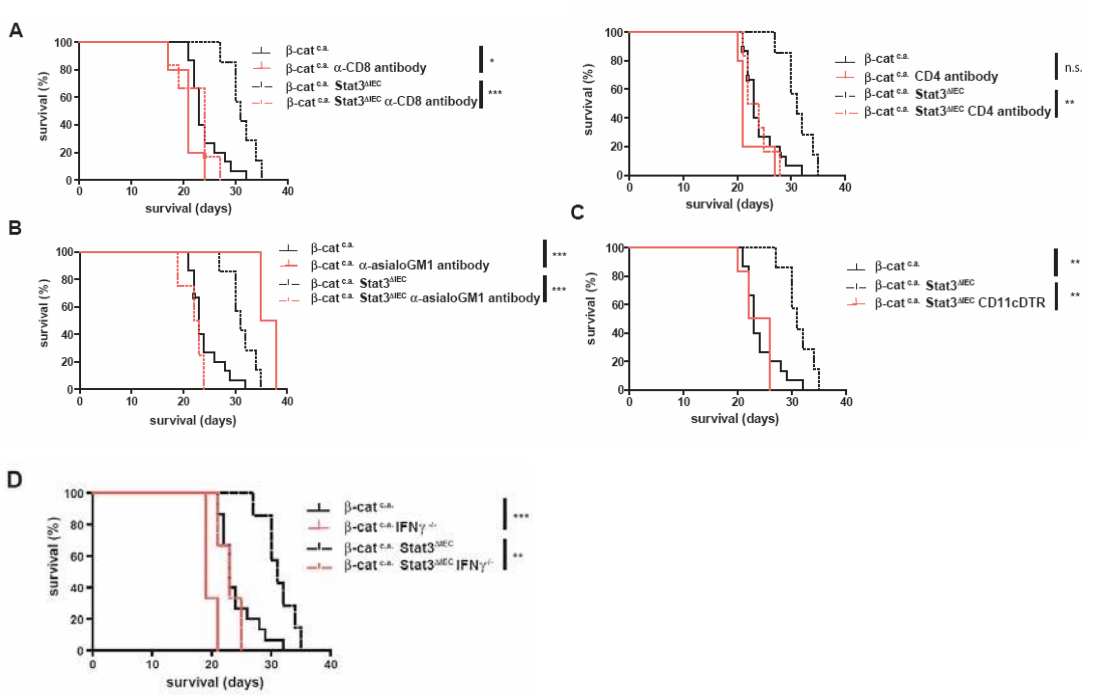

Figure 1.13: Survival Advantage in *β-cat*$^{c.a.}$/*Stat3*$^{\Delta IEC}$ Animals Relies on CD4$^+$ and CD8$^+$ T Cells, NK- Cells as Well as CD11c$^+$ Cells. (A) Kaplan-Meier survival curve of *β-cat*$^{c.a.}$ and *β-cat*$^{c.a.}$/*Stat3*$^{\Delta IEC}$ animals untreated (black lines) and treated with α-CD8/α-CD4 (n≥5) (red lines) antibody. **(B)** Kaplan-Meier survival curve of *β-cat*$^{c.a.}$ and *β-cat*$^{c.a.}$/*Stat3*$^{\Delta IEC}$ animals untreated (black lines) and treated with α- asialoGM1 (red lines) (n≥ 4) antibody to deplete natural killer cells. **(C)** Kaplan-Meier survival curve of *β-cat*$^{c.a.}$ and *β-cat*$^{c.a.}$/*Stat3*$^{\Delta IEC}$ animals untreated (black lines) and *β-cat*$^{c.a.}$/*Stat3*$^{\Delta IEC}$ transplanted with bone marrow of *CD11cDTR* animals (n= 6) and treated diphtheria toxin (DT) (red line) to deplete CD11c$^+$ cells. **(D)** Kaplan-Meier survival curve of *β-cat*$^{c.a.}$ (n≥7), *β-cat*$^{c.a.}$/*Stat3*$^{\Delta IEC}$ (n≥7), *β-cat*$^{c.a.}$/*IFNγ*$^{-/-}$ (n≥3) and *β-cat*$^{c.a.}$/*Stat3*$^{\Delta IEC}$/*IFNγ*$^{-/-}$ (n≥3) mice. *p<0,05, **p<0,01, ***p<0,001 by log-rank test. Figure taken from (Bollrath, 2010), original fig. 4.16.

2 Aim of the Study

As outlined above, Stat3 has emerged as a major regulator of tumorigenesis. It is considered as a key mediator of pro-tumorigenic factors of the tumor microenvironment and has been shown to be a central mediator in a feed-forward mechanism involving several immune-related cytokines and transcription factors. However, the role of Stat3 in sporadic carcinogenesis, that is tumors emerging on previously non-inflamed tissue as seems to be common in humans, has not been studied thoroughly.

Preliminary data showed that in addition to transcriptional regulation of pro-survival and pro-proliferation genes, Stat3 might be engaged in regulating adaptive anti-tumor immunity in early stage tumor cells. The work presented here intended to

(I) characterize the anti-tumor immune response observed in this model,

(II) identify the molecular mechanism of Stat3-regulated anti-tumor immunity, and

(III) evaluate potential therapeutic implications for future anti-cancer therapy strategies.

3 Material and Methods

3.1 Animal Models

Mice used in this study were as following:

mouse line:	allele	origin, identifier	description/genetic modification
*villin-cre*ER^{T2}	Tg(Vil-cre/ERT2)^{23Syr}	(el Marjou et al., 2004); MGI:3053826	Tamoxifen-inducible Cre-expression in IEC.
Stat3$^{F/F}$	Stat3^{tm1Aki}	(Takeda et al., 1998); RRID:IMSR_APB:2010	"Floxed" exon 21 of Stat3; deleting both Y705 and S727 residues when recombined by Cre.
Ctnnb$^{loxEx3/wt}$	Ctnnb1^{tm1Mmt}	(Harada et al., 1999); MGI:1858008	"Floxed" exon 3 of the gene encoding β-Catenin, including its degron-domain.
Ctss$^{-/-}$	Ctss^{tm1Hap}	(Shi et al., 1999); RRID:MGI:3573791	Whole-body deletion of cathepsin S.
Ctsl$^{F/F}$	Ctsl$^{tm1.1Thre}$	(Tholen et al., 2014); RRID:MGI:5810299	Conditional knock-out of cathepsin L.
Atg7$^{F/F}$	Atg7$^{tm1.1Tchi}$	(Komatsu et al., 2005); RRID:MGI:3590136	„Floxed" exon 14 of Atg7 containing the active site cysteine residue essential for substrate activation.
ROSAOVA	Gt(ROSA)26Sor$^{tm2(OVA/EGFP)Dwir}$	(Sandhu et al., 2011); MGI:5056498	Cre-mediated expression of ovalbumin-derived MHC-I and -II restricted antigens.
OT-I	Tg(TcraTcrb)1100Mjb	Jackson Laboratories #003831; RRID:MGI:5292730	Mice harbor CD8^{+} T cells with a transgenic TCR recognizing OVA$_{aa257-264}$ (SIINFEKL).
Tap1$^{-/-}$	Tap1^{tm1Arp}	Jackson Laboratories# 002944; RRID:MGI:3621930	Whole-body knock-out of *Tap1*, deficient in MHC-I antigen presentation.

3.1.1 *Villin-cre*^{ERT2}

Upon tamoxifen administration, cells with an active *Villin1*-promoter (mainly epithelial cells throughout the intestine) express *Cre* ("Causes recombination") and recombination of loxP ("locus of X-over P1")-sites occurs. LoxP-sites are 34 bp elements naturally occurring in the genome of bacteria. For site-specific recombination within the genome of a mouse, loxP-sites are inserted into genes or other parts of the DNA and Cre activity can either cause deletions, inversions or translocations, depending on the orientation of loxP sites.

In order to generate a "conditional knock-out" mouse, the gene of interest is flanked by loxP-sites (termed "floxed"). This gene is expressed at a close-to-normal

level, unless *Cre* is activated. In this mouse line, *Cre*-expression stops rapidly after withdrawal of tamoxifen, yet recombined alleles persist in the gut due to activity of *Villin1* in the stem cell compartment (el Marjou et al., 2004).

3.1.2 *Stat3*$^{\Delta IEC}$

In *Stat3*$^{F/F}$ mice loxP-sites have been inserted into both introns neighboring exon 21 of Stat3 containing the phosphorylation site tyrosine 705. Due to the usage of a cryptic splice site, a part of exon 22 containing the serine 727 phosphorylation site is also removed by Cre-mediated recombination (Schweizer et al., 2002; Takeda et al., 1998), resulting in conditional knock-out of 31 amino acid residues out of 770 of wildtype *Stat3* containing both activation domains known.

Stat3$^{F/F}$ mice have been crossed with *villin-cre*ER^{T2} mice and respective offspring has been treated with tamoxifen to generate *Stat3*$^{\Delta IEC}$ mice.

3.1.3 *β-cat*$^{c.a.}$

The mouse line *Ctnnb*$^{loxEx3/wt}$ harbors loxP-sites at both introns neighboring exon 3 of *Ctnnb1*, the exon containing the degron domain of β-Catenin. After Cre-mediated recombination respective cells express a truncated form of β-Catenin that can no longer be phosphorylated as required for proteasomal degradation. Mutant β-Catenin accumulates within the cytoplasm and nucleus, where it can activate the transcription of target genes, thereby mimicking active Wnt signaling.

Crossing with *villin-cre*ER^{T2} mice and induction of Cre-expression in respective offspring by tamoxifen-treatment generates *β-cat*$^{c.a.}$ mice, characterized by intestinal

polyposis closely resembling early stage tumorigensis (Harada et al., 1999; Schwitalla et al., 2013a).

3.1.4 *Ctss*$^{-/-}$

Whole body deletion of cathepsin S was achieved by homologous recombination targeting exon 5, which contains the active site cysteine of murine cathepsin S (Shi et al., 1999). This null mutant of cathepsin S shows a defective MHC-II pathway and angiogenesis (Shi et al., 2003).

3.1.5 *Ctsl*$^{F/F}$

Two loxP sites have been introduced into the introns 3-4 and 7-8 of *Ctsl*. Cre-mediated recombination results in deletion in exons 4 to 7 with a frameshift thereafter.

3.1.6 *Atg7*$^{F/F}$

Conditional knock-out of *Atg7* is achieved by Cre-mediated recombination of two loxP-sites introduced into the introns flanking exon 14. This exon contains containing the active site cysteine residue essential for activation of LC3, a major step in the generations of autophagosomes.

3.1.7 *ROSAOVA*

This mouse line has been inserted a part of the chicken ovalbumin gene encoding aa 246–353 (with an indel at position 258 changing isoleucine to valine) in antisense orientation into the ubiquitously active ROSA26 locus. This sequence is flanked by inversely oriented loxP sites, resulting in continuous inversion of the

cassette by Cre-mediated recombination with expectedly 50% of Cre-expressing cells in “on” and 50% in “off” state (Sandhu et al., 2011).

The inserted fragment encodes the amino acid residues $OVA_{aa257-264}$ (SIINFEKL), a frequently used model antigen presented by K^b (MHC-I) and recognized by the TCR expressed in the OT-I mouse line. Furthermore, the $OVA_{aa323-339}$ (ISQAVHAAHAEINEAGR) antigen is expressed as well, which can be presented by MHC-II and recognized by OT-II and DO11.10 TCR. In addition, the cassette expresses eGFP and the SV40 T-antigen.

When bred with *villin-cre*ER^{T2} mice, the resulting mouse line has been termed *OVA*^{Vil} to indicate the expression of *OVA*-fragments in cells with active *Villin*-promoter. This mouse line was intercrossed with *villin-cre*ER^{T2}/*Ctnnb*$^{loxEx3/wt}$ and *villin-cre*ER^{T2}/*Ctnnb*$^{loxEx3/wt}$ *Stat3*$^{F/F}$ mice to obtain the respective compound mutant mice as indicated.

3.1.8 *OT-I*

This transgenic mouse line expresses rearranged mouse TCRα (Tcra-V2, Tcra-J(α26)) and TCRβ (Tcrb-V5, Tcrb-D(β2), Tcrb-J(β2.6)) chains. Those have been cloned from the ovalbumin-recognizing T cell lines AD10 (TCRα) and B3 (TCRβ). Due to expression of these constructs in thymocytes (naïve T cells during thymic selection) these mice almost exclusively harbor ovalbumin-recognizing, MHC-I restricted $CD8^+$ T cells (Hogquist et al., 1994).

These mice have been used as donor mice of splenocytes or T cells for *in vitro* studies.

3.1.9 *Tap1*$^{-/-}$

This mouse line was generated by homologous recombination of a 7 kb fragment within the MHC-II locus, deleting about 80% of the coding region of *Tap1* while preserving the expression of Lmp7, which shares a bidirectional promoter with *Tap1* (Ferrington and Gregerson, 2012). Homozygous offspring shows defective MHC-I antigen-presentation and reduced numbers of $CD8^+$ T cells after thymic selection (Van Kaer et al., 1992).

This mouse line has been used as donor of DC for *in vitro* studies.

3.2 Genotyping

Genotyping was performed by PCR. As template, genomic DNA was isolated using a tail probe placed in 100 µl of tail lysis buffer (see below) and shaken for 2-16 hours at 60°C. Thereafter, proteinase K has been inactivated by heating the samples to 95°C for 10 min, then undigested material has been pelleted at 10.000 g for 10 min and supernatants containing gDNA diluted 1:10 with dH_2O. For genotyping of *Ctsl*^{F} mice samples were purified before PCR (NucleoSpin gDNA Clean-up kit, Macherey-Nagel, Düren, Germany).

Tail Lysis Buffer
1.5 M Tris (pH 8,5)
200 mM NaCl
5 mM EDTA
0.2 % SDS
5 %v/v proteinase K (Qiagen, Hilden, Germany)

PCR reaction		
	10X PCR buffer	2 µl
	50 mM MgCl2	0.8 µl
	10 mM dNTP Mix	0.4 µl
	20 mM forward primer	0.5 µl
	20 mM reverse primer	0.5 µl
	Taq polymerase (all Thermo Scientific, Waltham, USA)	0.15 µl
	template (gDNA)	1.5 µl
	dH_2O (up to 20 µl final volume)	14.15 µl
PCR conditions	35 cycles, additional denaturation period at 94°C for 5 min. prior to the start plus final elongation period at 72°C for 10 min. after the last cycle	
primers used:		
***villin-cre*ER^{T2}**	forward primer	5'-ACC TGA AGA TGT TCG CGA TTA TCT-3'
	reverse primer	5'-ACC GTC AGT ACG TGA GAT ATC TT-3'
	cycle details	94°C 30 s, 58°C 30 s, 72°C 30 s
	amplicon size	370 bp
Stat3	forward primer	5'-CCT GAA GAC CAA GTT CAT CTG TGT GAC-3'
	reverse primer	5'-CAC ACA AGC CAT CAA ACT CTG GTC TCC-3'
	cycle details	94°C 30 s, 58°C 30 s, 72°C 30 s
	amplicon size	220 bp (wildtype), 320 bp (floxed allele)
***Ctnnb*^{loxEx3}**	forward primer	5'-CTG AAT GAA CTG CAG GAC GA-3'
	reverse primer	5'-TTC CCA GTC CTT CAC GCA AG-3'
	cycle details	94°C 30 s, 58°C 30 s, 72°C 120 s
	amplicon size	1000 bp
***Ctnnb*^{wt}**	forward primer	5'-TTC CCA GTC CTT CAC GCA AG-3'
	reverse primer	5'-GCA AGT TCC GCG TCA TCC T-3'
	cycle details	94°C 30 s, 58°C 30 s, 72°C 60 s
	amplicon size	400 bp
***Ctss*^{KO}**	forward primer	5'-CTC TGT GTA GCC TGG AAT TC-3'
	reverse primer	5'-CTA AAG CGC ATG CTC CAG ACT GCC-3'
	cycle details	94°C 30 s, 62°C 45' s, 72°C 45 s
	amplicon size	180 bp
***Ctss*^{wt}**	forward primer	5'-GTA GGA AGC GTC TGC CTC TAT-3'
	reverse primer	5'-CTT GAA GGG CAG CTG AAG CTG-3'
	cycle details	94°C 30 s, 60°C 45 s, 72°C 45 s
	amplicon size	180 bp
Ctsl^{F}	forward primer	5'-CAC ACA GAA GAC TGT ATG GC-3'
	reverse primer	5'-TCA AAC TCA GAA ATC TGC CTG-3'
	cycle details	94°C 30 s, 60°C 30 s, 72°C 40 s, 15 Cycles, then 94°C 30 s, 56°C 30 s, 72°C 40 s, 25 Cycles
	amplicon size	598bp (wildtype), 771bp (floxed allele)

***Atg7*^{F}**	forward primer	5'-TGG CTG CTA CTT CTG CAA TGA TGT-3'
	reverse primer	5'-CAG GAC AGA GAC CAT CAG CTC CAC-3'
	cycle details	94°C 30 s, 60°C 45 s, 72°C 150 s
	amplicon size	500 bp
***Atg7*^{wt}**	forward primer	5'-TTG CCA ACA TCC CTG GAT AC-3'
	reverse primer	5'-TGG CAC CCA CTG ACC AAT AG-3'
	cycle details	94°C 30 s, 60°C 45 s, 72°C 150 s
	amplicon size	800 bp
OT-I (*Tcra*)	forward primer	5'-CAG CAG CAG GTG AGA CAA AGT-3'
	reverse primer	5'-GGC TTT ATA ATT AGC TTG GTC C-3'
	cycle details	94°C 30 s, 62°C 60 s, 72°C 60 s
	amplicon size	300 bp
OT-I (*Tcrb*)	forward primer	5'-AAG GTG GAG AGA GAC AAA GGA TTC-3'
	reverse primer	5'-TTG AGA GCT GTC TCC-3'
	cycle details	94°C 30 s, 52°C 45 s, 72°C 45 s
	amplicon size	300 bp
***Tap1*^{KO}**	forward primer	5'-CTT GGG TGG AGA GGC TAT TC-3'
	reverse primer	5'-AGG TGA GAT GAC AGG AGA TC-3'
	cycle details	94°C 30 s, 64°C 30" -0,5°C per Cycle, 72°C 4 s 12 Cycles, then 58°C 30 s 25 Cycles
	amplicon size	280 bp
***Tap1*^{wt}**	forward primer	5'-AGG CTC AGC GTG CCA CTA AT-3'
	reverse primer	5'-ATT GAA GTT CCT GCG CCT CC-3'
	cycle details	94°C 30 s, 64°C 30" -0,5°C per Cycle, 72°C 4 s 12 Cycles, then 58°C 30 s 25 Cycles
	amplicon size	240 bp

DNA has been visualized by agarose-gel electrophoresis using 1-2% agarose / TAE gels.

TAE buffer (50X)	
	2 M Tris
	1 M acetic acid (5.71% v/v)
	50 mM EDTA

3.3 Animal experiments

All mice have been house in specific pathogen-free facilities at Klinikum rechts der Isar, Munich and the Georg-Speyer-Haus, Frankfurt/Main, with chow (standard formulation) and water supply ad libitum. Individually-ventilated cages

were used and maintained on a 12-hour light/dark cycle. All procedures were reviewed and approved by the Regierung of Oberbayern or the Regierungspräsidium Darmstadt, respectively. Appropriate certification has been obtained (FELASA). For experimental cohorts, age and sex-matched male and female mice at 6 to 12 weeks of age were used. In general, mice were housed in groups of 3-5 mice per cage, unless experimental procedures (e.g. supplemented chow) or individual behavior (e.g. fighting) required single housing.

3.3.1 *Tamoxifen Treatment*

In order to induce genetic recombination of loxP sites in mice carrying the *villin-cre*ER^{T2} allele or control mice were treated by five daily oral administrations of 1 mg tamoxifen (Sigma-Aldrich) dissolved in a 20% v/v ethanol / 80% v/v sunflower oil mixture. In the case of AOM-treated *Stat3*$^{\Delta IEC}$, *OVA*^{Vil}, *OVA*^{Vil}/*Stat3*$^{\Delta IEC}$ or control mice tamoxifen has been administered by tamoxifen-containing chow (Genobios, Laval, France, dosage 400 mg/kg).

3.3.2 *Intraperitoneal Injections*

Intraperitoneal (i.p.) injections have been performed with a microcannula (30 G) into the tightened abdominal skin. To induce colon tumors mice were injected i.p. with azoxymethane (AOM, Sigma-Aldrich, St. Louis, USA) once a week for 6 weeks at 10 mg/kg bodyweight. AOM has been diluted in 0.9% w/v NaCl solution and kept frozen until useage.

Chloroquine (Sigma-Aldrich) was i.p. injected at 60 mg/kg bodyweight in 0.9% w/v NaCl-solution, 3-MA (Sigma-Aldrich) at 30 mg/kg bodyweight in PBS, daily starting upon tamoxifen-treatment. Deferoxamine (DFO; Sigma-Aldrich) was dissolved in 0.9% w/v NaCl-solution and injected i.p. at 400 mg/kg every other day starting upon tamoxifen-treatment.

E64d (Santa Cruz Biotechnology, Dallas, USA) was dissolved in a 20% v/v ethanol / 80% v/v sunflower oil mixture and applied as oral gavage daily starting upon tamoxifen-treatment. n-acetyl-cysteine (Sigma-Aldrich) was dissolved in the drinking water at 0.5% w/v and applied continuously starting upon tamoxifen-treatment.

3.4 Human Samples

Human tumor samples were obtained from the tumor bank at the Institute of Pathology at Klinikum rechts der Isar, Munich or the Victoria Cancer Biobank, Melbourne. Samples have been analyzed per case and no assignment to groups (e.g. sex, age) have been performed. All procedures were performed with the approval of the respective ethics committees of the Technical University of Munich and the Victoria Cancer Biobank on samples from subjects that had given their written informed consent.

3.5 Histology and Immunohistochemistry

Intestinal tissue was embedded as “swiss rolles” (Moolenbeek and Ruitenberg, 1981) into paraffin blocks after overnight formalin-fixation (4% v/v paraformalaldehyde in PBS). Paraffin sections (3 µm) were prepared by microtomy and mounted on glass slides. After overnight drying they were stained using standard histological or immunohistochemical procedures as following:

3.5.1 *Hematoxylin/Eosin (H.E.)*

Slides were deparaffinized in xylol for 2 times 10 min, then rehydrated in descending ethanol dilutions (100%, 96%, 80%, 70%, 50% v/v in H_2O and dH_2O) 30 s each. Then slides were submerged in haematoxylin solution (Vector Labs, Burlingame, USA) for 1 min and washed twice with distilled water. Afterwards the tissue was stained for 10 s in a 3% eosin (Sigma-Aldrich) solution in water acidified

with 10 drops acetic acid per 100 ml and washed twice with dH_2O. Thereafter slides were dehydrated in ascending ethanol dilutions (50%, 70%, 80%, 96% and 100% v/v in H_2O) 30 s each and xylol 50 min. Cover slip was added on with tissue embedding medium (Vector Labs).

3.5.2 *Immunohistochemistry (IHC)*

Horseradish peroxidase-based IHC-staining was performed on slides dehydrated as above (xylol 2x10 min, 100%, 96%, 80%, 70%, 50% v/v ethanol and dH_2O 30 s each). Antigen-retrieval was achieved by boiling the slides in citrate buffer (pH 6.0, Vector Labs) for 20 min using a microwave. After cooling down, endogenous peroxidase signal has been blocked by adding 3% v/v H_2O_2 (Sigma-Aldrich) / H_2O for 10 min, followed by streptavidin blocking (2 drops / ml PBS, Vector Labs) for 30 min. Primary antibodies have been added thereafter in a 3% v/v BSA fraction V / 0.03% v/v triton X (both Sigma-Aldrich) / PBS solution containing 2 drops of Biotin (Vector Labs) for 16 hours at 4°C. Appropriate biotinylated donkey secondary antibodies have been added in 3% v/v BSA fraction V / PBS buffer and incubated for 30 min at room temperature. Meanwhile, avidin-biotin complex solution (VECTASTAIN Elite ABC kit, Vector Labs) has been incubated at 4°C and added for 30 min at room temperature thereafter. Subsequently, the slides have been incubated with freshly prepared DAB solution (DAB Peroxidase (HRP) Substrate Kit, Vector Labs) and stopped after color reaction was apparent. After each step slides have been washed with PBS twice. Then the slides have been counter-stained with hematoxylin (Vector Labs) for 1 min, washed, dehydrated and embedded as above.

3.5.3 *Immunofluorescence (IF)*

Immunofluorescence staining from paraffin-embedded tissue has been performed essentially similar to IHC, with the peroxidase blocking step omitted and

the streptavidin blocking replaced by blocking with 5% donkey serum (Vector Labs) / PBS. For immunofluorescence staining of cultured cells, these were grown on Lab-Tek II Chamber slides (Thermo Scientific) and fixed in 2% PFA/PBS at 4°C for 15 min and permeabilized with methanol at -20°C for 10 min.

Primary antibodies were diluted in 3% v/v BSA fraction V / 0.03% v/v triton X (both Sigma-Aldrich) / PBS solution and left overnight. Fluorescent-conjugated secondary antibodies were diluted in 3% v/v BSA fraction V / PBS buffer and incubated for 30 min at room temperature. Then the cover slips were mounted with DAPI-containing mounting medium (ProLong Gold Antifade, Thermo Scientific). Washing steps were carried out twice in PBS between each step.

3.5.4 *Antibodies Used for Immunohistology (IHC and IF)*

Target	Supplier	Identifier	Dilution
CD3	Dako	Cat# IS503; RRID:AB_779085	undiluted
pY705-STAT3	Cell Signaling	Cat# 9145; RRID:AB_2491009	1:200
pS727-STAT3 (mouse)	Cell Signaling	Cat# 9134S; RRID:AB_331589	1:100
cleaved Caspase-3	Cell Signaling	Cat# 9579; RRID:AB_10897512	1:250
LAMP2	Abcam	Cat# ab13524; RRID:AB_2134736	1:200
COXII	Proteintech	Cat# 55070-1-AP; RRID:AB_10859832	1:50
Cathepsin S	Santa Cruz	Cat# sc-6505; RRID:AB_2245620	1:250
OXPHOS	Abcam	Cat# ab110413; RRID: RRID:AB_2629281	1:100
pS727-STAT3 (human)	Abcam	Cat# ab30647; RRID:AB_779085	1:50
CD8 (human)	Cell Marque	108M-96; RRID:AB_1158208	1:100

Biotinylated secondary antibodies were anti-rabbit IgG (BA-1000) or anti-goat IgG (BA-5000, both Vector Labs). For IF fluorescent-labelled anti-rabbit IgG-Alexa Fluor 488 (A-21206, Thermo Scientific) and anti-rat IgG-Cy3 (Jackson ImmunoResearch, West Grove, USA) were used.

3.6 Microscopic Analyses

Light microscopy was performed on an AxioVision microscope and AxioImager software (Zeiss, Jena, Germany). Size of tumors was quantified by measuring the largest area of each tumor in serial sections (approx. 250 µm distance between single sections).

Analysis of subcellular structures was carried out on a SP5 confocal laser scanning microscope (Leica, Wetzlar, Germany) at 630X magnification. For detection of co-localizing particles those were visualized by sequential analysis to prevent fluorescent spill-over. Laser excitation used was 405 nm for DAPI, 488 nm for Alexa Fluor 488 and 561 nm for Cy3.

For transmission electron microscopy tissue samples from small intestines were excised, fixed with 2.5 % glutaraldehyde solution and stained with osmium tetraoxideaccording to standard procedures.

3.7 Isolation of Intestinal Epithelial Cells

For IEC isolation intestines have been opened longitudinally, cleared of mucus, cut into small pieces (approx. 5 mm) and incubated in PBS containing 5 mM EDTA and 2 mM DTT with gentle agitation at 37°C for 10 Minutes. Epithelial cells were then separated from underlying tissue by heavy vortexing and subsequent centrifugation at 400 g for 5 min at 4°C.

3.8 Protein Analysis

For extraction of cytosolic proteins pelleted cells were dissolved in subcellular extraction buffer and incubated for 15 min on ice. 1 tablet of protease inhibitor cocktail (Roche Diagnostics, Mannheim, Germany) was added per 50 ml of buffer. Heavy membrane particles were pelleted at 10.000 g for 10 min. and dissolved in modified RIPA buffer with protease inhibitors and cleared of lipids by additional

centrifugation at 17.000 g for 12 min. For whole cell extracts cells pelleted, dissolved in modified RIPA buffer as above and cleared of lipids by additional centrifugation at 17.000 g for 12 min in presence of protease inhibitors.

Subcellular Extraction Buffer
25 μg/ml digitonin
250 mM sucrose
20 mM Hepes
10 mM KCl
1.5 mM $MgCl_2$
1 mM EDTA
1 mM EGTA
pH 7.5 with KOH or HCl
modified RIPA buffer
50 mM Tris-HCl
250 mM NaCl
25 mM sodium pyrophosphate
3 mM EDTA
3 mM EGTA
1 mM DTT
1% Triton X
0.5%, Igepal CA-630
10% Glycerol
pH 7.5 with HCl or NaOH
Protease / Phosphatase Inhibitors
“complete” protease inhibitor (1 tablet per 50 ml)
50 mM β-glycerophosphate
5 mM sodium orthovanadate
25 mM sodium fluoride
2 nM phenylmethane sulfonyl fluoride

All compounds listed purchased from Sigma-Aldrich or Carl Roth (Karlsruhe, Germany) except “complete” protease inhibitor was purchased from Roche Diagnostics, Mannheim, Germany.

3.8.1 *Immunoblotting*

Immunoblotting was performed as polyacrylamide gel electrophoresis under denaturating and reducing conditions. For gel preparation, acrylamide, resolving gel buffer and dH_2O were mixed thoroughly and poured into a glass chamber. As starting radicals 50 µl of a 10 % w/v stock ammonium persulfate and 5 µl tetramethylethylenediamine (TEMED) were added. During polymerization the gel was overlayered with isopropanol.

After polymerization of the resolving gel was complete, isopropanol was removed and the stacking gel solution consisting of acrylamide, stacking gel buffer and dH_2O was added and polymerization induced with starting radicals as above.

Resolving Gel Buffer
1.5 M Tris (pH 8.8 with NaOH)
0.4% w/v SDS
Stacking Gel Buffer
0.5 M tris (pH 6.8)
0.4% w/v SDS

Gel:	**Acrylamide (40% w/v stock)**	**Buffer**	**dH_2O**
5%	1.25 ml	2.5 ml	6.25 ml
7.5%	1.87 ml	2.5 ml	6.63 ml
8%	2 ml	2.5 ml	5.5 ml
10%	2.5 ml	2.5 ml	5 ml
12%	3 ml	2.5 ml	4.5 ml
15%	3.75 ml	2.5 ml	3.75 ml

Concentration of protein samples was determined by mixing 2 µl of sample with 1 ml of a Bradford-based dye (Bio-Rad Protein Assay, Bio-Rad, Philadelphia, USA, dilution 1:6 in dH_2O). The absorbance at 595 nm was determined by photometry and calculated using serial dilutions of BSA as standard curve.

Protein samples (approx. 30 µg) were diluted to a volume of 20-30 µl with RIPA buffer, then Laemmli buffer was added and the samples were incubated at 95°C for 5 min. After brief spin the proteins were loaded carefully onto the gel prepared as above.

Laemmli Buffer (4X)
200 mM tris (pH 6,8 with HCl)
8% w/v SDS
40% v/v glycerol
0,4% w/v bromphenole blue
5% v/v β-mercaptoethanol

(all reagents from Sigma-Aldrich or Carl Roth)

The gel was placed in a chamber filled with running buffer (diluted with dH_2O to 1X) and electric current was applied to allow movement of proteins from cathode (-) to anode (+). For protein resolution constant voltage mode was used. While proteins were in stacking gel, currency of 70 V was applied, when moved into the resolving gel currency was stepwise increased to 120 V.

After the resolution was completed, the gel was taken out of the chamber and placed in a transfer chamber. For the blotting, PVDF membrane (Immobilon-P, Merck-Millipore, Darmstadt, Germany) was used and activated with methanol for 1 min before placing it directly adjacent to the gel in the blotting chamber. The blotting chamber was performed by the tank (wet) transfer method with transfer buffer containing 20% methanol. Electric current was applied in the constant amperage mode with 350 mA for 90 min at 4°C with the gel at the cathode and the membrane at the anode.

Running Buffer (10X)	
	9.5 M glycine
	0.25 M Tris
	35 mM SDS
Transfer Buffer (10X)	
	9.5 M glycine
	0.25 M Tris
PBST	
	PBS
	0.1% Tween 20

(all reagents from Sigma-Aldrich or Carl Roth)

Membranes were then taken out, blocked in 3% milk/PBST for 30 min at room temperature on a rocking platform and probed with antibody in 3% milk/PBST (STAT3, Gapdh, β-Actin) or 3% BSA /PBST (all other) at 4°C overnight or for 2 hours at room temperature while agitated. Thereafter membrane has been washed three times 10 min each with PBST, then incubated with horseradish peroxidase (HRP)-linked secondary antibody (GE Healthcare, Buckinghamshire, UK or Santa Cruz).

Signal has been detected using the SuperSignal West Pico PLUS Chemiluminescent Substrate kit (Thermo Scientific) and Hyperfilm ECL (GE Healthcare). For re-probing signal was removed by Restore Western Blot stripping buffer (Thermo Scientific) for 10 min at 37°C with gentle agitation.

Target	Supplier	Identifier	Dilution
LC3	Cell Signaling	Cat# 2775; RRID: AB_915950	1:500
phospho-DRP1	Cell Signaling	Cat# 4494S; RRID:AB_11178659	1:500
STAT3	BD	Cat# 610190; RRID:AB_397589	1:2000
p62	Progen	Cat# GP62-C; RRID:AB_2687531	1:1000
MHC-I	Santa Cruz	Cat# sc-59199; RRID:AB_1126186	1:50
Gapdh	Santa Cruz	Cat# sc-32233; RRID:AB_627679	1:1000
β-actin	Sigma	Cat# A4700; RRID:AB_476730	1:3000
Cathepsin B	Abcam	Cat# ab58802; RRID:AB_940824	1:400

3.9 Isolation of Lamina Propria Cells

For the isolation of lamina propria cells intestines of mice were placed in supplemented RPMI, opened longitudinally, cleared of mucus, chopped into small pieces and digested in digestion buffer for 15 - 20 min. at 37°C while gently shaking. Then the digestion was interrupted by 15 s heavy vortexing and the tube placed on ice. Liberated cells in the supernatant were collected and placed on ice. To stop the digesting enzymes, 5 mM EDTA was added to the cell suspension.

The remaining tissue has been subjected to 2 additional digestion steps for 15 - 20 min using fresh digestion medium. Following the third digestion step all fractions were combined and passed through a 70 µm strainer (BD) and the cells centrifuged for 5 min at 400 x g at 4°C. Then the supernatant was discarded and the cell pellet resuspended in supplemented RPMI containing 10% FCS.

For intracellular staining cells were *ex vivo* restimulated in supplemented RPMI with 10% FCS, containing either 1 µg/ml ionomycin and 20 ng/ml phorbol-myristate-acetate (for T cells) or 0.1 µg/ml LPS (for DC, all Sigma-Aldrich) in presence of

Golgi-Plug (BD, 1:1000) for 5 hours at 37°C. Volume of 1 ml in a 24-well plate was used per sample.

	Component	Supplier
Supplemented RPMI		
	RPMI	Thermo Scientific
	10 mM Hepes	Sigma-Aldrich
	2 mM L-Glutamine	Thermo Scientific
	Non-essential amino acids (1:100)	Thermo Scientific
	1 mM sodium pyruvate	Thermo Scientific
	100 U Penicillin/Streptomycin	Thermo Scientific
	2% v/v fetal calf serum	Thermo Scientific
Digestion Buffer		
	supplemented RPMI (as above)	
	1 mg/ml Collagenase I (C0130)	Sigma-Aldrich
	1 mg/ml Dispase II	Roche
	20 μg/ml DNase I	Sigma-Aldrich

3.10 Flow Cytometry

Flow cytometric analysis was performed on a Gallios flow cytometer (Beckman-Coulter, Brea, USA), FACSCalibur, FACSCantoII or LSRFortessa (all BD). The cell suspension was prepared by labelling with the appropriate antibody cocktail. For exclusion of dead cells with Live/Dead Fixable Blue Dead Cell Stain Kit (final dilution 1:100 in PBS) was used. Appropriate isotype control antibodies were purchased from Thermo Scientific. For TCR Vβ profiling, the Anti-Mouse TCR Vβ Screening Panel kit (BD, Cat.# 557004) consisting of 15 FITC-conjugated Vβ specific antibodies together with FITC-conjugated TCRγδ antibody (Thermo Scientific, Cat.# 11-5711-82) has been used.

For intracellular staining, cells were prestained with 0.5 μg/ml ethidium bromide monoazide (Sigma-Aldrich) for 15 min in bright light or Live/Dead Fixable

Blue Dead Cell Stain Kit, fixed in IC-fixation buffer for 30 Minutes on ice and stained in permeabilization buffer (diluted 1:10 in dH_2O, all Thermo Scientific).

SIINFEKL-MHC-I pentamer was purchased from ProImmune (Oxford, UK, cat. no. F093-2B-E) and used at final dilution of 1:20 per sample for 20 min at room temperature in staining buffer. B-cells were identified by co-staining for B220 and excluded from analysis.

FACS-sort has been performed on a FACSAria or FACSAria Fusion (all BD) in sort buffer in presence of propidium iodide (final concentration 0.5 μg/ml). For sorting cells isolated from intestinal lamina propria, nozzle size of 100 μm and a sort rate of approx. 1000 events/s was used. Sorted cells have been collected in RNAprotect Cell reagent (Qiagen).

	Component	Supplier
Staining Buffer		
	PBS	Thermo Scientific
	2% v/v FCS	Thermo Scientific
Sort Buffer		
	PBS	Thermo Scientific
	5 mM EDTA	Sigma-Aldrich
	2 % v/v BSA	Sigma-Aldrich

The following fluorescent-conjugated antibodies were used (all at dilution 1:200):

Target	Supplier	Identifier
CD3-Alexa Fluor 700	Thermo Scientific	Cat# 56-0032; RRID:AB_529508
CD4-eFluor 450	Thermo Scientific	Cat# 48-0042; RRID:AB_1272194
CD8α-APC	Thermo Scientific	Cat# 17-0081; RRID:AB_469334
IFNγ-PerCP-Cy5.5	Thermo Scientific	Cat# 45-7311; RRID:AB_1107020
CD11c-FITC	Thermo Scientific	Cat# 11-0114; RRID:AB_464941
CD11b-APC-eFluor 780	Thermo Scientific	Cat# 47-0112; RRID:AB_1603193
CD80-PE-Cy7	Thermo Scientific	Cat# 25-0801; RRID:AB_2573369
Gr-1-Alexa Fluor 700	Thermo Scientific	Cat# 56-5931; RRID:AB_494007
F4/80-APC	Thermo Scientific	Cat# 17-4801; RRID:AB_469452
EpCAM-eFluor 450	Thermo Scientific	Cat# 48-5791; RRID:AB_10717090
Foxp3-PE	Thermo Scientific	Cat# 12-5773; RRID:AB_465936
B220-efluor 450	Thermo Scientific	Cat# 48-0452; RRID:AB_1548761
SIINFEKL-H2Kb	Thermo Scientific	Cat# 12-5743; RRID:AB_925774
CD45-BV786	BD	Cat# 564225; RRID:AB_2716861
IL-12-PE	BD	Cat# 554479; RRID:AB_395420
biotinylated CD11c (MACS)	BD	Cat# 553800; RRID:AB_395059
CD45-APC-efluor 780	Thermo Scientific	Cat# 47-0451; RRID:AB_1548790
CD11c-efluor 450	Thermo Scientific	Cat# 48-0114; RRID:AB_1548665
H-2Kb-Percp-Cy5.5	BD	Cat# 562831; RRID:AB_2732002
H-2Dd-PE	BD	Cat# 553580; RRID:AB_394938

3.11 Cell Culture

3.11.1 *Plasmids*

Plasmids expressing mutant *Stat3* have been obtained from Andrew Larner (Wegrzyn et al., 2009). In brief, the plasmids containing a MSCV-promoter, the mitochondrial localization sequence of human *Cox8a*, murine *Stat3* cDNA in wildtype or mutant form as indicated, an internal ribosomal entry site (IRES) and EGFP. Each plasmid has been co-transfected with plasmids expressing ecotropic

gag/pol and *env* for γ-retroviral transduction in HEK-293T cells. Culture supernantant has been used to transduce *Stat3*$^{-/-}$ mouse embryonic fibroblasts (provided by Thomas Decker).

The vector pCI-OVA has been generated by inserting the OVA-cassette amplified from DEC205-OVA (Loschko et al., 2011) using a primer specific for *ova* cDNA with NheI or NotI restriction sites at their 5' end, respectively. The fragment has been amplified by PCR and purified by gel electrophoresis. It has then been ligated into the pCI-neo vector (Promega #TB215) digested previously with NheI and NotI.

3.11.2 *Cell Lines*

The murine colon carcinoma cell lines CMT93 was obtained from ATCC (Manassas, USA). Cells were cultured under standard conditions using Dulbecco's modified Eagle's medium (DMEM) supplemented with 10% FCS and 1% Penicillin-Streptomycin at 37°C, 5% CO_2. CMT93 cells were transfected with an expression vector encoding chicken ovalbumin cDNA (pCI-OVA). Transfection has been performed using Lipofect 2000 (Thermo Scientific) on 6-well plates using 3 µg plasmid DNA and 5 µl Lipofect 2000 per well. One day after transfection cells were transferred into 10 cm dishes and incubated with culture medium containing 1.5 mg/ml geneticin (Thermo Scientific). About 10 days later stable clones were selected by colony picking and termed OVA-CMT. Expression level of *Ova* has been determined by immunoblot or qPCR.

CT26 cells transfected with an expression vector encoding ovalbumin along with EGFP (pCI-OVA-IRES-GFP), termed OVA-CT26, were described previously (Gamrekelashvili et al., 2007) and donated from Jaba Gamrekelashvili and Tim F. Greten.

3.11.3 *RNAi-Mediated Gene Silencing*

Stable knockdown of Stat3 was achieved by transfection of OVA-CMT or OVA-CT26 cells with pcDNA6.2-Stat3-miRNA (containing a synthetic Stat3-binding pre-miRNA: TCGTGAAACGTGAGCGACTCAAACTGGTTTTGGCCACTGACTGACCAGTT TGACGCTCACGTTT; target sequence: CAGTTTGAGTCGCTCACGTTT) or pcDNA6.2-scrambled from BLOCK-it Pol II miR RNAi Expression Vector Kit (Thermo Scientific #K493600), after removal of the EmGFP-expression cassette by restriction with DraI. Clones were selected using supplemented DMEM containing 10 µg/ml blasticidin S (Thermo Scientific) and successful knockdown of Stat3 protein was confirmed by immunoblot analysis.

For siRNA-mediated knockdown-experiments a pool of 4 pre-validated siRNAs ("ON-TARGETplus-smart pool") per gene was purchased from Dharmacon/GE Healthcare and transfected using DharmaFECT 4 (Dharmacon) or Viromer green (Lipocalyx, Halle, Germany) for OVA-CMT or OVA-CT26 cells, respectively. For transfection of one well on a 6-well plate using DharmaFECT 4, 100 pmol siRNA was added to 50 µl of Opti-MEM (Thermo Scientific) and 2,5 µl of DharmaFECT 4 was mixed with 50 µl Opti-MEM in separate tubes. These were incubated at room temperature for 5 min, then combined and incubated at room temperature for 20 min to allow complex formation. Then the solution was added to 900 ml of DMEM/10 % FCS and transferred into the well. For transfection using Viromer green, 100 pmol siRNA was added to 6 µl of 10 mM NaCl solution. Viromer green was diluted at 1.5 µl to 50 µl of buffer F (Lipocalyx). Those solutions were incubated at room temperature for 5 min, then combined and incubated at room temperature for 20 min to allow complex formation. Then the solution was added to 900 ml of DMEM / 10 %

FCS and transferred into the well. Cells were seeded one to two days prior to reach approx. 30 % confluency at transfection.

3.12 T Cell Activation Assay

In T cell activation assays OVA-CMT cells were pretreated with H_2O_2 at 1 mM, E64d (10 µg/ml) or DMSO (all Sigma-Aldrich) for 2 hours at 37°C and washed in cell culture medium. Then $5x10^4$ OVA-CMT cells were added to $5x10^5$ OT-I splenocytes into a 96-well plate and incubated at 37°C for 2 days. IFNγ levels in supernatants were determined by ELISA (DY485, R&D Systems) according to the manufacturer's instructions.

In co-culture experiments using purified DC and $CD8^+$ T cells, DC were prepared from the spleen of C57B/6 wildtype or *Tap1*$^{-/-}$ mice 14 days after s.c. injection of $5x10^6$ Flt3L-expressing B16 melanoma cells (Mach et al., 2000) or from Balb/c wildtype mice. DC were labeled with a biotinylated CD11c-antibody (553800, BD) and sorted using MACS-separation columns (Miltenyi, Bergisch-Gladbach, Germany) according to the manufacturer's instructions. Splenic OT-I $CD8^+$ T cells were magnetically purified by negative selection using $CD8a^+$ T cell isolation kit II (130-095-236, Miltenyi). Purity was confirmed by flow cytometry and found to be greater than 95%. $5x10^4$ CMT-OVA or OVA-CT26 cells were pretreated for 2 hours with 1 mM H_2O_2, washed and incubated with $2x10^5$ OT-I $CD8^+$-T cells with indicated amount of DC. Experiments were performed at least two times in triplicates.

3.12.1 *Cross-Dressing Experiments*

For MHC class I transfer studies purified DC from C57B/6J or *Tap1*$^{-/-}$ (on C57B/6J background) mice were incubated with OVA-CT26 cells for 12-16 hours at 37°C. The cells then were stained with anti-CD45-APC-efluor 780 (47-0451-82), anti-CD11c-efluor 450 (48-0114-82, all Thermo Scientific), anti-H-$2K^b$–Percp-Cy5.5

(562831) and anti-H-2D^d-PE antibodies (553580, all BD) and analyzed by flow cytometry. The cells CD45$^+$CD11c$^+$GFP$^-$ were identified as DC and analyzed for (surface) expression of H-2D^d.

3.12.2 *LMP Quantification*

For quantification of LMP, cells were incubated in DMEM (Thermo Scientific) supplemented with 10% FCS and 1% Penicillin-Streptomycin in presence or absence of H_2O_2 (Sigma-Aldrich) at 1 mM for 2 hours. Then the cells were washed and cultured in supplemented DMEM for another 6 hours. Then cells were detached using Trypsin-EDTA (Thermo Scientific), and incubated with 50 ng/ml acridine orange (Calbiochem/Merck, Darmstadt, Germany) in supplemented DMEM for 15 min. at 37°C. Then cells were washed in PBS and analysed by flow cytometry at 488 nm excitation and 620±30 nm emission to quantify the red fluorescence of the lysosomal compartment. Where indicated cells were pre-incubated with rotenone (25 µM), antimycin A (100 µM) or DMSO overnight and with DFO (1 mM, all Sigma-Aldrich) for 1 hour prior to H_2O_2-stimulation.

3.13 Metabolic analyses

3.13.1 *Cathepsin Activity*

Protease activity of the cathepsin family activity was measured using cytosolic fractions generated as stated above in presence of pefabloc (1 µM). Assay was performed in triplicates in a reaction buffer using 2 µg of protein lysate and 10 µM protease substrate z-LR-AMC (ES008, R&D Systems). Increase of fluorescence was measured at 390/485 nm on a spectrophotometer (Fluostar Omega, BMG Labtech, Ortenberg, Germany) and slope (ΔE/t) was calculated at linear phase.

Reaction Buffer	Component	Supplier
	50 mM sodium acetate	Sigma-Aldrich
	8 mM EDTA	Sigma-Aldrich
	1 mM DTT	Sigma-Aldrich
	1 µM pefabloc	Sigma-Aldrich
	dH_2O	

3.13.2 *Intracellular Iron*

Iron content was assessed by confocal live cell microscopy of cells grown on chambered optical coverslips (µ-slides, Ibidi, Martinsried, Germany) incubated in phenol-red free medium in presence of the Fe^{2+}-sensitive probe IP-1 at 20 µM and Hoechst 33342 (Sigma-Aldrich) at 1 µg/ml and, where indicated, with LysoTracker red DND-99 (Thermo Scientific) at 25 nM for 30 min. Where indicated cells were pre-treated overnight with rotenone (25 µM), antimycin A (100 µM) or DMSO (all Sigma-Aldrich).

3.13.3 *Respiratory Activity*

The oxygen consumption of trypsinized OVA-CMT93^{scr} and OVA-CMT93^{STAT3KD} cells was determined at 37 °C using an Oxygraph-2k (Oroboros, Innsbruck, Austria). In each case, $3x10^6$ cells were suspended in 2 ml pre-warmed FCS-supplemented DMEM medium and transferred into one of the two Oxygraph-chambers. 10 synchronous measurements with both cell lines were performed. Oxygen consumption rates (OCR) were determined after stabilization of the flux signal (1st deviation of the change in oxygen concentration) by using the 'mark tool' of the DatLab5 control software (Oroboros). After recording the basal respiration (basal OCR), oligomycin (Sigma-Aldrich; 2 µg/ml) was added to inhibit mitochondrial adenosine-triphosphate (ATP) synthesis. Subsequently carbonyl

cyanide-p-trifluoromethoxyphenylhydrazone (FCCP, Sigma-Aldrich) was added stepwise to assess maximal capacity of the mitochondrial electron-transfer chain (maximal OCR) that occurred usually at 4.5 – 5.5 µM of the uncoupler. Finally, 2 mM KCN (Sigma-Aldrich) was added to determine the mitochondria-independent oxygen consumption of the cells.

3.13.4 *Energy Metabolism*

In order to quantify the glucose uptake $5x10^5$ cells were incubated in supplemented DMEM in presence of 5 mg/ml glucose for 24 hours. Then glucose concentration in the supernatant was assayed using the Glucose Assay Kit (Sigma-Aldrich) according to the manfacturer's instructions and substracted from initial concentration.

Total cellular adenosine-triphosphate (ATP) content was measured based on luciferase activity using the kit CellTiter-Glo (Promega, Madison, USA) according to the manufacturer's instructions using $5x10^4$ cells. Cell proliferation was assayed by seeding 10^4 OVA-CMT93 cells and counting the cell number using an automated cell counter (CASY, Roche Innovatis, Reutlingen, Germany) after 84h culture in glucose and pyruvate-free DMEM (Thermo Scientific) supplemented with 10% FCS and glucose (5 mg/ml), galactose (5 mg/ml), 2-deoxyglucose (1.5 mg/ml) or 3-bromopyruvate (100 µM, all Sigma-Aldrich) as indicated.

3.13.5 *Mitochondrial Content and Turnover*

The mitochondrial compartment of cells was measured by flow cytometry following incubation of cells with MitoTracker deep red (250 nM, Thermo Scientific) in conventional cell culture medium for 30 minutes at 37°C. To estimate the mitochondrial membrane potential cells were incubated with tetramethylrhodamin-methylester (TMRM, 50 nM) in HBSS supplemented with 10 mM Hepes (all Thermo

Scientific) for 30 minutes at 37°C and subjected to flow cytometry at ex/em 561/610-20 BP.

MitoTimer was expressed in OVA-CMT^{scr} or OVA-CMT^{Stat3KD} cells by co-transfecting cells with pTRE-Tight-MitoTimer (Hernandez et al., 2013) and pES.1–2(M2N)p (containg reverse tetracycline-responsive transactivator M2 (Urlinger et al., 2000)) using Lipofectamine 2000 (Thermo Scientific) as described above. 2 days after transfection cells were seeded in triplicates, treated with doxycycline (Sigma-Aldrich) at 2 µg/ml for 1 hour, then incubated for additional 48 hours in conventional cell culture medium and treated with doxycycline for 2 hours. Cells were then analyzed by flow cytometry for fluorescence at 530/30 nm and 585/42 nm at excitation of 488 nm for new and old mitochondria, respectively.

NAD^+/NADH ratio was measured using fresh tissue of small intestine and the NAD/NADH Assay Kit (ab65348, Abcam) according to the manufacturer instructions.

Citrate synthase activity was assayed using mitochondria isolated from small intestine epithelial cells resuspended in 0.25 M sucrose, 10 mM Tris, 1 mM EDTA, ph 7.2 passed 15 times through a 21G-needle. Unbroken cells were pelleted at 750 g for 5’ and discarded. The supernatant was subjected to centrifugation at 9,000 g for 15’ and the pellet resuspended in 0.25 M sucrose, 2 mM HEPES, 0.1 mM EGTA, pH 7.4 (with KOH) and used as crude mitochondrial fraction. To release matrix enzymes mitochondria were pelleted at 10,000 g for 15’ and resuspended in 25 mM potassium phosphate buffer, pH 7.2, 5 mM $MgCl_2$ and subjected to 3 freeze-thaw cycles. The assay was performed adding acetyl CoA (0.1 mM) and oxaloacetic acid (0.1 mM) in buffer containing 50 mM KPi, pH 7.4, 0.1 mM 5,5’-dithio-bis-(2-nitrobenzoic acid;

DTNB, all Sigma-Aldrich or Carl Roth) and slope (ΔE/t) was measured at 412 nm using a spectrophotometer (SpectraMax 340, Molecular Devices, Sunnyvale, USA).

3.14 Gene Expression Analyses

Total RNA was extracted from snap-frozen tissue, isolated enterocytes or cultured cells using the RNeasy Mini kit (Qiagen, Hilden, Germany) according to the manufacturer's instructions. SuperScript II Reverse Transcriptase (Thermo Scientific) was used for synthesis of cDNA from 1 µg total RNA. Real-time PCR analysis using Fast-Start Universal SYBR Green PCR Master Mix (Roche Diagnostics) was performed on a StepOne Plus Real-Time PCR system (Thermo Scientific). Data has been normalized to the mRNA level of a housekeeping gene (cyclophilin A) using the delta C_T method ($2^{CTcyclo-CTgene}$). Primer sequences were as following:

Primer	Sequence
Aco1-F	AGAACCCATTTGCACACCTTG
Aco1-R	AGCGTCCGTATCTTGAGTCCT
Alpi-F	AACTCACCTCATGGGCCTCTT
Alpi-R	GGGTTTCGGTTGGCATCATA
Atp5l-F	AAGGAAGCTGTGCTGAATGG
Atp5l-R	ATGCCACGTTTGCCTATGA
Ccl17-F	CAAGCTCATCTGTGCAGACC
Ccl17-R	CGCCTGTAGTGCATAAGAGTCC
Ccl2-F	CAGCCAGATGCAGTTAACGC
Ccl2-R	AGCCTACTCATTGGGATCATCTTG
Ccl20-F	TGGCAAGCGTCTGCTCTTC
Ccl20-R	TTGCTGCTTCTGCCTGGC
Ccl22-F	TCATGGCTACCCTGCGTGTC
Ccl22-R	CCTTCACTAAACGTGATGGCAGAG
Ccl25-F	TGGATGCCGGTTGTCCAT
Ccl25-R	TTCCATTTGATCCTGTGCTGG
Ccl28-F	AGCAGGGCTCACACTCATGG
Ccl28-R	ACCTCAGTGCAACAGCTGGAG
Ccl3-F	CCAAGTCTTCTCAGCGCCAT
Ccl3-R	TCTTCCGGCTGTAGGAGAAGC
Ccl4-F	AGCTCTGCGTGTCTGCCCT

Ccl4-R	TGCTGAGAACCCTGGAGCA
Ccl5-F	GTGCTCCAATCTTGCAGTCGT
Ccl5-R	TGAACCCACTTCTTCTCTGGGT
Chga-F	TCCCCACTGCAGCATCCAGTTC
Chga-R	CCTTCAGACGGCAGAGCTTCGG
Cp-F	ATTTTCAACGGGCTGATGACA
Cp-R	GGAGTGGTAAATCCTGGTCACA
Cphn-F	ATGGTCAACCCCACCGTGT
Cphn-R	TTCTGCTGTCTTTGGAACTTTGTC
Cst3-F	CGCCATACAGGTGGTGAGAG
Cst3-R	GGCACGCTGTAGATCTGGAA
Ctsb-F	CCCGACCATTGGACAGATTAGA
Ctsb-R	CACTGCCCCAAATGCCC
Ctsl-F	GGGTTGTGTGACTCCTGTGAAG
Ctsl-R	AACCCGATGCGCTAAACG
Ctss-F	AGCTGCCACGTGTTCAAGGT
Ctss-R	TGGCCACTGCTTCTTTCAGG
Cxcl10-F	GAATCCGGAATCTAAGACCATCAA
Cxcl10-R	GTGCGTGGCTTCACTCCAGT
Cxcl11-F	GCACCTCTTTCAGTCTGTTTCCTG
Cxcl11-R	AGCCATCCCTACCATTCATTCAC
Cxcl9-F	GAACGGAGATCAAACCTGCC
Cxcl9-R	TCTTTTCCCATTCTTTCATCAGC
Defa-F	TCAAGAGGCTGCAAAGGAAGAGAAC
Defa1-R	TGGTCTCCATGTTCAGCGACAGC
Eno1-F	GAGGCGCTTAGTGCTGCT
Eno1-R	AGAATAGACATGGCGAATTTCTG
Fh1-F	GCACCCCAATGATCATGTTA
Fh1-R	CATTGCTGTGGGAAAGGTG
Fth1-F	CAAGTGCGCCAGAACTACCA
Fth1-R	GCCACATCATCTCGGTCAAAA
Ftl1-F	CCATCTGACCAACCTCCGC
Ftl1-R	CGCTCAAAGAGATACTCGCC
G6pd2-F	CTGAATGAACGCAAAGCTGA
G6pd2-R	CAATCTTGTGCAGCAGTGGT
Gck-F	CCCTGAGTGGCTTACAGTTC
Gck-R	ACGGATGTGAGTGTTGAAGC
Glut1-F	ATGGATCCCAGCAGCAAG
Glut1-R	CCAGTGTTATAGCCGAACTGC
Heph-F	GTGGTCTATACCAACTGATGGGG
Heph-R	GGGAGCATAGTTCCACTGCATA
Ifnb-F	AGCTCCAAGAAAGGACGAACAT

Ifnb-R	GCCCTGTAGGTGAGGTTGATCT
Ifng-F	TTACTGCCACGGCACAGTCA
Ifng-R	AGTTCCTCCAGATATCCAAGAAGAGA
Il12p35-F	CACGCTACCTCCTCTTTTTG
Il12p35-R	CAGCAGTGCAGGAATAATGTT
Il6-F	ATGGTACTCCAGAAGACCAGAGGA
Il6-R	GTATGAACAACGATGATGCACTTG
Ireb2-F	TTCTGCCTTACTCAATACGGGT
Ireb2-R	AGGGCACTTCAACATTGCTCT
Lyz1-F	GAGACCGAAGCACCGACTATG
Lyz1-R	CGGTTTTGACATTGTGTTCGC
Mt1a-F	AAGAGTGAGTTGGGACACCTT
Mt1a-R	CGAGACAATACAATGGCCTCC
Mt2-F	GCCTGCAAATGCAAACAATGC
Mt2-R	AGCTGCACTTGTCGGAAGC
Mt3-F	ACCTGCCCCTGTCCTACTG
Mt3-R	CCTTGGCACACTTCTCACATC
Mtf1-F	TGCCTTTTCTGGTGGAAGGT
Mtf1-R	TACGTAACCCTGGGACATTGC
Mtf2-F	TCAAACGTCTACCGTTACAGTG
Mtf2-R	CAGGGTGCAATCTATCCCAGT
Muc2-F	CCCAGAAGGGACTGTGTATG
Muc2-R	TGCAGACACACTGCTCACA
Olfm4-F	GCCACTTTCCAATTTCAC
Olfm4-R	GAGCCTCTTCTCATACAC
Pck1-F	CCCAGGAGGTGAGGAAGTTTG
Pck1-R	GGAGCCGTCGCAGATGTG
Pdk1-F	GTTGAAACGTCCCGTGCT
Pdk1-R	GCGTGATATGGGCAATCC
Pfkfb3-F	ACTACTAGAGAGAGGAGACACATGATCCT
Pfkfb3-R	CGCACACCGACTCGATGA
Pfkl-F	CCATGGACGAGGAGAGGTT
Pfkl-R	TCCAGTTGTTCTCAAAGCTCCT
Pir-F	AAGTGAAGAGATCCCGAAACCC
Pir-R	GCGAGTGTAAACCTTCGACTTT
Pklr-F	CTTGCTCTACCGTGAGCCTC
Pklr-R	ACCACAATCACCAGATCACC
Slc40a1-F	TGGAACTCTATGGAAACAGCCT
Slc40a1-R	TGGCATTCTTATCCACCCAGT
Tap1-F	TCACCATGGGACACATGCAC
Tap1-R	ATGGACTCGCACACGTTGG
Tfrc-F	GTTTCTGCCAGCCCCTTATTAT

Tfrc-R	GCAAGGAAAGGATATGCAGCA
Tnfa-F	ACTCCAGGCGGTGCCTATG
Tnfa-R	GAGCGTGGTGGCCCCT
Villin-F	TTCTACGGTGGTGACTGCTACC
Villin-R	TGGTCCAACAGGACGGCTTGAT

3.15 NGS-Based TCR Repertoire Analysis

NGS-based TCR repertoire analysis was performed by Repertoire Genesis Inc. (Osaka, Japan). Total RNA was converted to complementary DNA (cDNA) with Superscript III reverse transcriptase (Thermo Scientific). BSL-18E primer containing polyT$_{18}$ (see below) and a *Sph*I site was used for cDNA synthesis. After cDNA synthesis, double strand (ds)-cDNA was synthesized with *E. coli* DNA polymerase I, *E. coli* DNA Ligase, and RNase H. ds-cDNAs were blunted with T4 DNA polymerase (all Thermo Scientific). P10EA/P20EA adaptor was ligated to the 5' end of the ds-cDNA and then cut with *Sph*I restriction enzyme. After removal of adaptor and primer with MinElute Reaction Cleanup kit (Qiagen), PCR was performed with KAPA HiFi DNA Polymerase (Kapa Biosystems, Woburn, USA) using either TCR α-chain constant region-specific (mCA1) or TCR β-chain constant region-specific primers (mCB1) and P20EA (Table S1). PCR conditions were as follows: 98°C (20 sec), 65°C (30 sec), and 72°C (1 min) for 20 cycles. The second PCR was performed with either mCA2 or mCB2 and P20EA primers using the same PCR conditions. Amplicons were prepared by amplification of the second PCR products using P22EA-ST1-R and either mCA-ST1-R or mCB-ST1-R. After PCR amplification, index (barcode) sequences were added by amplification with Nextera XT index kit v2 set A (illumina, San Diego, USA). The indexed products were mixed in an equal molar concentration and quantified by a Qubit 2.0 Fluorometer (Thermo Scientific). Sequencing was done with the Illumina Miseq paired-end platform (2 x 300bp). Assignment of sequences was performed by determining sequences with the highest identity in a data set of

reference sequences from the international ImMunoGeneTics information system (IMGT) database (http://www.imgt.org). Data processing, assignment, and data aggregation were automatically performed using repertoire analysis software originally developed by our group (Repertoire Genesis, RG). RG implemented a program for sequence homology searches using BLATN, an automatic aggregation program, a graphics program for TRV and TRJ usage, and CDR3 length distribution. Sequence identities at the nucleotide level between query and entry sequences were automatically calculated. Nucleotide sequences of CDR3 regions ranged from conserved Cysteine at position 104 (Cys104) of IMGT nomenclature to conserved Phenylalanine at position 118 (Phe118) and the following Glycine (Gly119) was translated to deduced amino acid sequences. Sequence read having identical TRV, TRJ and deduced amino acid sequence of CDR3 was defined as unique read. The copy number of unique reads were automatically counted by RG software in each sample and then ranked in order of the copy number. Percentage occurrence frequencies of sequence reads with TRAV, TRAJ, TRBV and TRBJ genes in total sequence reads were calculated.

Primer	Sequence
BSL-18E	AAAGCGGCCGCATGCTTTTTTTTTTTTTTTTTTVN
mCA-ST1-R	TCGTCGGCAGCGTCAGATGTGTATAAGAGACAGGTGGTACACAGCAGGTTCT
mCA1	TCATGTCCAGCACAGTTTTG
mCA2	GTTTTCGGCACATTGATTTG
mCB-ST1-R	TCGTCGGCAGCGTCAGATGTGTATAAGAGACAGGTTGGGTGGAGTCACATTT
mCB1	AGGATTGTGCCAGAAGGTAG
mCB2	TTGTAGGCCTGAGGGTCC
P10EA	GGGAATTCGG
P20EA	TAATACGACTCCGAATTCCC
P22EA-ST1-R	GTCTCGTGGGCTCGGAGATGTGTATAAGAGACAGCTAATACGACTCCGAATTCCC

3.16 Statistical Analysis

Cell culture assays have been performed in triplicates and in two independent experiments, unless stated otherwise. Data are expressed as mean ± SEM. Differences were analyzed by log-rank, two-tailed Student's t-test, Mann-Whitney U test, one-way ANOVA (using Bonferroni post test), one-sample t-test or χ^2-test using Prism 5 (GraphPad Software Inc., La Jolla, USA) or Excel (Microsoft, Redmond, USA), p-values ≤ 0.05 were considered significant.

4 Results

4.1 Loss of Stat3 in Intestinal Epithelial Cells Protects Mice from Tumorigenesis

In order to evaluate the role of Stat3 in the development of sporadic CRC, we made use of a chemically induced model of colon tumors. The mutagenic substance azoxymethane (AOM) is known to induce oncogenic point mutations in the gene encoding β-catenin and to trigger colonic tumorigenesis in mice (Greten et al., 2004; Schwitalla et al., 2013b; Tanaka et al., 2003) resembling the "classical pathway" of colon carcinogenesis (Fearon and Vogelstein, 1990). *Stat3*^{flox} and *Stat3*$^{\Delta IEC}$ were subjected to 6 weekly injections of AOM and tumor development was examined histologically 18 weeks later. While in Stat3-proficient (*Stat3*^{flox}) mice development of tubular adenomas in the distal colon was observed at 100% incidence, tumor development was completely abolished in *Stat3*$^{\Delta IEC}$ mice (Figure 4.1A-C). Surprisingly, no pre-neoplastic formations could be detected in AOM-treated *Stat3*$^{\Delta IEC}$ mice, which were detectable in *Stat3*$^{\Delta IEC}$ mice subjected to the AOM/DSS model of colitis-associated carcinogenesis (Bollrath et al., 2009). Interestingly, histological examination of colons of AOM challenged *Stat3*$^{\Delta IEC}$ mice revealed a marked accumulation of CD3$^+$ T cells within the colonic lamina propria of *Stat3*$^{\Delta IEC}$ mice when compared to tumor free areas of *Stat3*^{flox} controls (Figure 4.1D-F). At an early timepoint of the model, however, we detected AOM-induced aberrant crypt-foci, precursor lesions with distorted crypt architecture (Figure 4.1G), paralleled by an elevated number of CD11c$^+$ dendritic cells, but not F4/80$^+$ or Gr1$^+$ myeloid cells and increased *Il12* mRNA expression in the colon of *Stat3*$^{\Delta IEC}$ mice (Figure 4.1H, I),

suggesting T cell mediated loss of mutagenized Stat3-deficient cells during tumorigenesis.

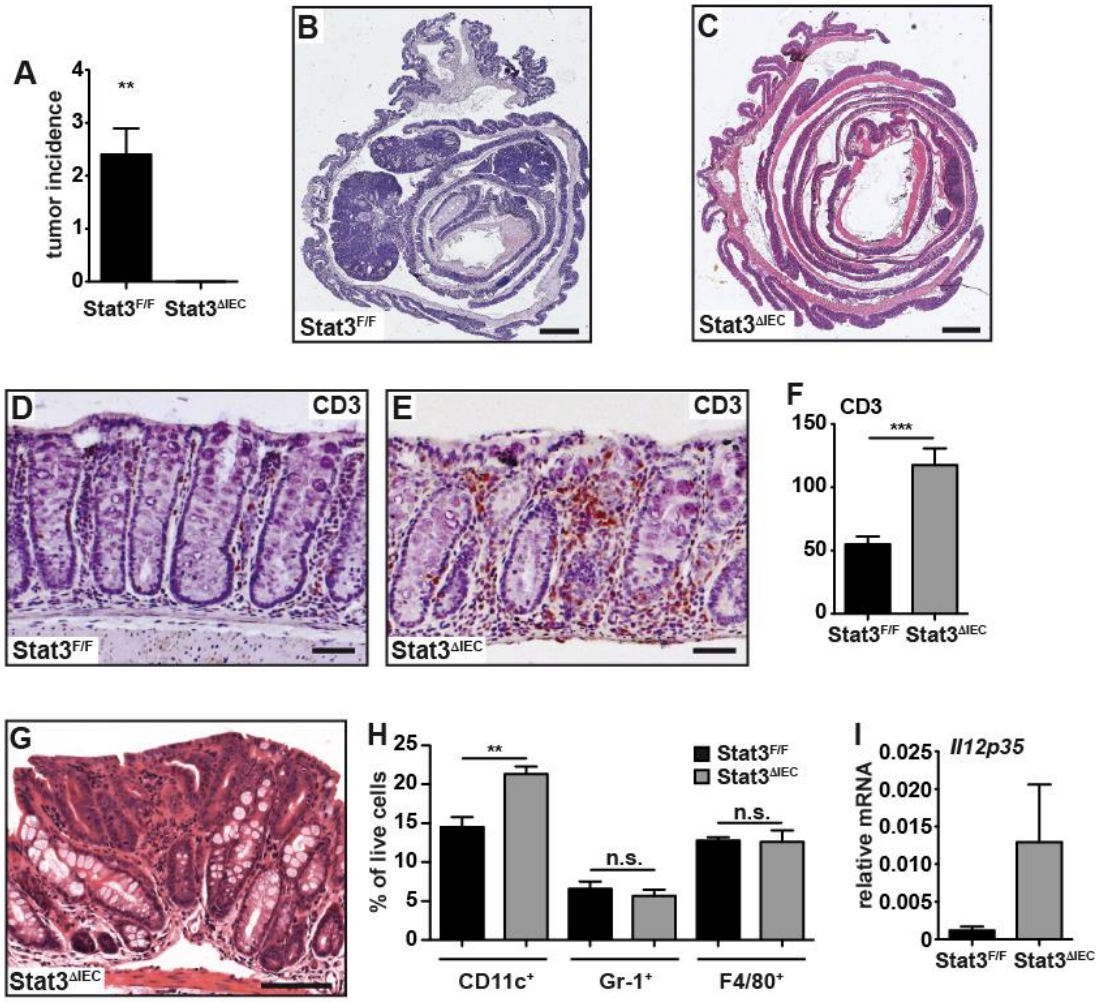

Figure 4.1: Loss of Stat3 in IEC Blocks Initiation of Sporadic Intestinal Tumorigenesis. (A) Tumor incidence in *Stat3*$^{F/F}$ and *Stat3*$^{\Delta IEC}$ mice 18 weeks after 6 weekly injections of AOM (n=10 or 9 per genotype, respectively, ** p<0.01 by one-sample t-test). **(B, C)** Representative H&E stained sections of AOM-challenged mice demonstrating absence of colonic tumors in *Stat3*$^{\Delta IEC}$ mice (C) in contrast to *Stat3*$^{F/F}$ littermate controls (B); scale bar = 1 mm. **(D, E)** Immunohistochemical staining of CD3 in colons of AOM-challenged mice 18 weeks after the last AOM injection; scale bar = 50 µm. **(F)** Quantification of infiltrating CD3$^+$ T cells in non-tumor areas as shown in (D) and (E); n = 3 mice per genotype, at least 10 high-power fields per mouse. **(G)** Representative depiction of aberrant crypt foci in the colon of Stat3$^{\Delta IEC}$ mice 8 weeks after the first AOM injection. H&E., scale bar = 100 µm. **(H)** Flow cytometric analysis of different myeloid cell subpopulations in colonic lamina propria of *Stat3*$^{F/F}$ and *Stat3*$^{\Delta IEC}$ mice one week after the last AOM injection (n=5 per genotype, ** p<0.01 by Student's t-test). **(I)** Relative mRNA expression of *Il12p35* in colonic mucosa of *Stat3*$^{F/F}$ and *Stat3*$^{\Delta IEC}$ mice one week after the last AOM injection (n=5 per genotype).

4.1.1 *Oncogene Activation in IEC Induces STAT3 Phosphorylation*

These results correspond with findings of Dr. Julia Bollrath (as outlined in section 1.7) and, therefore, we hypothesized that Stat3-deficient pre-neoplastic cells trigger an anti-tumor immune-response against mutagenized cells caused likewise by AOM-exposure or genetic recombination. In those experiments *villin-cre*ER^{T2}/*Ctnnb*$^{loxEx3/wt}$ mice, termed *β-cat*$^{c.a.}$, have been used, a mouse line with tamoxifen-inducible IEC-specific expression of a stabilized form of β-catenin. *β-cat*$^{c.a.}$ mice mimic the AOM-induced oncogenic mutations and aberrant activation of the Wnt/β-catenin pathway (Greten et al., 2004). They are characterized by rapid expansion of proliferative intestinal crypt stem cells and loss of absorptive enterocytes causing death of *β-cat*$^{c.a.}$ mice within approx. three weeks after oral tamoxifen application (Schwitalla et al., 2013a). Positive IHC-staining for both the serine 727- and tyrosine 705-phosphorylated form of Stat3 indicated marked STAT3 activation in transformed crypts of *β-cat*$^{c.a.}$ mice (Figure 4.2A-D).

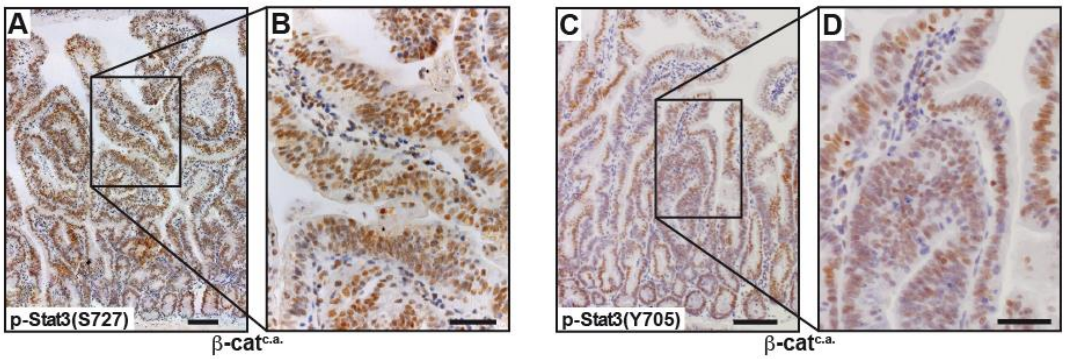

Figure 4.2: Activation of Wnt-Signaling in IEC Activates STAT3-Phosphorylation. (A-D) Immunohistochemical analysis of serine 727- (A, B) or tyrosine 705- (C, D) phosphorylated Stat3 in *β-cat*$^{c.a.}$ mice 15 days after the start of tamoxifen administration. Scale bar =100 µm (A, C) or 50 µm (B, D).

4.1.2 *Stat3-Deficient Tumorigenic IEC Trigger Adaptive Immunity*

IEC-restricted homozygous ablation of Stat3 significantly prolonged the survival of corresponding *β-cat*$^{c.a.}$/*Stat3*$^{\Delta IEC}$ mice dependent on the adaptive immune system as shown by Julia Bollrath (Figure 1.10-Figure 1.13). Confirming the activity of cytotoxic CD8^{+} T cells within the intestinal mucosa, increased apoptosis of *Stat3*-deficient IEC could be detected during the course of the model (Figure 4.3A). Furthermore, a higher villus/crypt ratio indicated a block in crypt expansion in mice compared to Stat3-proficient controls, while IEC-differentiation in *β-cat*$^{c.a.}$/*Stat3*$^{\Delta IEC}$ was indifferent to *β-cat*$^{c.a.}$ (Figure 4.3B-I).

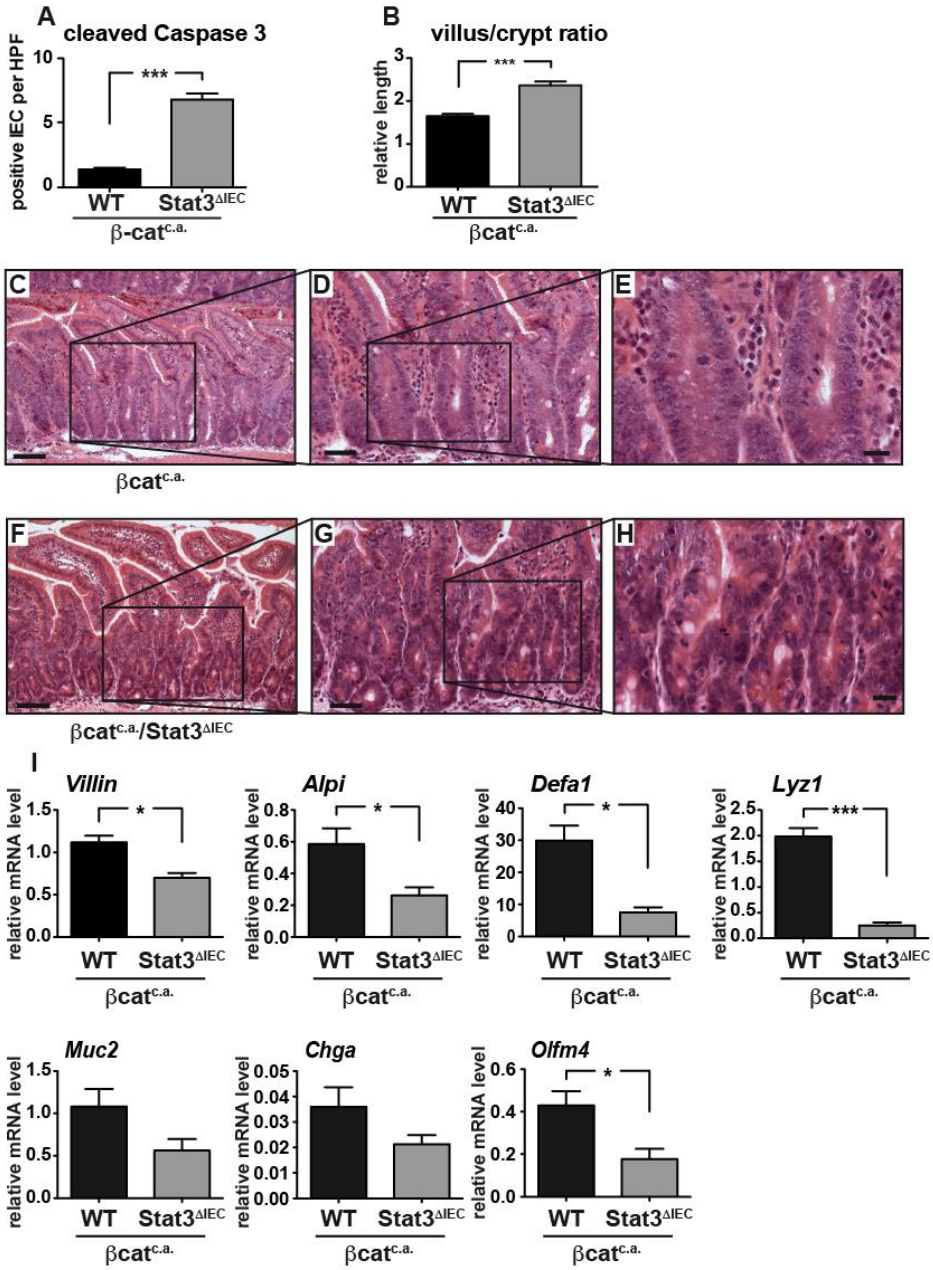

Figure 4.3: Transformed Stat3-Deficient IEC Show Increased Apoptosis. (A) Number of apoptotic cleaved caspase 3^{+} IEC in *β-cat*$^{c.a.}$ and *β-cat*$^{c.a.}$/*Stat3*$^{\Delta IEC}$ mice 15 days after the start of tamoxifen administration (n=4/genotype; ≥20 high power fields (HPF)/animal; *** p< 0.001 by Student's t-test). **(B)** Villus length relative to average crypt length per mouse in the small intestine of *β-cat*$^{c.a.}$ and *β-cat*$^{c.a}$/Stat3$^{\Delta IEC}$ mice 15 days after the start of tamoxifen administration (n=3 or 5 mice, respectively, *** p<0.001 by Student's t-test). **(C-H)** H&E staining of the small intestine of *β-cat*$^{c.a.}$ (C-E) and *β-cat*$^{c.a}$/Stat3$^{\Delta IEC}$ (F-H) mice 15 days after the start of tamoxifen administration. Scale bar = 100 µm (C, F), 50 µm (D, G) or 20 µm (E, H). **(I)** Relative mRNA expression of the indicated genes in IEC of *β-cat*$^{c.a.}$ and *β-cat*$^{c.a.}$/*Stat3*$^{\Delta IEC}$ mice 15 days after the start of tamoxifen administration (n=3 mice per genotype).

Real-Time PCR confirmed elevated *Ifng* expression in the mucosa of *β-cat*$^{c.a.}$/*Stat3*$^{\Delta IEC}$ mice when compared to their Stat3 proficient counterparts (Figure

4.4A). These findings were further corroborated by FACS analysis, which revealed a marked increase of $CD3^+$ T cells in the lamina propria of *β-cat*$^{c.a.}$/*Stat3*$^{\Delta IEC}$ mice and $CD8^+$ cells as the main source of IFNγ (Figure 4.4B-D). Moreover, *β-cat*$^{c.a.}$/*Stat3*$^{\Delta IEC}$ mice showed an elevated frequency of $CD11b^+F4/80^+$ macrophages (Figure 4.4E) and activated $CD11b^+/CD11c^+$ dendritic cells (DC) that expressed CD80 and IL-12 (Figure 4.4F-H). In addition, at an earlier timepoint of the model we could detect elevated expression of MHC class I in $EpCAM^+$ IEC (Figure 4.4I), suggesting increased antigen-expression of Stat3-deficient IEC as a potential trigger of $CD8^+$ T cell activation. In contrast, other notable immune cell populations were unchanged (Figure 4.4J-L).

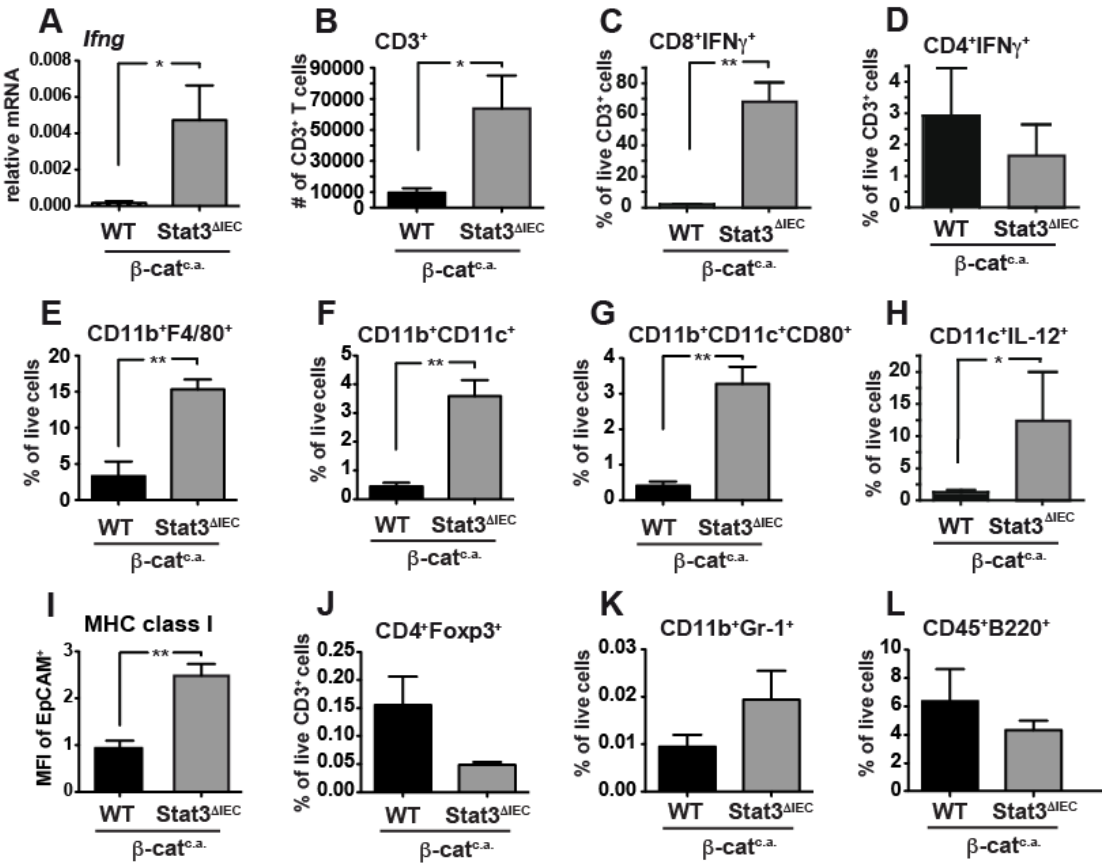

Figure 4.4: Activation of Wnt-Signaling in Stat3-Deficient IEC Triggers Antigen-Presentation and Adaptive Immunity. (A) Relative *Ifng* mRNA expression in small intestinal mucosa of *β-cat*$^{c.a.}$ and *β-cat*$^{c.a.}$/*Stat3*$^{\Delta IEC}$ mice 15 days after the start of tamoxifen administration; n=6/genotype, * $p<0.05$ by Student's t-test. **(B)** Quantification of infiltrating $CD3^+$ T cells in small intestinal lamina propria of *β-cat*$^{c.a.}$ and *β-cat*$^{c.a.}$/*Stat3*$^{\Delta IEC}$ mice 15 days after the start of tamoxifen administration. **(C-H)** Flow cytometric analysis of IFNγ in $CD8^+$ and $CD4^+$ T cells, $CD11b^+F4/80^+$ cells as well as IL-12 and CD80 in $CD11c^+$ cells in small intestinal lamina propria of *β-cat*$^{c.a.}$ and *β-cat*$^{c.a.}$/*Stat3*$^{\Delta IEC}$ mice 15 days after the start of tamoxifen administration (n=3/genotype; * $p<0.05$; ** $p< 0.01$). **(I)** Mean fluorescence intensity (MFI) representing surface expression of MHC class I as assed by flow cytometry 3 days after the start of tamoxifen administration (n=4 mice each, ** $p<0.01$ by Student's t-test). **(J-L)** Flow cytometric analysis of $CD4^+Foxp3^+$ (N), $CD11b^+Gr1^+$ (O) $CD45^+B220^+$ cells in small intestinal lamina propria of *β-cat*$^{c.a.}$ and *β-cat*$^{c.a.}$/*Stat3*$^{\Delta IEC}$ mice 15 days after the start of tamoxifen administration (n=3/genotype).

Furthermore, a number of T cell related chemokines, most notably the IFNγ-inducible chemokines CXCL-9, CXCL-10 and CXCL-11, were found to be upregulated in Stat3-deficient IEC during tumorigenesis (Figure 4.5). Collectively, these data suggest that loss of Stat3 in IEC triggered an adaptive immune response promoting IEC death, which delayed expansion of β-catenin mutant crypt cells associated with prolonged survival of *β-cat*$^{c.a.}$ /*Stat3*$^{\Delta IEC}$ mice.

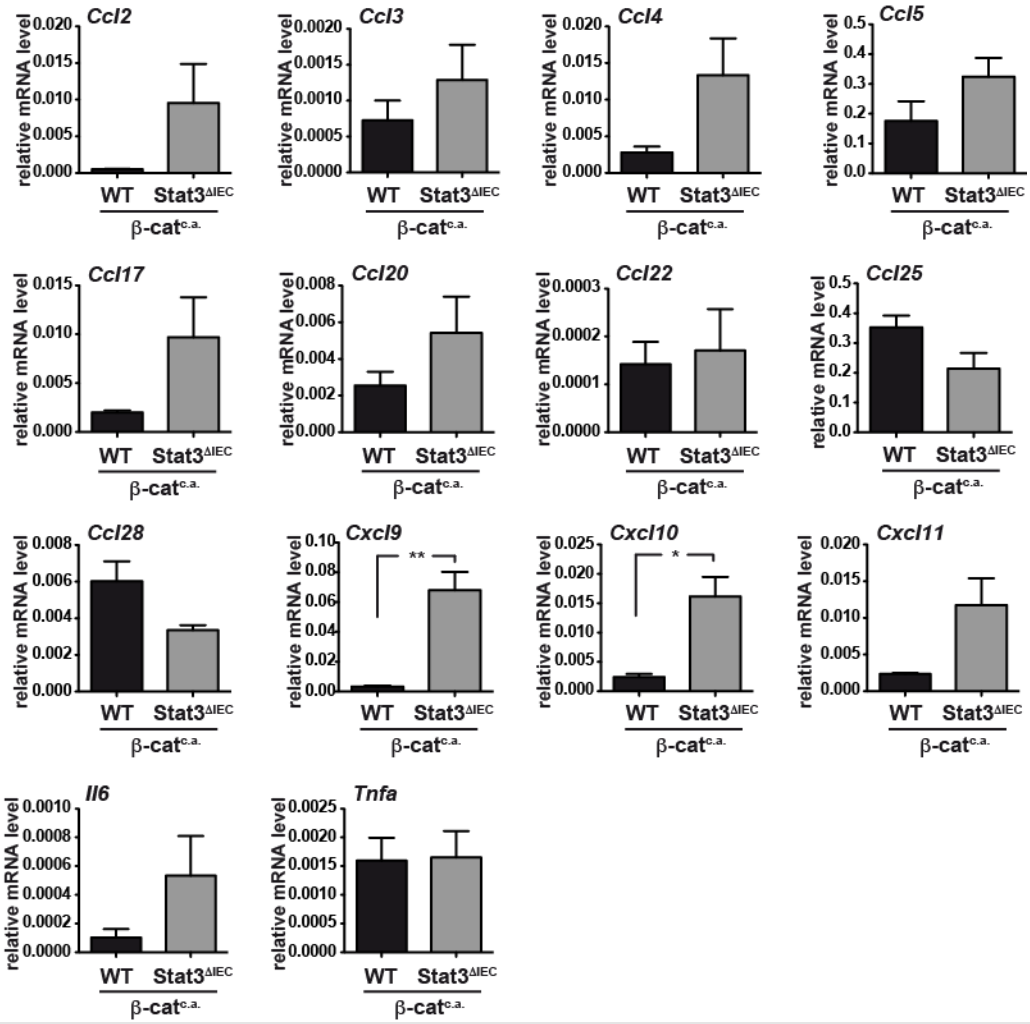

Figure 4.5: **IEC of *β-cat*$^{c.a.}$ /*Stat3*$^{\Delta IEC}$ Mice Show Increased Chemokine-Expression.** Relative gene expression of the indicated cytokines or chemokines in IEC of *β-cat*$^{c.a.}$ and *β-cat*$^{c.a.}$ /*Stat3*$^{\Delta IEC}$ mice 15 days after the start of tamoxifen administration (n=3/genotype, * $p < 0.05$, ** $p < 0.01$ by Student's t-test).

4.1.3 *Increased T Cell Clonality in Intestines of β-cat*$^{c.a.}$ */Stat3*$^{\Delta IEC}$ *Mice*

T cells (as well as B-cells) activated by antigen-contact and co-stimulation and cytokine-signaling proliferate and give rise to a pool of daughter cells that share the same rearranged TCR gene loci and, therefore, show the same reactivity towards antigens. This feature of the adaptive immune system is called clonal expansion and is required for a proper immune reaction. We aimed to confirm the activation of an adaptive immune response in *β-cat*$^{c.a.}$ and *β-cat*$^{c.a.}$ /*Stat3*$^{\Delta IEC}$ mice. Therefore, we purified $CD8^+$ T cells from the intestinal mucosa by FACS sorting and analyzed the

clonality of T cells by sequencing of the TCRα- and β-chain CDR3 regions. In line with an enhanced antigen-dependent immune response in these mice, we could observe clonal expansion of $CD8^+$ T cells and a less diverse T cell receptor repertoire (Figure 4.6A-K) in *β-cat*$^{c.a.}$/*Stat3*$^{\Delta IEC}$ mice compared to Stat3-proficient controls.

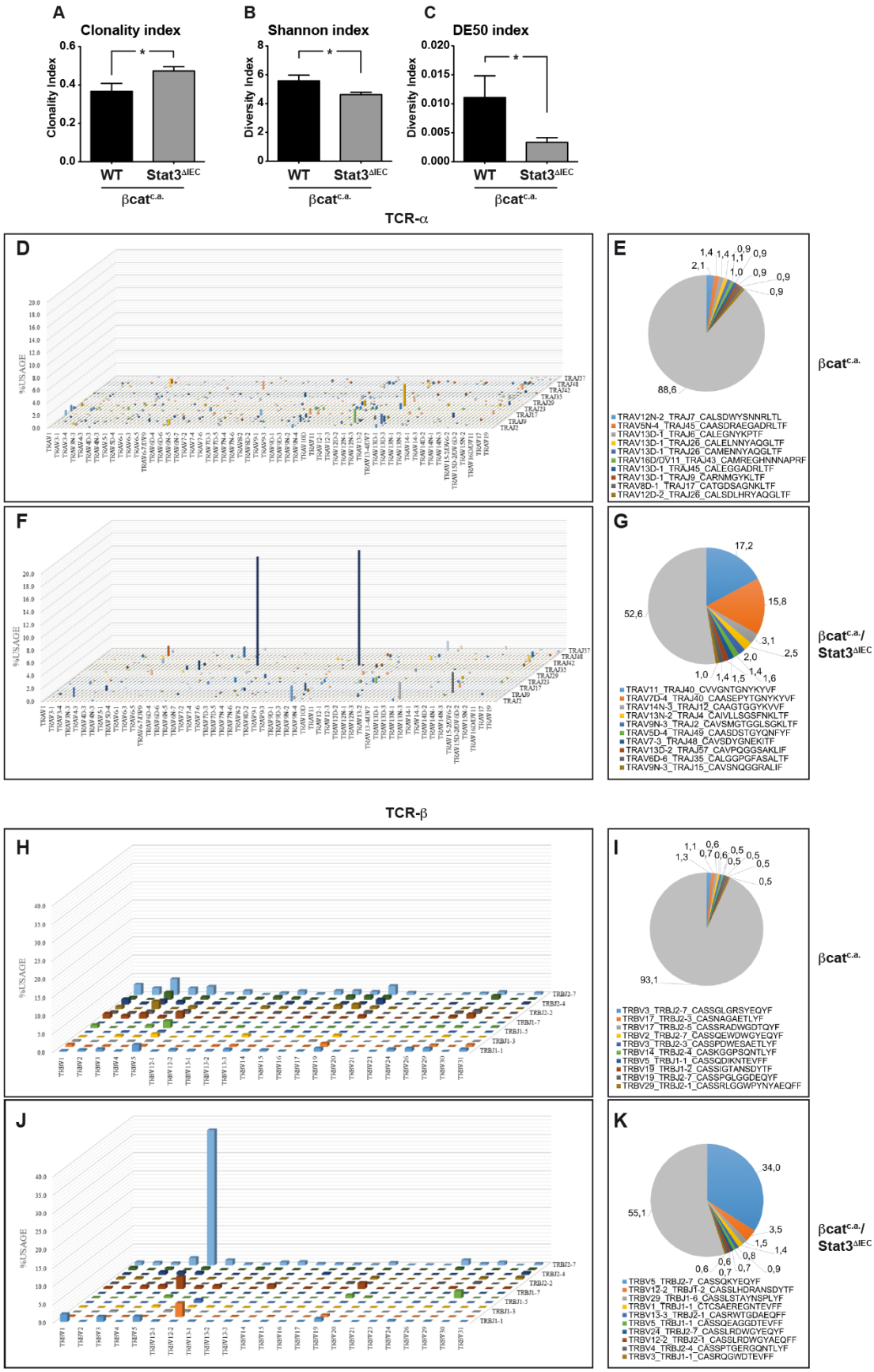
A
Clonality index
Clonality Index
0.6
0.4
0.2
0.0
*
WT
Stat3ΔIEC
βcatc.a.
B
Shannon index
Diversity Index
8
6
4
2
0
*
WT
Stat3ΔIEC
βcatc.a.
C
DE50 index
Diversity Index
0.020
0.015
0.010
0.005
0.000
*
WT
Stat3ΔIEC
βcatc.a.
TCR-α
D
%USAGE
E
1,4 1,4 1,1 0,9 0,9
2,1
1,0 0,9 0,9
0,9
88,6
TRAV12N-2_TRAJ7_CALSDWYSNNRLTL
TRAV5N-4_TRAJ45_CAASDRAEGADRLTF
TRAV13D-1_TRAJ6_CALEGNYKPTF
TRAV13D-1_TRAJ26_CALELNNYAQGLTF
TRAV13D-1_TRAJ26_CAMENNYAQGLTF
TRAV16D/DV11_TRAJ43_CAMREGHNNNAPRF
TRAV13D-1_TRAJ45_CALEGGADRLTF
TRAV13D-1_TRAJ9_CARNMGYKLTF
TRAV8D-1_TRAJ17_CATGDSAGNKLTF
TRAV12D-2_TRAJ26_CALSDLHRYAQGLTF
βcatc.a.
F
%USAGE
G
17,2
15,8
52,6
3,1
2,5
2,0
1,0 1,4 1,5 1,4 1,6
TRAV11_TRAJ40_CVVGNTGNYKYVF
TRAV7D-4_TRAJ40_CAASEPYTGNYKYVF
TRAV14N-3_TRAJ12_CAAGTGGYKVVF
TRAV13N-2_TRAJ4_CAIVLLSGSFNKLTF
TRAV9N-3_TRAJ2_CAVSMGTGGLSGKLTF
TRAV5D-4_TRAJ49_CAASDSTGYQNFYF
TRAV7-3_TRAJ48_CAVSDYGNEKITF
TRAV13D-2_TRAJ57_CAVPQGGSAKLIF
TRAV6D-6_TRAJ35_CALGQPQFASALTF
TRAV9N-3_TRAJ15_CAVSNQGGRALIF
βcatc.a./
Stat3ΔIEC
TCR-β
H
%USAGE
I
1,1 0,6
1,3 0,7 0,6 0,5 0,5 0,5
0,5
93,1
TRBV3_TRBJ2-7_CASSGLGRSYEQYF
TRBV17_TRBJ2-3_CASNAGAETLYF
TRBV17_TRBJ2-5_CASSRADWGDTQYF
TRBV2_TRBJ2-7_CASSQEWDWGYEQYF
TRBV3_TRBJ2-3_CASSPDWESAETLYF
TRBV14_TRBJ2-4_CASKGGPSQNTLYF
TRBV5_TRBJ1-1_CASSQDIKNTEVFF
TRBV19_TRBJ1-2_CASSIGTANSDYTF
TRBV19_TRBJ2-7_CASSPGLGGDEQYF
TRBV29_TRBJ2-1_CASSRLGGWPYNYAEQFF
βcatc.a.
J
%USAGE
K
34,0
55,1
3,5
1,5
1,4
0,8
0,6 0,6 0,7 0,9
0,7
TRBV5_TRBJ2-7_CASSQKYEQYF
TRBV12-2_TRBJ1-2_CASSLHDRANSDYTF
TRBV29_TRBJ1-6_CASSLSTAYNSPLYF
TRBV1_TRBJ1-1_CTCSAEREGNTEVFF
TRBV13-3_TRBJ2-1_CASRWTGDAEQFF
TRBV5_TRBJ1-1_CASSQEAGGDTEVFF
TRBV24_TRBJ2-7_CASSLRDWGYEQYF
TRBV12-2_TRBJ2-1_CASSLRDWGYAEQFF
TRBV4_TRBJ2-4_CASSPTGERGQNTLYF
TRBV3_TRBJ1-1_CASRGGWDTEVFF
βcatc.a./
Stat3ΔIEC

Figure 4.6: Clonal Expansion of Intestinal CD8$^+$ T Cells in β-cat$^{c.a.}$/Stat3$^{\Delta IEC}$ Mice as Shown by TCR Repertoire Analysis. (A-C) Statistical analysis for clonality (A) and diversity of T cell receptor (TCRα and TCRβ) repertoire (B, C) in sorted mucosal CD8$^+$ T cells from *β-cat*$^{c.a.}$ and *β-cat*$^{c.a.}$/*Stat3*$^{\Delta IEC}$ mice 15 days after the start of tamoxifen administration (n = 3 and 4, respectively, * $p < 0,05$ by Mann-Whitney U-test). **(D-K)** Relative abundance of productive unique TCR-α (D-G) and TCR-β (H-K) chain sequences (D, F, H, J) from sorted intestinal CD8$^+$ T cells and the relative contribution of the ten most abundant sequences (E, G, I, K) from one representative *β-cat*$^{c.a.}$ (D, E, H, I) or *β-cat*$^{c.a.}$/*Stat3*$^{\Delta IEC}$ mouse (F, G, J, K) each 15 days after the start of tamoxifen administration (of 3 or 4 mice analyzed, respectively).

Interestingly, within our experimental group of 4 mice the T cell repertoire was unique in each individual animal ((Figure 4.7A). Analysis of the distribution pattern of clones in various animals revealed that most clones detected in each mouse cannot be detected in other mice and only a limited number of clones are being detected in more than one mouse, typically with low copy number. E.g., the only clone detected in all 4 mice examined (TRAJ15-derived, sequence CAVSGQGGRALI) was present with relative abundance of < 0.01 % of in-frame reads in each mouse.

This high degree of interindividual heterogeneity was confirmed by flow cytometric profiling of TCR Vβ in CD8$^+$ T cells isolated from the intestines of wildtype, *β-cat*$^{c.a.}$ and *β-cat*$^{c.a.}$ /*Stat3*$^{\Delta IEC}$ mice, showing a unique profile in each mouse analyzed (Figure 4.7B). These findings support the hypothesis that hyperproliferating Stat3-deficient IEC activate T cells by increased surface-display of antigenic peptides, however, the particular antigen(s) responsible for T cell expansion seem to be different in each mouse.

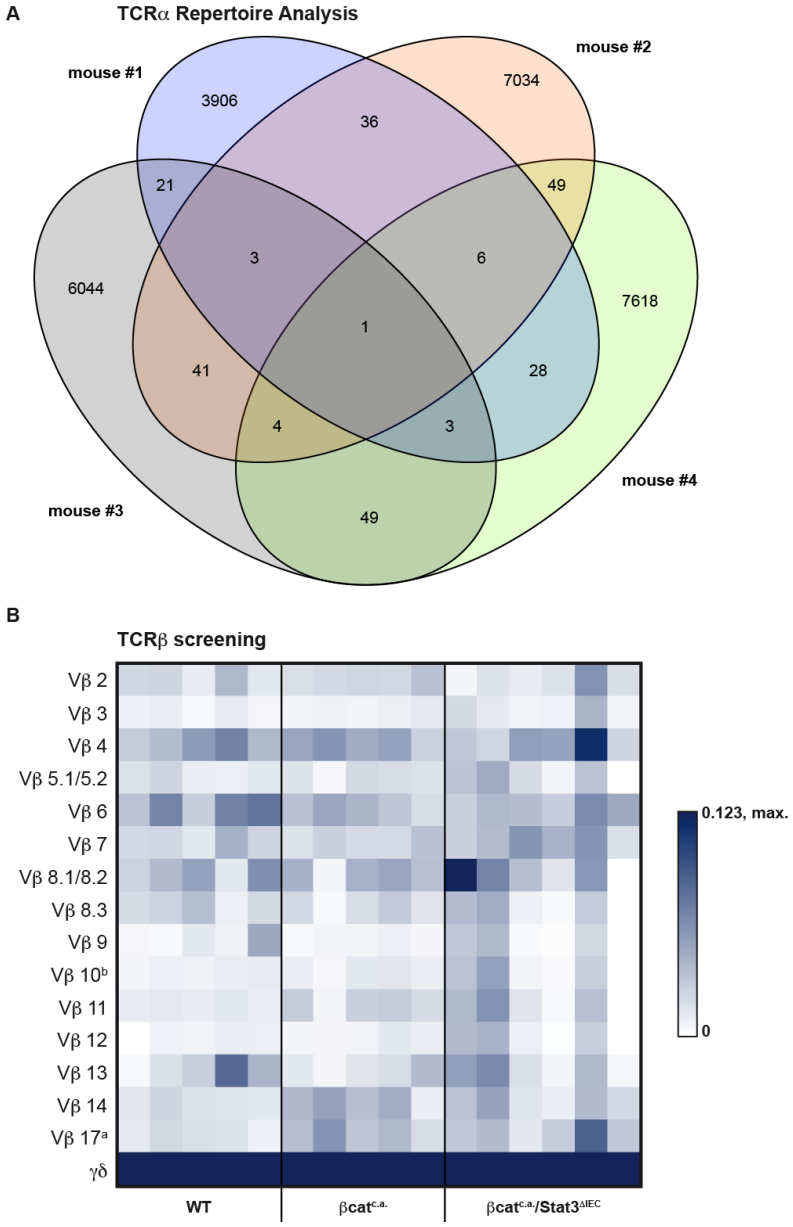

Figure 4.7: High Interindividual Variability in Intestinal T Cell Clones in *β-cat*$^{c.a.}$ /*Stat3*$^{\Delta IEC}$ mice. **(A)** Venn diagram depicting number of T cell clones detected in the intestine of one or more *β-cat*$^{c.a.}$ /*Stat3*$^{\Delta IEC}$ mice by TCR sequencing. A total number of 24843 unique TCR clones have been detected in at least one of the four mice depicted. **(B)** Heatmap depiction of relative abundance of $CD3^+CD8^+$ cells staining with the indicated TCR specific antibody as assessed by flow cytometry. Cells were isolated from the small intestine of wildtype (n=5), *β-cat*$^{c.a.}$ (n=5) and *β-cat*$^{c.a.}$ /*Stat3*$^{\Delta IEC}$ (n=6) mice 15 days after the start of tamoxifen administration. Note that values exceeding the indicated maximum value, denominating the highest value in non γδTCR lines, are depicted in same color as the maximum value.

4.1.4 *Expansion of Antigen-Specific T Cells in β-cat$^{c.a.}$/Stat3$^{\Delta IEC}$ Mice by Enhanced Antigen-Presentation*

Next, we tested the reactivity of T cells towards a defined neoantigen expressed in Stat3-deficient or -proficient hyperproliferating IEC. Therefore, we made use of the mouse line ROSAOVA expressing an ovalbumin-derived immunogenic peptide (OVAaa 246–353) upon Cre-mediated recombination. We bred those mice with both *β-cat*$^{c.a.}$ mice (*β-cat*$^{c.a.}$/*OVA*^{IEC}) as well as *β-cat*$^{c.a.}$/*Stat3*$^{\Delta IEC}$ mice (*β-cat*$^{c.a.}$/*Stat3*$^{\Delta IEC}$/*OVA*^{IEC}) and resulting offspring were treated with tamoxifen. We analyzed expansion of antigen-specific T cells by flow cytometry using the K^{b}/OVA (SIINFEKL) pentamer. Expectedly, we could detect a significantly increased number of SIINFEKL specific CD8^{+} T cells in the intestinal mucosa in *β-cat*$^{c.a.}$/*Stat3*$^{\Delta IEC}$/*OVA*^{IEC} mice (Figure 4.8A). In line with the increased expansion of antigen-specific T cells observed, staining of IEC using the 25-D1.16 monoclonal antibody that specifically reacts with ovalbumin-derived peptide SIINFEKL bound to H-2K^{b} of MHC class I, revealed increased binding on Stat3-deficient IEC, confirming enhanced antigen processing in IEC from *β-cat*$^{c.a.}$/*Stat3*$^{\Delta IEC}$/*OVA*^{IEC} mice (Figure 4.8B).

Similarly, the number of SIINFEKL specific CD8^{+} T cells was elevated in AOM-challenged *Stat3*$^{\Delta IEC}$/*OVA*^{IEC} mice when compared to *OVA*^{IEC} mice (Figure 4.8C). Collectively, these data strongly suggest that IEC-specific Stat3 activation precludes the generation of an effective CD8^{+} T cell-dependent immune response during the tumor initiation phase.

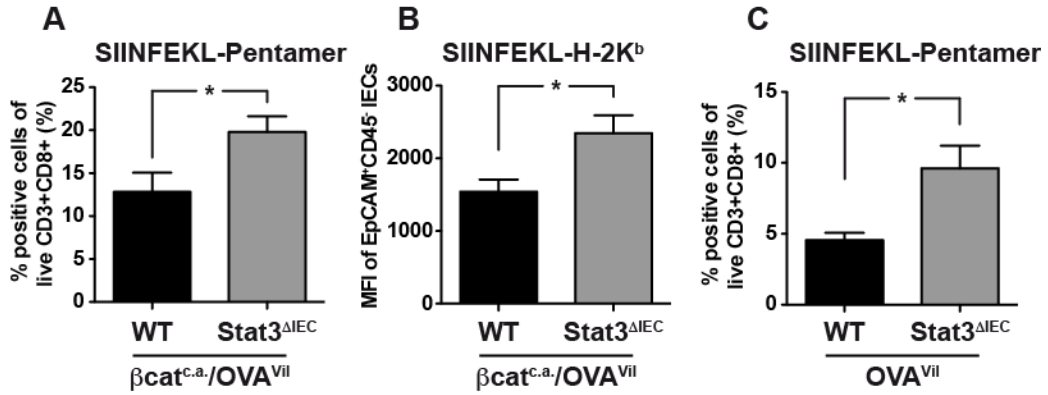

Figure 4.8: Elevated Activation of Antigen-Specific T Cells by Stat3-Deficiency in Early Tumorigenesis. (A) Flow cytometric quantification of SIINFEKL-MHC pentamer binding $CD3^+CD8^+$ T cells in the intestines of *β-cat*$^{c.a.}$/*OVA*^{IEC} or *β-cat*$^{c.a.}$/*Stat3*$^{\Delta IEC}$/*OVA*^{IEC} mice 15 days after the start of tamoxifen administration (n=5 mice each, * $p<0.05$ by Student's t-test). **(B)** Mean fluorescence intensity (MFI) representing surface expression of SIINFEKL-binding MHC class I as assessed by flow cytometry 15 days after the start of tamoxifen administration (n=5 mice each, * $p<0.05$ by Student's t-test). **(C)** Flow cytometric quantification of SIINFEKL-MHC pentamer binding $CD3^+CD8^+$ T cells in the colon of AOM-treated *OVA*^{IEC}- or *OVA*^{IEC}/*Stat3*$^{\Delta IEC}$ mice 18 weeks after the first AOM injection. Mice have been fed continuously with tamoxifen-containing chow starting 14 weeks after the first AOM injection (n=4 or 6 mice, respectively, * $p<0.05$ by Student's t-test).

4.2 Immune Activation is a Consequence of Lysosomal Membrane Permeabilization

Having evaluated the consequence of Stat3 deletion in epithelial cells during early stages of tumorigenesis we next aimed to identify the responsible mechanism that triggered the activation of enhanced antigen presentation and activation of the adaptive immune system. A previous study using murine colon cancer cells or B16 melanoma cells expressing a dominant negative Stat3 mutant found increased expression of pro-inflammatory cytokines including TNFα, IL-6, CCL5, CXCL10 and IFNβ which triggered $CD8^+$ T cell activation (Wang et al., 2004). We tested the contribution of these cytokines in our model system and, surprisingly, we did not observe marked expression differences for these cytokines and chemokines between primary IEC of Stat3 wildtype *β-cat*$^{c.a.}$ and Stat3-deficient *β-cat*$^{c.a.}$/*Stat3*$^{\Delta IEC}$ mice 3 days after the first tamoxifen application (Figure 4.9).

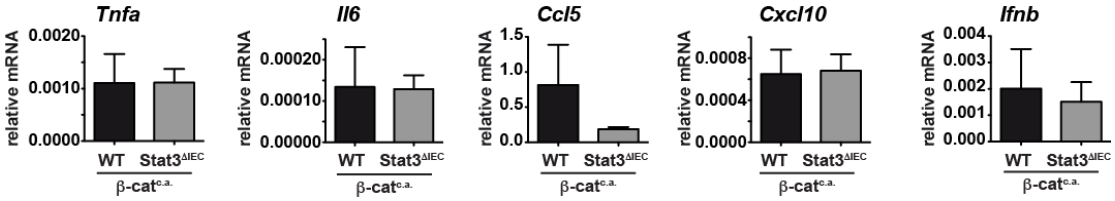

Figure 4.9: Indifferent Expression of Selected Cytokines in Stat3-Proficient or -Deficient IEC. Relative mRNA expression of *Tnfa, Il6, Ccl5, Cxcl10 and Ifnb* in small intestinal mucosa of *β-cat*$^{c.a.}$ and *β-cat*$^{c.a.}$/*Stat3*$^{\Delta IEC}$ mice 15 days after the start of tamoxifen administration (n=5 mice per genotype).

However, histomorphological evaluation revealed markedly enlarged lysosomal structures in the apical segment of the epithelial layer of *β-cat*$^{c.a.}$/*Stat3*$^{\Delta IEC}$ mice when stained for the lysosomal membrane protein LAMP2 (Figure 4.10A, B), which prompted us to examine lysosomal function. Lysosomes are membrane-enclosed organelles rich in proteases such as cathepsins. We evaluated total expression of cathepsins S, L and B as well as of the lysosomal protease inhibitor cystatin C and found its level to be indifferent in IEC of *β-cat*$^{c.a.}$/*Stat3*$^{\Delta IEC}$ or *β-cat*$^{c.a.}$ control mice (Figure 4.10C, D). However, we observed an increased localization of cathepsins S and B in the cytoplasm of purified Stat3-deficient IEC presumably as a result of increased release from lysosomes due to increased lysosomal membrane permeabilization (LMP; Figure 4.10E-G). In order to evaluate the functional consequence of lysosomal protease activity during tumorigenesis, we administered the pan-cysteine protease inhibitor E64d to *β-cat*$^{c.a.}$ and *β-cat*$^{c.a.}$/*Stat3*$^{\Delta IEC}$ mice. We observed that E64d prevented upregulation of *Ifng* gene expression in the intestinal mucosa of both Stat3-deficient and -proficient *β-cat*$^{c.a.}$ mice as well as IEC apoptosis, thus demonstrating the importance of lysosomal proteases for $CD8^+$ T cell activation (Figure 4.10H, I).

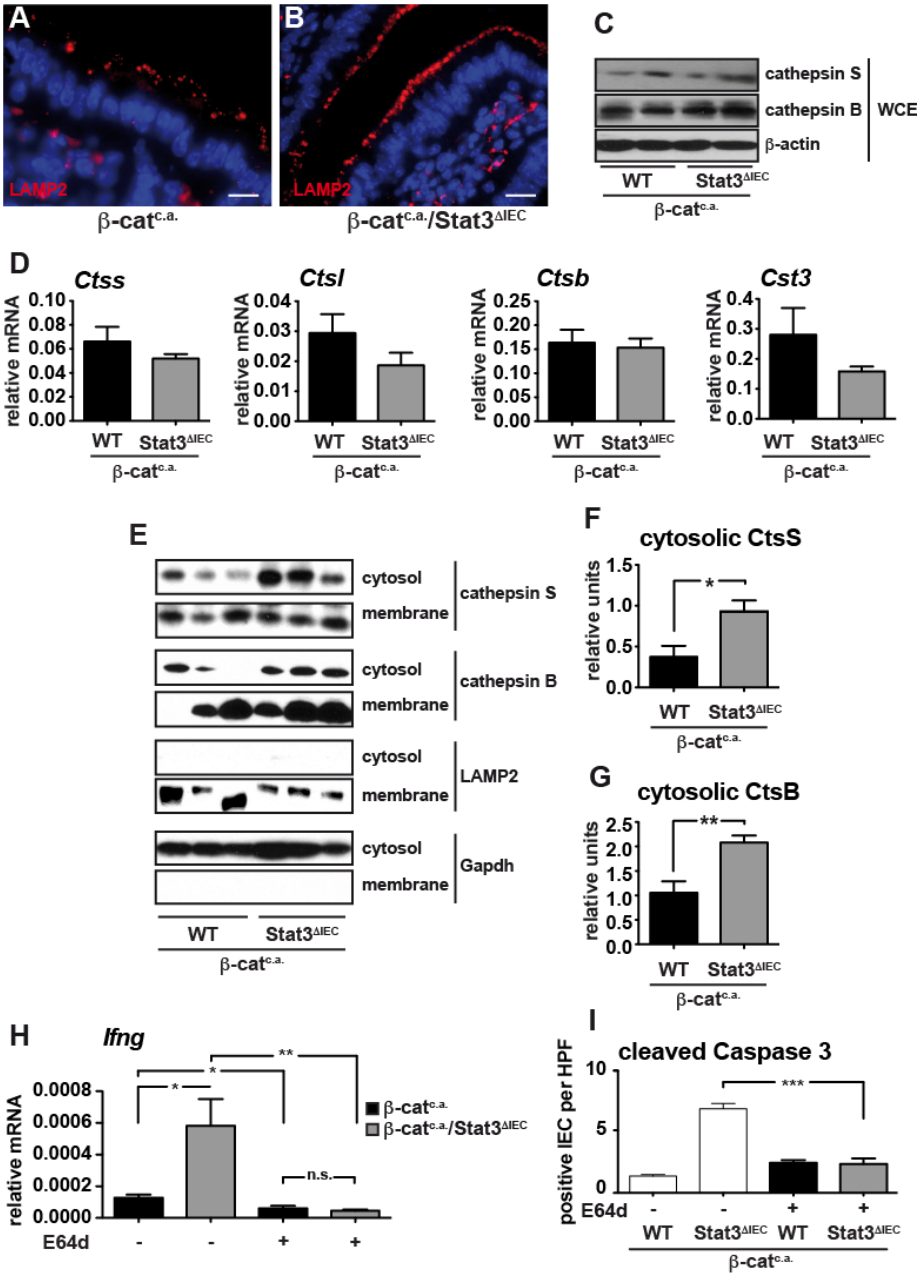
A
LAMP2
β-cat c.a.
B
LAMP2
β-cat c.a./Stat3 ΔIEC
C
cathepsin S
cathepsin B
β-actin
WCE
WT
Stat3 ΔIEC
β-cat c.a.
D
Ctss
Ctsl
Ctsb
Cst3
relative mRNA
WT
Stat3 ΔIEC
β-cat c.a.
E
cytosol
membrane
cathepsin S
cathepsin B
LAMP2
Gapdh
WT
Stat3 ΔIEC
β-cat c.a.
F
cytosolic CtsS
relative units
G
cytosolic CtsB
relative units
H
Ifng
relative mRNA
β-cat c.a.
β-cat c.a./Stat3 ΔIEC
n.s.
E64d
I
cleaved Caspase 3
positive IEC per HPF
E64d

Figure 4.10: Stat3-Deficiency During Tumorigenesis Triggers Lysosomal Dysfunction. (A, B) Immunofluorescence LAMP2 staining visualizing lysosomes in the mucosa of *β-cat*$^{c.a.}$ and *β-cat*$^{c.a.}$/*Stat3*$^{\Delta IEC}$ mice 3 days after the start of tamoxifen administration. scale bar = 5 µm. **(C)** Immunoblot analysis of cathepsin S and cathepsin B in whole cell extracts (WCE) of small intestinal IEC of *β-cat*$^{c.a.}$ and *β-cat*$^{c.a.}$/*Stat3*$^{\Delta IEC}$ mice 15 days after the start of tamoxifen administration. **(D)** Relative mRNA expression of *Ctss*, *Ctsl*, *Ctsb* and *Cst3* (encoding the cysteine protease inhibitor Cystatin C) in isolated small intestinal IEC of *β-cat*$^{c.a.}$ and *β-cat*$^{c.a.}$/*Stat3*$^{\Delta IEC}$ mice 15 days after the start of tamoxifen administration. (n=6 mice each, p>0.05 by Student's t-test). **(E-G)** Immunoblot analysis of cathepsin S, cathepsin B, LAMP2 and Gapdh in cytosolic and membrane fractions isolated from small intestinal IEC of *β-cat*$^{c.a.}$ and *β-cat*$^{c.a.}$/*Stat3*$^{\Delta IEC}$ mice 3 days after the start of tamoxifen administration (E), and densitometric quantification of cytosolic cathepsin S (F) and B (G) normalized to Gapdh (n≥6, * p<0.05, ** p<0.01 by Student's t-test). **(H)** Relative amount of *Ifng*-mRNA in the small intestinal whole mucosa of *β-cat*$^{c.a.}$ and *β-cat*$^{c.a.}$/*Stat3*$^{\Delta IEC}$ mice 15 days after the start of tamoxifen administration treated with the cyteine protease inhibitor E64d at 5 mg/kg bodyweight or control (n≥5, * p<0.05, ** p<0.01 by Student's t-test). **(I)** Quantification of cleaved caspase-3 positive IEC in the small intestine of E64d-treated or control *β-cat*$^{c.a.}$ or *β-cat*$^{c.a.}$/*Stat3*$^{\Delta IEC}$ mice 15 days after the start of tamoxifen administration (n=4/group, ≥20 400X-high-power fields (HPF) have been counted per animal, *** p<0.001 by Student's t-test). Please note that parts of the figure have been reproduced from Figure 4.3A for better visibility.

4.2.1 *T Cell Activation by a Stat3-Independent LMP-Trigger*

To test the hypothesis that LMP could trigger CD8$^+$ T cell activation we utilized the lysosomotropic agent chloroquine, a small 320 Da molecule with a pK_a of approx. 8.1 and well-known inducer of LMP (Boya et al., 2003; de Duve et al., 1974). Treatment of *β-cat*$^{c.a.}$ mice with chloroquine triggered the release of cathepsins from lysosomes in β-catenin mutant IEC (Figure 4.11A) and caused accumulation of CD3$^+$ T cells in the lamina propria of *β-cat*$^{c.a.}$ mice (Figure 4.11B, C) as well as upregulation of *Ifng* mRNA (Figure 4.11D). In addition, chloroquine-treatment increased the number of cleaved caspase-3$^+$ apoptotic IEC in *β-cat*$^{c.a.}$ mice (Figure 4.11E) in line with cytotoxic T cell activation. Moreover, chloroquine prevented expansion of β-catenin mutant crypts and death of *β-cat*$^{c.a.}$ mice in a CD8$^+$ T cell dependent manner (Figure 4.11F-I). In agreement with this notion, we could observe an increased number of SIINFEKL specific CD8$^+$ T cells in the intestinal mucosa of AOM-challenged *OVA*^{IEC} mice (Figure 4.11J). Consequently, chloroquine-treatment over a period of 4 weeks reduced tumor load of established AOM-induced adenomas in WT

mice (Figure 4.11K), strongly supporting the stimulation of an anti-tumor immune response upon LMP induction.

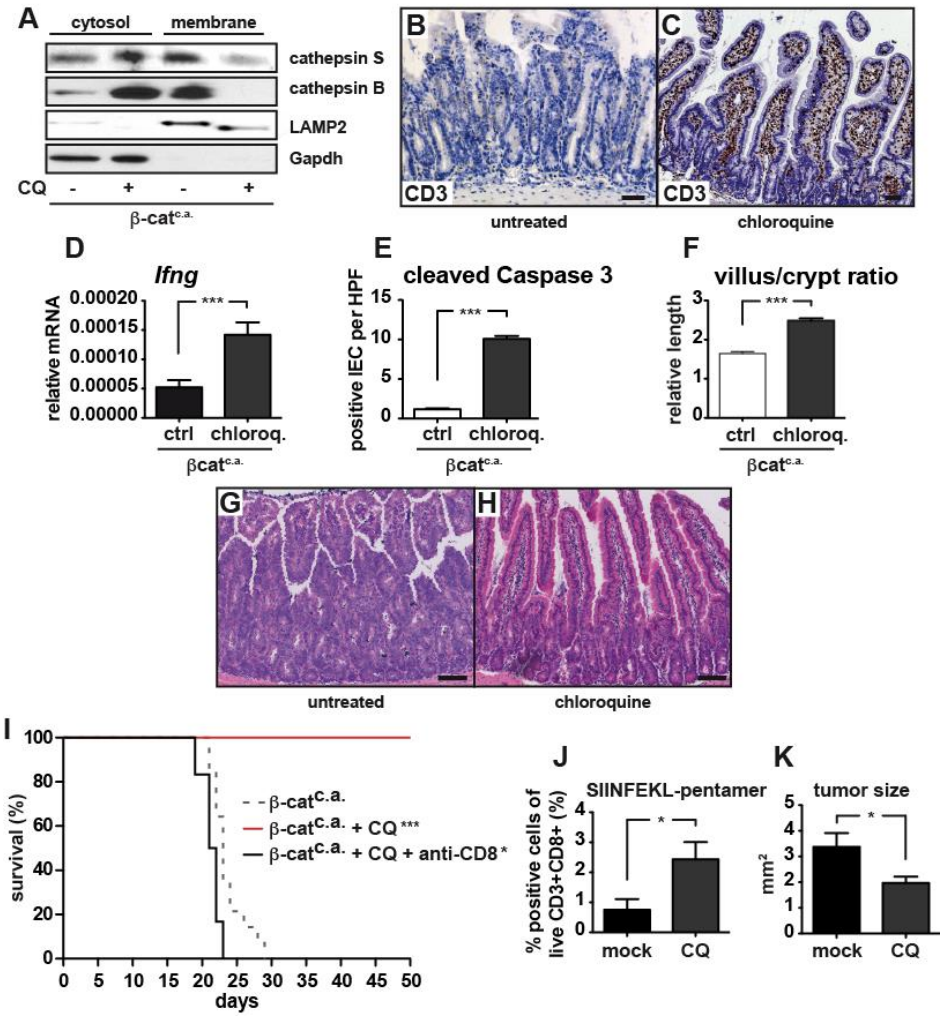

Figure 4.11: Induction of LMP Triggers Adaptive Immunity During Tumorigenesis. (A) Immunoblot analysis of cathepsin S, cathepsin B, Lamp2 and Gapdh in IEC isolated 3 days after the start of tamoxifen administration from untreated or chloroquine (60 mg/kg) treated *β-cat*$^{c.a.}$ mice. **(B, C)** Immunohistochemical analysis reveals marked accumulation of $CD3^+$ T cells in small intestinal mucosa of chloroquine treated *β-cat*$^{c.a.}$ mice (C) as compared to untreated controls (B) 15 days after the start of tamoxifen administration. Scale bar = 50 µm. **(D)** Relative amount of *Ifng*-mRNA in the small intestine of *β-cat*$^{c.a.}$ mice 15 days after the start of tamoxifen administration treated with chloroquine or control (n≥6 per group, *** p<0.001 by Student's t-test). **(E)** Quantification of cleaved caspase-3 positive IEC in the small intestine of chloroquine-treated or control *β-cat*$^{c.a.}$ mice 15 days after the start of tamoxifen administration (n=4/group, ≥20 400X-high-power fields (HPF) have been counted per animal, *** p<0.001 by Student's t-test). Please note that parts of the figure have been reproduced from Figure 4.3A for better visibility. **(F)** Villus length relative to average crypt length per mouse in the small intestine of chloroquine-treated or control *β-cat*$^{c.a.}$ mice 15 days after the start of tamoxifen administration (n=3 mice per group, *** p<0.001 by Student's t-test). Please note that parts of the figure have been reproduced from Figure 4.3B for better visibility. **(G, H)** H&E staining of the small intestine of chloroquine-treated (H) or untreated (G) *β-cat*$^{c.a.}$ and mice 15 days after the start of tamoxifen administration indicating decrease in crypt-hyperproliferation in chloroquine-treated mice. Scale bar = 100 µm. **(I)** Kaplan-Meier survival curve of chloroquine treated (n=8), chloroquine and anti-CD8-antibody treated (n=6) or untreated *β-cat*$^{c.a.}$ mice (n= 15); * p<0.05, *** p< 0.001 by log-rank test. The dashed line (for *β-cat*$^{c.a.}$ mice) has been reproduced from Figure 1.10 for better comparison. **(J)** Flow cytometric quantification of SIINFEKL-MHC pentamer binding $CD3^+CD8^+$ T cells in the colon of *OVA*^{IEC} mice injected daily for one week with chloroquine or saline at week 13 of the AOM model (n=6 mice each, * p<0.05 by Student's t-test). **(K)** Histological quantification of mean tumor size in AOM-treated mice that received daily chloroquine or saline injections for 4 weeks starting 10 weeks after the last AOM injection (n=5 or 8 mice, respectively, * p<0.05 by Student's t-test).

4.3 LMP Triggers Activation of Cytotoxic T cells *in vitro*

To further examine the link between LMP in early stage tumor cells and $CD8^+$ T cell recruitment, we established an *ex vivo* co-culture system, comprised of an ovalbumin expressing murine (C57BL/6-derived) colon carcinoma cell line (OVA-CMT93) that was co-cultured together with splenocytes from OT-I mice. This mouse line harbors cytotoxic T cells expressing a transgenic T cell receptor (TCR) that recognize the ovalbumin-derived peptide SIINFEKL (OVA257-264). T cell activation was quantified by measurement of IFNγ released by OT-I cells (Figure 4.12A). RNAi-mediated gene knockdown of *Stat3* was accomplished by stable expression of antisense *Stat3*-microRNA (OVA-CMT^{Stat3KD}) or scrambled control (OVA-CMT^{scr}) and was confirmed by immunoblotting (Figure 4.12B). Indeed, OVA-CMT^{Stat3KD} cells were more susceptible to peroxide-induced LMP than OVA-CMT^{scr} cells as assessed by flow cytometric monitoring of the reduction in acidophilic acridine orange staining (Figure 4.12C). While unchallenged Stat3-deficient or -proficient cells resulted in similar OT-I T cell activation, induction of LMP in tumor cells by H_2O_2-treatment prior to their co-culture with OT-I splenocytes significantly elevated IFNγ production (Figure 4.12D). Similar to the *in vivo* situation and consistent with a higher degree of LMP, IFNγ release by OT-I cells was greatly enhanced in OVA-CMT^{Stat3KD}. Furthermore, treatment of OVA-CMT^{Stat3KD} cells with the pan-cysteine protease inhibitor E64d reduced IFNγ release (Figure 4.12E), further supporting the notion that LMP-dependent protease release may be involved in antigen processing in OVA-CMT93 cells.

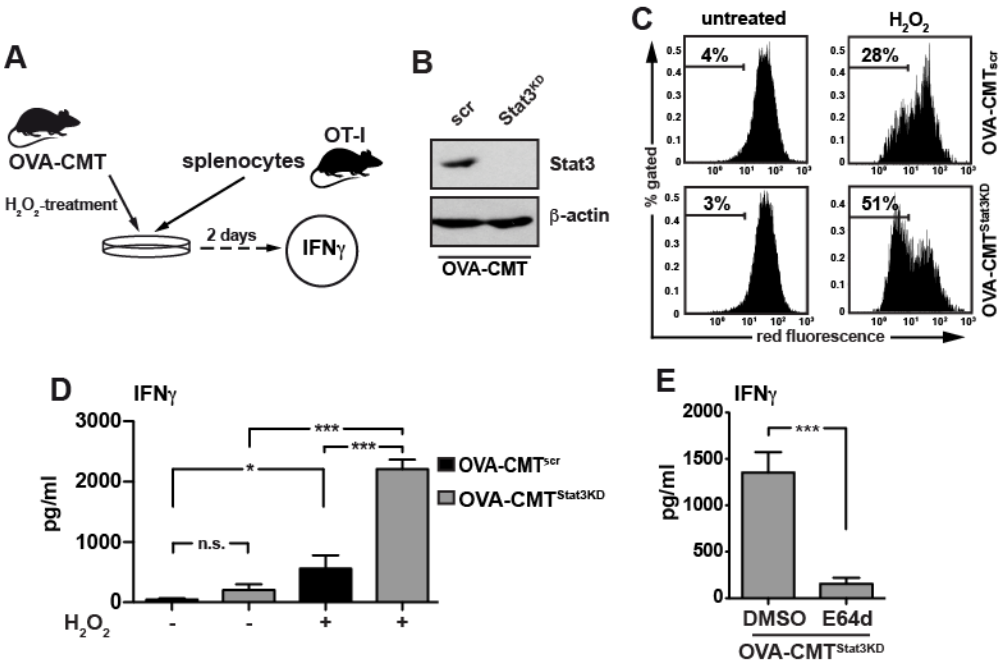

Figure 4.12: Stat3-Deficient Tumor Cells Undergoing LMP Activate Antigen-Specific T Cells *in vitro*. (A) Experimental set up of co-culture experiment: OVA-CMT cells were either untreated or pre-treated with H_2O_2 (1 mM) for 2 hours prior to a 48-hour incubation with OT-I splenocytes. **(B)** Immunoblot analysis of STAT3 in OVA-expressing CMT cells that were additionally stably transfected with pcDNA6.2-GW/scrambled or pcDNA6.2-GW/Stat3-miRNA. **(C)** Representative flow cytometric analysis of acridine orange stained OVA-CMT^{scr} and OVA-CMT^{Stat3KD} cells reveals increased loss of red fluorescence 6 hours after H_2O_2 challenge in OVA-CMT^{Stat3KD} cells indicating elevated LMP. **(D)** IFNγ levels in the supernatant of OT-I splenocytes that had been co-cultured for two days with OVA-CMT^{scr} or OVA-CMT^{Stat3KD} cells. OVA-CMT cells had been left either untreated or stimulated with H_2O_2 (1 mM) for 2 hours prior to co-culture with OT-I splenocytes (n=6 from 2 independent experiments, * $p < 0.05$, *** $p < 0.001$). **(E)** IFNγ levels in supernatants of OT-I splenocytes that had been co-cultured for two days with OVA-CMT^{Stat3KD} cells. OVA-CMT^{Stat3KD} cells had been pretreated with H_2O_2 (1 mM) for 2 hours in the presence of the cysteine protease inhibitor E64d (10 mg/ml) prior to co-culture with OT-I splenocytes. Note that protease inhibitor was present only during H_2O_2 stimulation but absent during co-culture with OT-I cells (*** $p < 0.001$ by Student's t-test, n=6 from 2 independent experiments).

4.3.1 *Stat3-Deficient Tumor Cells are Efficient Antigen-Donors for Cross-Dressing DC and T Cell Activation*

In order to evaluate the contribution of professional antigen presenting cells to T cell activation by tumor cells we co-cultured OVA-CMT^{Stat3KD} or OVA-CMT^{scr} cells together with MACS-purified OT-I CD8$^+$ T cells in the absence of DC. Indeed, this was sufficient to induce IFNγ secretion (Figure 4.13A), however, IFNγ levels were greatly enhanced when CD11c$^+$ DC were added in a dose-dependent manner

(Figure 4.13B). This suggested that OVA-CMT^{Stat3KD} cells were able to generate and present the respective antigen for activation of OT-I CD8$^+$ T cells themselves. We hypothesized that DC could enhanced the activation of T cells by displaying MHC-I bound SIINFEKL acquired from tumor cells, a phenomenon termed cross-dressing, rather than by cross-presenting antigens derived from ovalbumin-proteolysis within DC (Nakayama, 2014). We tested this hypothesis in an experiment comparing the effect of antigen-expressing tumor cells of two different MHC-haplotypes, either matched or mismatched to the T cells used, thereby using the self-MHC restriction of T cells (see section 1.4.3). We co-cultured DC from wildtype or *Tap1*-deficient mice and OT-I CD8 T cells, both on C57BL/6 background (haplotype H-2^b), together with either ovalbumin-expressing CT26 colon tumor cells of BALB/c origin (OVA-CT26^{Stat3KD} and OVA-CT26^{scr}, haplotype H-2^d) or C57BL/6-derived haplo-identical OVA-CMT^{Stat3KD} and OVA-CMT^{scr} (haplotype H-2^b, Figure 4.13C, D). In the presence of CT26 cells no OT-I T cell activation could be observed irrespective of whether CT26 cells had been pretreated with H_2O_2 or not. Instead, T cell activation was only triggered by haplo-identical OVA-CMT cells regardless of presence or absence of *Tap1* in DC (Figure 4.13E). This supports the notion that T cell activation occurred independently of antigen-processing in DC, which would be required for cross presentation. In contrast, knockdown of *Tap1* in tumor cells prevented IFNγ production by OT-I cells (Figure 4.13F, G), providing further evidence that generation of the antigenic peptide can occur directly in tumor cells.

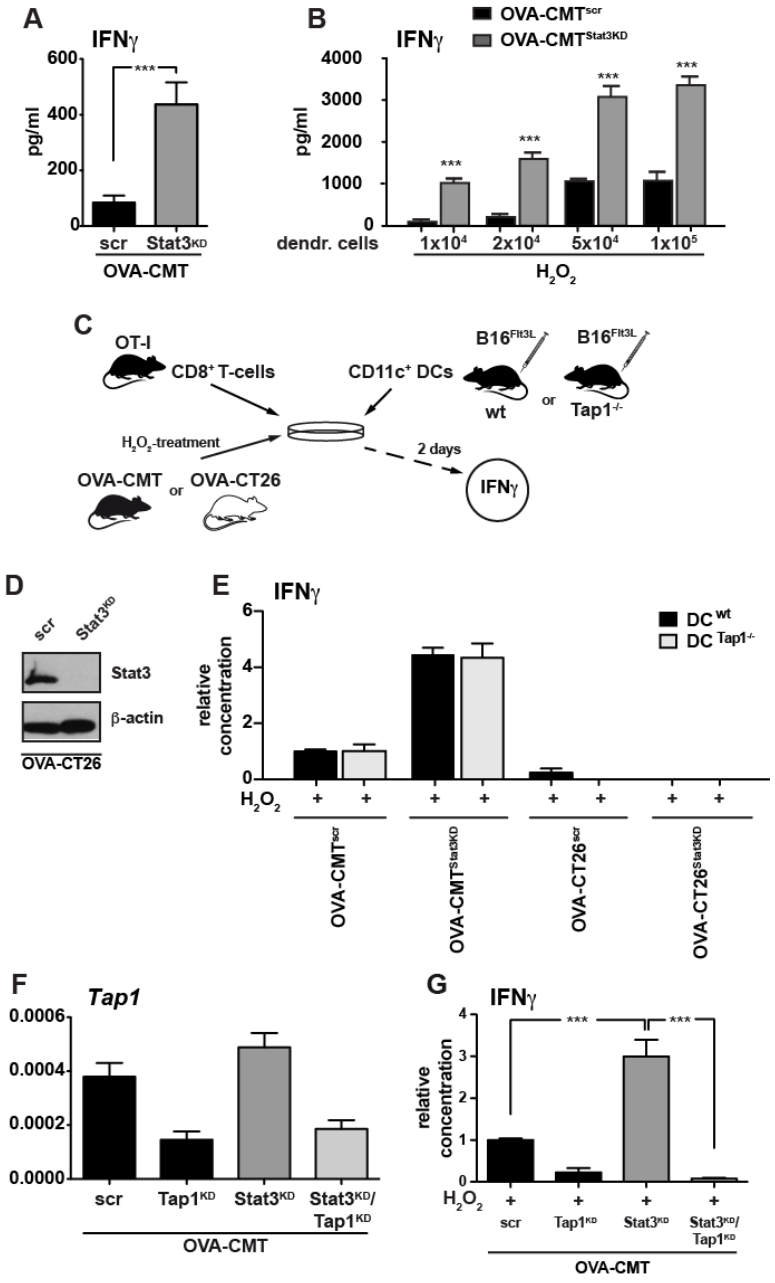

Figure 4.13: T Cell Activation Depends on Antigen Processing in Tumor Cells. (A) IFNγ levels in supernatants of purified $CD8^+$ OT-I T cells in the absence of $CD11c^+$ dendritic cells that had been co-cultured for two days with OVA-CMT^{scr} or OVA-$CMT^{Stat3KD}$ cells which had been pre-treated with H_2O_2 (1 mM) for 2 hours (*** $p < 0.001$ by Student's t-test, n=6 from 2 independent experiments). **(B)** IFNγ levels in supernatants of purified $CD8^+$ OT-I T cells along with increasing numbers of $CD11c^+$ dendritic cells that had been co-cultured for two days with OVA-CMT^{scr} or OVA-$CMT^{Stat3KD}$ cells which had been pre-treated with H_2O_2 (1 mM) for 2 hours (*** $p < 0.001$ by Student's t-test, $n \geq 3$ from 2 independent experiments). **(C)** Experimental set up of co-culture experiments using either OVA-CMT or OVA-CT26 cells that upon H_2O_2 stimulation are co-cultured with $CD11c^+$ dendritic cells from wildtype or *Tap1*$^{-/-}$ mice and OT-I CD8+ T cells. **(D)** Immunoblot analysis of STAT3 in OVA-expressing CT26 cells that were additionally stably transfected with pcDNA6.2-GW/scrambled or pcDNA6.2-GW/Stat3-miRNA. **(E)** IFNγ levels in supernatants of OT-I T cells that had been co-cultured with *wt* or *Tap1*$^{-/-}$ $CD11c^+$ dendritic cells as well as with H_2O_2 stimulated OVA-CMT or OVA-CT26 cells for 48 hours (n=6 from 2 independent experiments). **(F)** OVA-CMT cells have been transfected with the indicated siRNA and analyzed 2 days later for the expression of *Tap1* (n=3 each). **(G)** IFNγ levels in supernatants of OT-I splenocytes that had been co-cultured for 48 hours with H_2O_2 stimulated OVA-CMT cells with siRNA-mediated knockdown of Tap1 and/or Stat3 (n=6 from 2 independent experiments, *** $p<0.001$ by Student's t-test).

To further investigate the role of DC in T cell activation we cultured DC of either H-2^{d}- or H-2^{q}-haplotype together with OT-I T cells and OVA-CMT^{Stat3KD} or OVA-CMT^{scr} cells (H-2^{b}) and presence of DC of both haplotypes was effective to enhance stimulation of OT-I T cells in a dose-dependent manner when cultured together with OVA-CMT^{Stat3KD} cells but not with OVA-CMT^{scr} cells (Figure 4.14A, B). The ability of Stat3-deficient tumor cells to act as antigen-donor cells for DC cross-dressing after LMP induction was further supported by the detection of the BALB/c-derived MHC-I protein H-2D^{d} on C57BL/6 DC following co-culture of C57BL/6 splenocytes together with H_2O_2 pre-treated BALB/c CT26 cells. Again, the transfer of MHC-I molecules from tumor cells to DC occurred independently of *Tap1* expression in DC (Figure 4.14C, D). Taken together, these results further strongly supported our hypothesis that Stat3-deficient tumor cells can directly process antigens in an LMP dependent manner and cross-dress DC to induce an effective CD8^{+} T cell response.

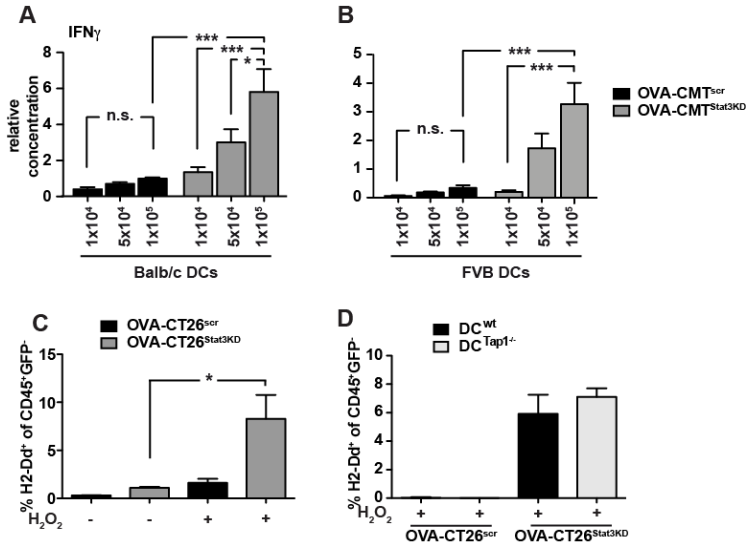

Figure 4.14: Stat3-Deficient Tumor Cells Undergoing LMP Activate T Cells by DC Cross-Dressing. (A, B) IFNγ levels in supernatants of purified $CD8^+$ OT-I T cells co-cultured for 48 hours with OVA-CMT^{scr} or OVA-$CMT^{Stat3KD}$ cells and the indicated number of $CD11c^+$ dendritic cells from Balb/c (A) or FVB (B) donors (n=12 from 4 independent experiments, * $p<0.05$, *** $p<0.001$ by one-way ANOVA). **(C)** Flow cytometric quantification of Balb/c-derived H2-D^d on $CD45^+GFP^-$ splenocytes from wildtype C57B/6 donor mice co-cultured for 6 hours with OVA-$CT26^{scr}$ or OVA-$CT26^{Stat3KD}$ cells (of Balb/c origin) after treatment of OVA-CT26 cells with H_2O_2 (1 mM) for 2 hours where indicated (n=6 from 2 independent experiments, * $p<0.05$ by Stundent's t-test). **(D)** Quantification of H2-D^d on $CD45^+GFP^-$ splenocytes from *wt* or *Tap1*$^{-/-}$ C57B/6 donor mice co-cultured for 2 days with OVA-$CT26^{scr}$ or OVA-$CT26^{Stat3KD}$ cells after treatment of OVA-CT26 cells with H_2O_2 (1 mM) for 2 hours (n=6 from 2 independent experiments).

4.3.2 *Identification of Proteases Responsible for Antigen-Processing in Tumor Cells Undergoing LMP*

Since our results suggested that T cell activation depended on LMP and proteases activity within tumor cells rather than DC, we aimed to identify the specific contribution of putative proteases in antigen processing. As the broad-spectrum cysteine proteases inhibitor E64d was effective in blocking T cell activation both *in vivo* and *in vitro*, we focused on the group of lysosomal cysteine proteases, also called cathepsins. While the prominent role of the cytosolic protease in generating MHC I antigens is well documented, cathepsin S and L are required for MHC-II mediated antigen presentation in APC and IEC or thymic cortical epithelial cells, respectively (Beers et al., 2005; Nakagawa et al., 1998). In addition, cathepsin S is involved in generation of peptides presented via the vacuolar pathway of cross-presentation in DC (Shen et al., 2004).

To evaluate whether cathepsin S, cathepsin L or alternative cathepsins might be responsible for MHC class I-mediated antigen presentation in Stat3-deficient tumor cells, we individually knocked down expression of single cathepsins B, D, F, H, L or S in OVA-CMT^{Stat3KD} cells and examined IFNγ release by OT-I T cells upon H_2O_2-treatment prior to the co-culture. Indeed, reduced expression of either cathepsin S or cathepsin L in OVA-CMT^{Stat3KD} cells effectively decreased T cell activation as assayed by IFNγ release, while knockdown of the other cathepsins had no effect (Figure 4.15A). To confirm the contribution of cathepsin S and cathepsin L to the observed phenotype in Stat3-deficient/β-catenin mutant IEC *in vivo*, we crossed *Ctss*$^{-/-}$ whole body mutants to *β-cat*$^{c.a.}$/*Stat3*$^{\Delta IEC}$ animals. To our surprise, cathepsin S-deficiency in the corresponding *Ctss*$^{-/-}$/*β-cat*$^{c.a.}$/*Stat3*$^{\Delta IEC}$ mice did not affect *Ifng* expression on day 15. Similarly, neither IEC restricted deletion of cathepsin L (*Ctsl*$^{\Delta IEC}$/*β-cat*$^{c.a.}$/*Stat3*$^{\Delta IEC}$) nor simultaneous loss of cathepsin S and L resulted in a reduction of IFNγ upregulation (Figure 4.15B). In addition, no effect on LMP in IEC of *Ctss*$^{-/-}$/*Ctsl*$^{\Delta IEC}$/*β-cat*$^{c.a.}$/*Stat3*$^{\Delta IEC}$ mice could be observed (Figure 4.15C). These results were paralleled by quantification of protease activity in IEC of mice of those genotypes which showed rather elevated enzymatic activity when tested with the cathepsin substrate z-Leu-Arg-AMC (Figure 4.15D). Taken together these results show that cathepsin S and L likely contribute to antigen processing in tumor cells undergoing LMP *in vitro*, the proteolytic effect of cathepsins overlap and the loss of one member of the cathepsin family can be compensated by other proteases *in vivo* in line with earlier reports from cathepsin knock-out mice and a recent report from a pancreatic neuroendocrine tumor model (Akkari et al., 2016; Turk et al., 2001).

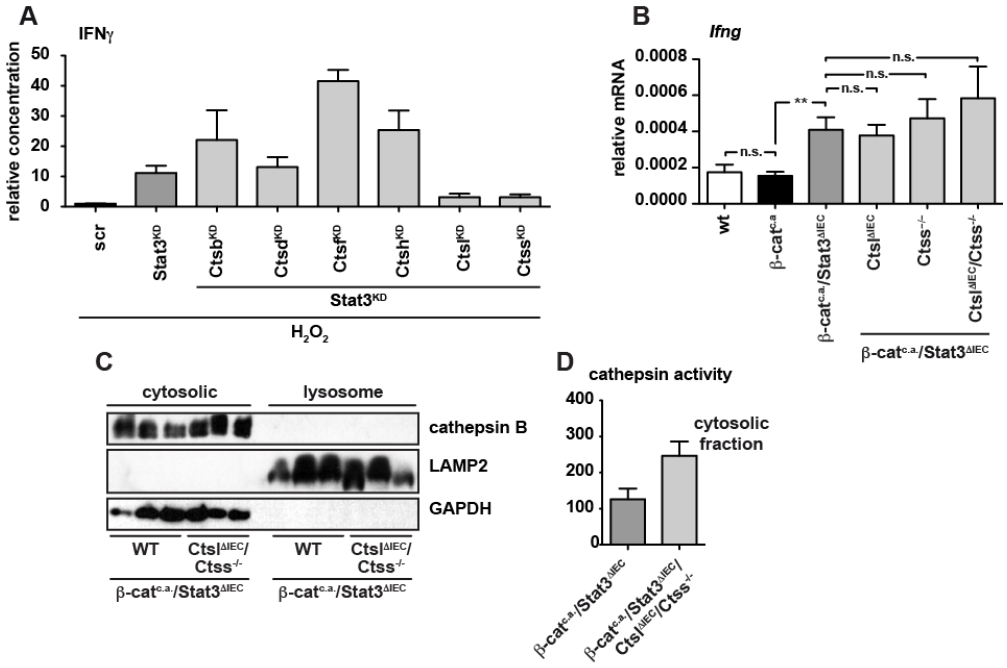

Figure 4.15: High Redundancy of Cathepsin-Proteases *in vivo*. (A) IFNγ levels in the supernatant of OT-I splenocytes that had been co-cultured for two days with OVA-CMT cells with RNAi-mediated knockdown of the indicated genes. OVA-CMT cells had been stimulated with H_2O_2 (1 mM) for 2 hours prior to co-culture with OT-I splenocytes ($n \geq 6$ from 3 independent experiments, * $p < 0.05$, *** $p < 0.001$). **(B)** Relative *Ifng* mRNA expression in small intestinal mucosa of mice with the indicated genotype 15 days after the start of tamoxifen administration. ($n \geq 7$, ** $p<0.01$ by Student's t-test). **(C)** Immunoblot analysis of cathepsin B, LAMP2 and Gapdh in cytosolic and membrane fractions isolated from small intestinal IEC of *β-cat*$^{c.a.}$/*Stat3*$^{\Delta IEC}$ and *β-cat*$^{c.a.}$/*Stat3*$^{\Delta IEC}$/Ctsl$^{\Delta IEC}$/Ctss$^{-/-}$ mice 3 days after the start of tamoxifen administration. **(D)** Protease activity of cytosolic cathepsins as measured using the fluorogenic substrate z-Phe-Leu-AMC (measured in duplicates from $n \geq 3$ mice, * $p<0.05$).

4.4 Lysosomal Iron(II) Accumulation is a Result of Enhanced Mitophagy and Triggers LMP

Next, we aimed to address the mechanism causing LMP, which is the result of lysosomal destabilization by various stimuli, most commonly iron(II) mediated generation of lipid radicals from ROS molecules (Boya and Kroemer, 2008; Terman et al., 2006). In the presence of bivalent (ferrous) iron reactive oxygen species can generate lipid radicals damaging lysosomal membranes (see section 1.6). ROS production is a well-known feature of tumor cells and oncogenic Wnt activation has been described to trigger ROS production in IEC (Myant et al., 2013).

In order to quantify the cellular bivalent iron load we used the novel fluorescent Fe^{2+}-specific probe IP-1 (Au-Yeung et al., 2013). In line with elevated

LMP susceptibility the IP-1 signal was markedly increased in Stat3-deficient CMT93 cells (Figure 4.16A-D). The signal of the iron probe IP-1 co-localized with LysoTracker fluorescence, confirming lysosomes as the predominant intracellular site of iron(II) accumulation in OVA-CMT cells (Figure 4.16E-J). However, we were not able to detect increased expression of genes coding for proteins involved in iron metabolism (Figure 4.16K) including proteins responsible for intracellular iron storage (*Ftl1*, *Fth1*), iron uptake (*Heph*, *Tfrc1*, *Scl40a1*), general regulation of iron metabolism (*Aco1*, *Ireb2*), metal-sensing transcription factors (*Mtf1*, *Mtf2*, *Pir*) or metabolism of other metals (*Mt1a*, *Mt2*, *Mt3*, *Cp*).

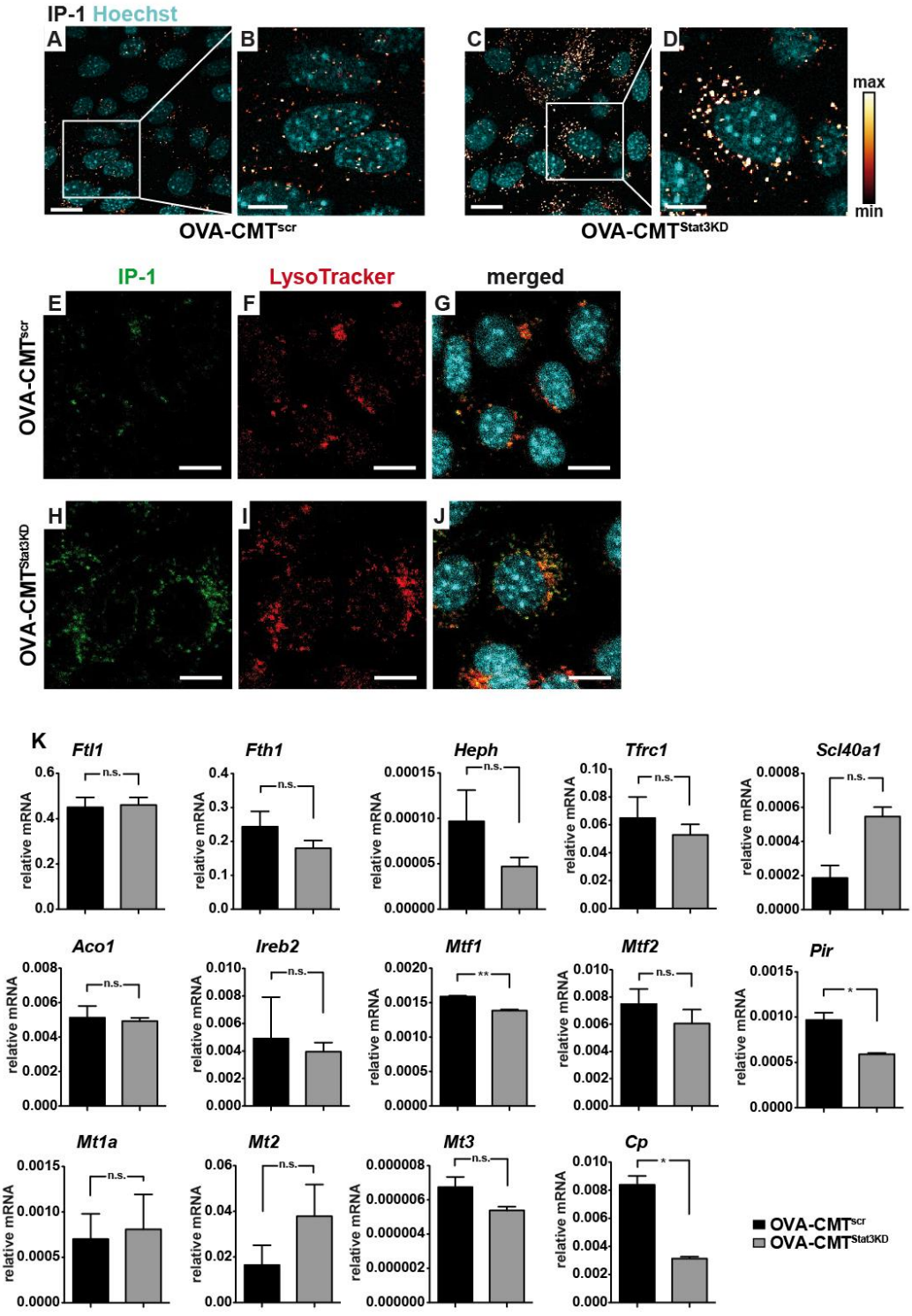

Figure 4.16: Stat3-Deficient Tumor Cells Show Accumulation of Lysosomal Ferric Iron. (A-D) Iron content of OVA-CMT^{scr} or OVA-CMT^{Stat3KD} cells was measured by confocal live cell microscopy and the fluorescent Fe^{2+}-specific probe IP-1. The intensity of IP-1 is shown by a red-yellow LUT depicted on the right-hand side. Scale bar = 20 µm (A, C) or 10 µm (B, D). **(E-J)** Confocal live cell microscopy of OVA-CMT^{scr} (E-G) or OVA-CMT^{Stat3KD} cells stained with IP-1 (green) and the lysosomotropic dye LysoTracker (red) to confirm lysosomal localization of iron. Blue staining in the merged images (G, J) represent Hoechst nuclear staining, yellow color indicates co-localization of IP-1 and LysoTracker signal. Scale bar = 10 µm. Please note the depicted sections in (E-G) and (H-J) represent the same cells than those depicted in (A) and (C), respectively. **(K)** Relative mRNA level of the indicated iron-related gene in OVA-CMT^{scr} or OVA-CMT^{Stat3KD} cells (n=2 each).

An alternative source for lysosomal iron is autophagy of iron containing proteins. Indeed, we observed an increased presence of components of the mitochondrial oxidative phosphorylation system when probed with an antibody cocktail recognizing components of all 5 respiratory chain complexes (OXPHOS) or an antibody specific for cytochrome c oxidase subunit II (COXII) in lysosomes of OVA-CMT^{Stat3KD} cells (Figure 4.17A-H). This was suggestive of enhanced mitophagy, a process selectively eliminating damaged or excessive mitochondria by the autophagic pathway known to be a major contributor of lysosomal iron levels due to the high iron content of mitochondria (Terman et al., 2006; Youle and Narendra, 2011).

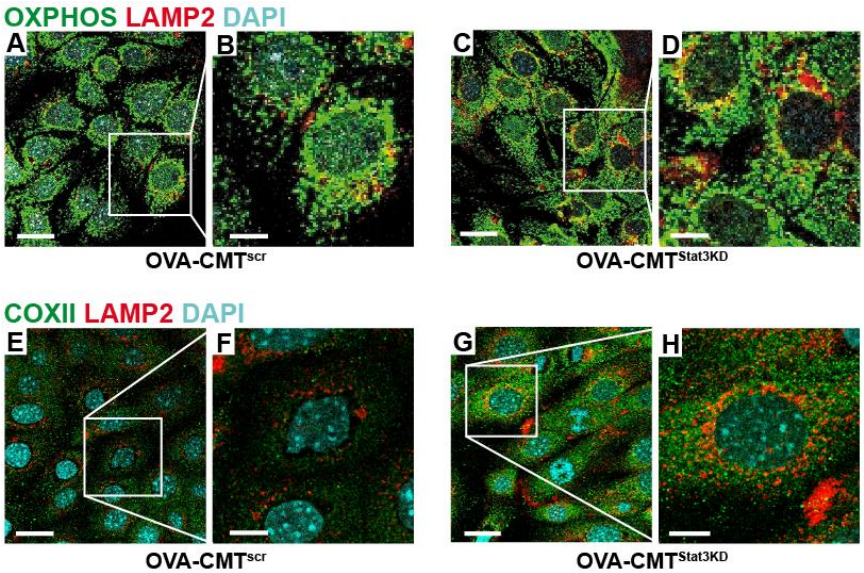

Figure 4.17: Stat3-Deficiency in Tumor Cells Increases Mitophagy. (A-H) Mitophagy in OVA-CMT^{scr} (A, B, E, F) and OVA-CMT^{Stat3KD} (C, D, G, H) was visualized by co-staining for mitochondrial proteins using OXPHOS-antibody cocktail or COXII-specific antibody (green) and the lysosomal membrane protein LAMP2 (red) and analyzed by confocal laser scanning microscopy. Scale bar=25µm (A, C, E, G) or 10µm (B, D, F, H).

4.4.1 *Stat3 Controls Mitochondrial Function and Turnover*

Interestingly, serine-phosphorylated Stat3 has been found to be involved in mitochondrial function to preserve oxidative phosphorylation in cardiac and nerve

cells as well as RAS-transformed tumor cells (Gough et al., 2009; Wegrzyn et al., 2009). In contrast, a transcriptionally constitutive active mutant of Stat3 (Stat3C) has been found to induces a metabolic switch towards aerobic glycolysis in a Hif1α-dependent manner (Demaria et al., 2010). In Stat3-deficient CMT93 cells we observed decreased glucose-uptake, increased ATP levels and increased basal and maximal oxygen consumption rates (Figure 4.18A-E), suggesting enhanced oxidative phosphorylation. The functional consequences of enhanced mitochondrial activity were demonstrated by increased proliferation of in OVA-CMT^{Stat3KD} cells in carbohydrate-deficient medium, or in the presence of the glycolysis inhibitors bromopyruvate or deoxyglucose, or in medium containing galactose as carbohydrate source, conditions where mitochondrial activity is required to yield a positive energy balance. In contrast proliferation was indifferent in the presence of glucose (Figure 4.18F). Taken together, OVA-CMT^{Stat3KD} showed increased mitochondrial activity and lower dependency on glycolysis for energy metabolism than their Stat3-profient controls.

Using MitoTracker deep red, a fluorescent dye that accumulates in mitochondria in a quantitative way, we found that the mitochondrial biomass of Stat3-deficient cells is elevated (Figure 4.18G). However, when we stained cells with the fluorescent substance TMRM that is sensitive for the mitochondrial membrane potential, an indicator of mitochondrial integrity and activity, we detected a reduced signal for TMRM fluorescence in a larger proportion of OVA-CMT^{Stat3KD} than OVA-CMT^{scr} cells, indicating mitochondrial turnover in this fraction of cells (Figure 4.18H). In addition, we semi-quantitively assessed the turnover of mitochondria over a period of 48 hours days using MitoTimer, a vector expressing a mitochondria-tagged derivative of dsRed, which changes its fluorescent properties over time,

controlled by a "TET-ON" promoter (Hernandez et al., 2013). Indeed, OVA-CMT^{Stat3KD} cells showed an elevated ratio of new to old mitochondria compared to OVA-CMT^{scr}, strongly suggesting increased turnover of mitochondria (Figure 4.18I).

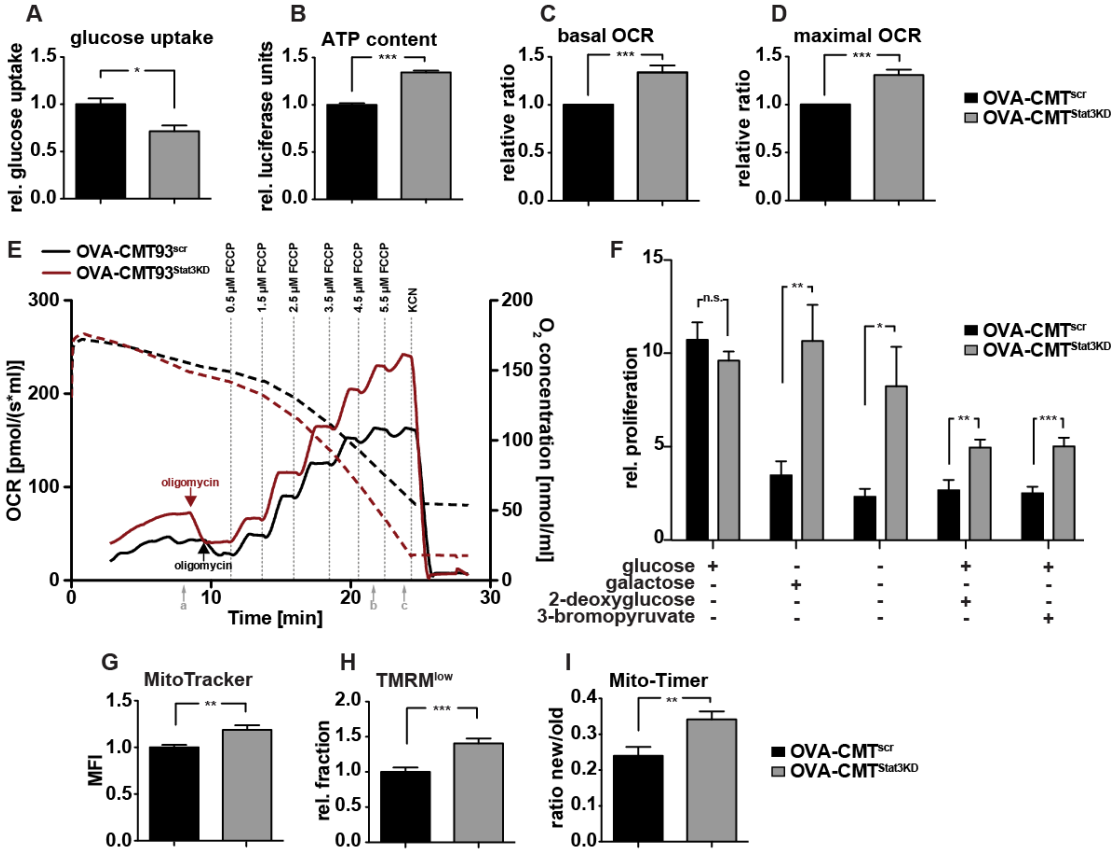

Figure 4.18: Increased Mitochondrial Activity and Turnover in Stat3-Deficient Tumor Cells. (A) Relative uptake of glucose as measured by decrease in the concentration in the supernatant over 12 hours (* $p<0.05$ by Student's t-test, n=7 from 2 independent experiments). **(B)** ATP content of the indicated cells as measured by luciferase activity (*** $p<0.001$ by Student's t-test, n=12 from 4 independent experiments). **(C-E)** Oxygen consumption rate was analyzed by respirometry using equal number of intact cells in FCS-supplemented DMEM (n=10 from 10 independent experiments). (C) The basal rate was measured after an initial stabilization time (position a in (E), *** $p<0.001$ by one-sample t-test). (D) The maximal rate was measured after addition of a saturating amount of the uncoupling agent FCCP (position b and c for OVA-CMT^{scr} and OVA-CMT^{Stat3KD}, respectively, in (E), *** $p<0.001$ by one-sample t-test). (E) O_2-concentration in dashed lines (right hand scale) and oxygen consumption rate (OCR) in solid lines (left hand scale) during a representative experiment. **(F)** Relative proliferation of OVA-CMT^{scr} or OVA-CMT^{Stat3KD} cells in presence or absence of the indicated carbohydrates or inhibitors of glycolysis for 3 days (n=6 of 2 independent experiments, * $p<0.05$, ** $p<0.01$, *** $p<0.001$ by Student's t-test). **(G)** Relative mean fluorescent intensity (MFI) of OVA-CMT^{scr} or OVA-CMT^{Stat3KD} cells incubated with MitoTracker (** $p<0.01$ by Student's t-test, n=11 from 3 independent experiments). **(H)** Relative fraction of cells showing low TMRM staining indicating low mitochondrial membrane potential ($p<0.001$ by Student's t-test, n=9 from 3 independent experiments). **(I)** Ratio of cells showing green or red fluorescence of MitoTimer, indicating new or old mitochondria, respectively (** $p<0.01$ by Student's t-test, n=18 from 3 independent experiments).

4.4.2 *Serine-Phosphorylation of STAT3 is Required to Suppress LMP-Induction*

To test the involvement of mitochondrial STAT3 in LMP induction, we used *Stat3*$^{-/-}$ fibroblasts and triggered LMP by H_2O_2 treatment. Retroviral reconstitution of *Stat3*$^{-/-}$ cells with either wildtype Stat3, a mitochondrial-targeted version of Stat3 (MLS-Stat3), a dominant negative tyrosine-to-phenylalanine mutant (MLS-Stat3Y705F), or a mutant defective in DNA binding (MLS-Stat3E434A/E435A) all reverted the increased level of LMP to levels comparable to *Stat3*$^{+/+}$ control cells (Figure 4.19A). In contrast, reconstitution of *Stat3*$^{-/-}$ cells with a construct expressing a *Stat3*-mutant containing additional inactivation of the S727 phosphorylation site (MLS-Stat3Y705F/S727A) yielded in LMP induction comparable to (non-reconstituted) *Stat3*$^{-/-}$ cells and elevated in comparison with the other mutants. Therefore, we speculate that LMP was prevented by S727 phosphorylated STAT3 in mitochondria rather than transcriptional activity of STAT3, which requires Y705-phosphorylation and DNA binding. Accordingly, expression levels of Stat3-dependent genes involved in glycolysis or mitochondrial respiration (Demaria et al., 2010) were not markedly changed in OVA-CMT^{Stat3KD} cells (Figure 4.19B). Taken together this data indicates that STAT3 controls LMP and metabolic alterations in CMT93-cells by its serine-phosphorylated form in a direct mitochondrial fashion rather than by transcriptional regulation of lysosomal function and metabolism.

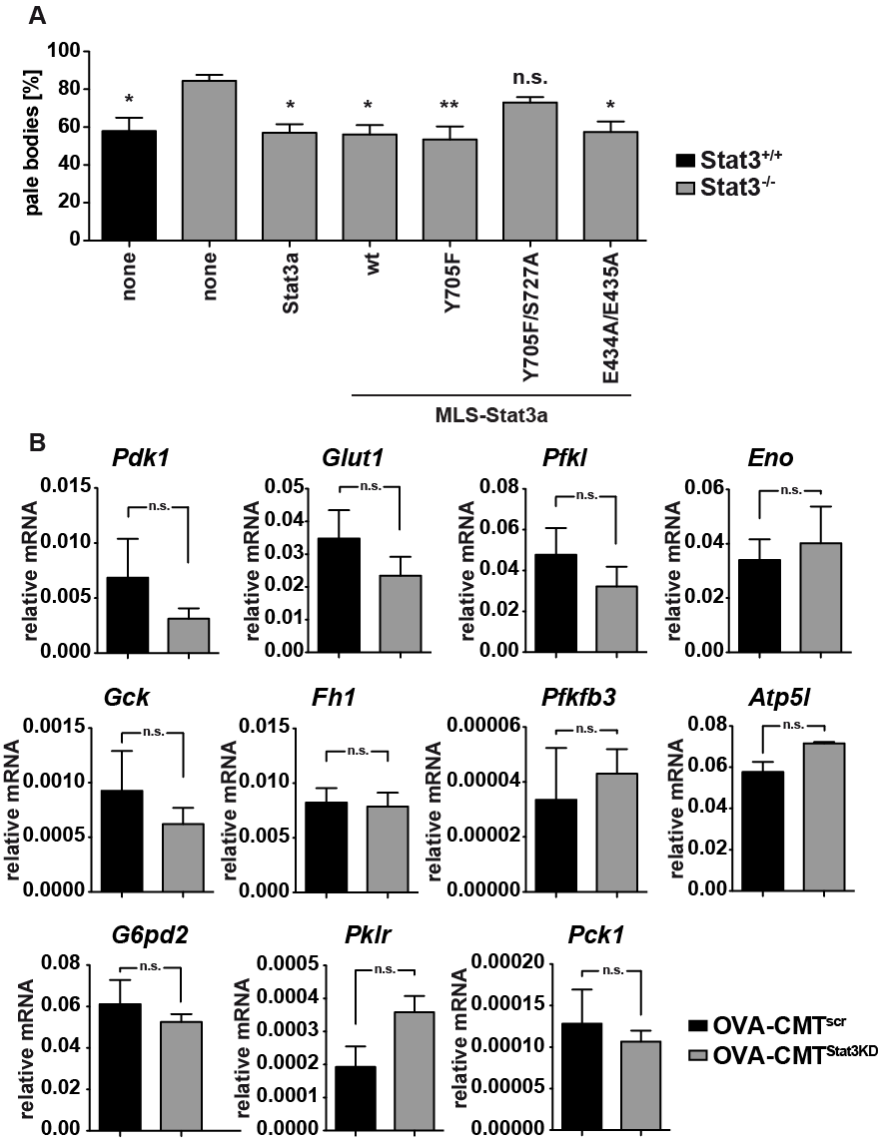

Figure 4.19: Mitochondrial Serine-Phosphorylated STAT3 Suppresses LMP. (A) Relative amount of pale bodies in MEFs of the indicated genotype reconstituted with the indicated variant of Stat3a after treatment with H_2O_2 (1 mM) for 2 hours and additional incubation in normal medium for 6 hours (n=7 of 3 independent experiments, * $p<0.05$, ** $p<0.001$ by one-way ANOVA against not-reconstituted $Stat3^{-/-}$ MEFs). **(B)** Relative mRNA level of the indicated metabolism related gene in OVA-CMT^{scr} or OVA-$CMT^{Stat3KD}$ cells (n=2 each).

4.4.3 *Enhanced Mitochondrial Activity and Degradation in IEC of β-cat$^{c.a.}$/Stat3$^{\Delta IEC}$ mice*

Comparable with effects observed in Stat3-deficient CMT cells *in vitro*, immunofluorescence staining for COXII or OXPHOS proteins indicated the presence of mitochondrial remnants in lysosomes of IEC compared to *β-cat*$^{c.a.}$ control animals

indicating Stat3-controlled mitophagy *in vivo*, while expression levels of genes controlling glycolysis were again unchanged (Figure 4.20A-I).

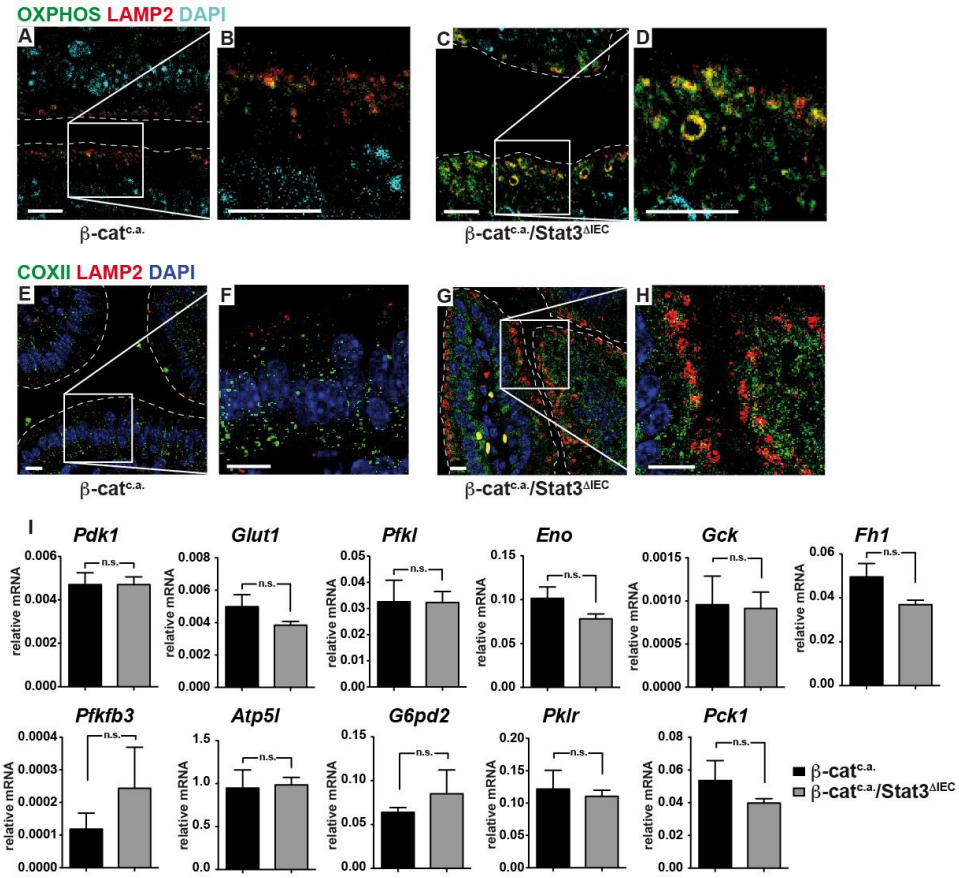

Figure 4.20: Enhanced Mitophagy in Intestines of *β-cat*$^{c.a.}$/*Stat3*$^{\Delta IEC}$ Mice. (A-H) Mitophagy in the epithelium of the small intestine of *β-cat*$^{c.a.}$ (A, B, E, F) and *β-cat*$^{c.a.}$/*Stat3*$^{\Delta IEC}$ mice (C, D, G, H) 3 days after the start of tamoxifen administration was visualized by co-staining for mitochondrial proteins using OXPHOS-antibody cocktail or COXII-specific antibody (green) and the lysosomal membrane protein LAMP2 (red) and analyzed by confocal laser scanning microscopy. Images are representative for 3 mice, Scale bar = 10 µm, dashed lines represent approximate luminal borders of intestinal mucosa. **(I)** Relative mRNA level of the indicated metabolism related gene in IEC of *β-cat*$^{c.a.}$ and *β-cat*$^{c.a.}$/*Stat3*$^{\Delta IEC}$ mice 3 days after the start of tamoxifen administration (n=3 each).

In order to functionally confirm our findings *in vivo*, we measured the enzymatic activity of citrate synthase and the intracellular NAD^+/NADH ratio as proxy measurements for mitochondrial activity in IEC of *β-cat*$^{c.a.}$/*Stat3*$^{\Delta IEC}$ or control mice. Both values were elevated in Stat3-deficient IEC suggesting higher mitochondrial activity (Figure 4.21A, B). In addition, electron microscopy confirmed morphological changes in mitochondrial ultrastructure such as cristaelysis (Figure

4.21C, D) in line with increased mitochondrial degradation. Moreover, immunoblot analysis revealed elevated activation of Drp1 in *β-cat*$^{c.a.}$/*Stat3*$^{\Delta IEC}$ IEC (Figure 4.21E), a protein controlling mitochondrial fission. Furthermore, conversion of LC3-I to LC3-II in *β-cat*$^{c.a.}$/*Stat3*$^{\Delta IEC}$ IEC was elevated suggesting enhanced autophagosome formation, yet simultaneous accumulation of p62 suggested decreased autophagic flux (Figure 4.21F, G) in agreement with induction of mitophagy but impaired lysosomal function.

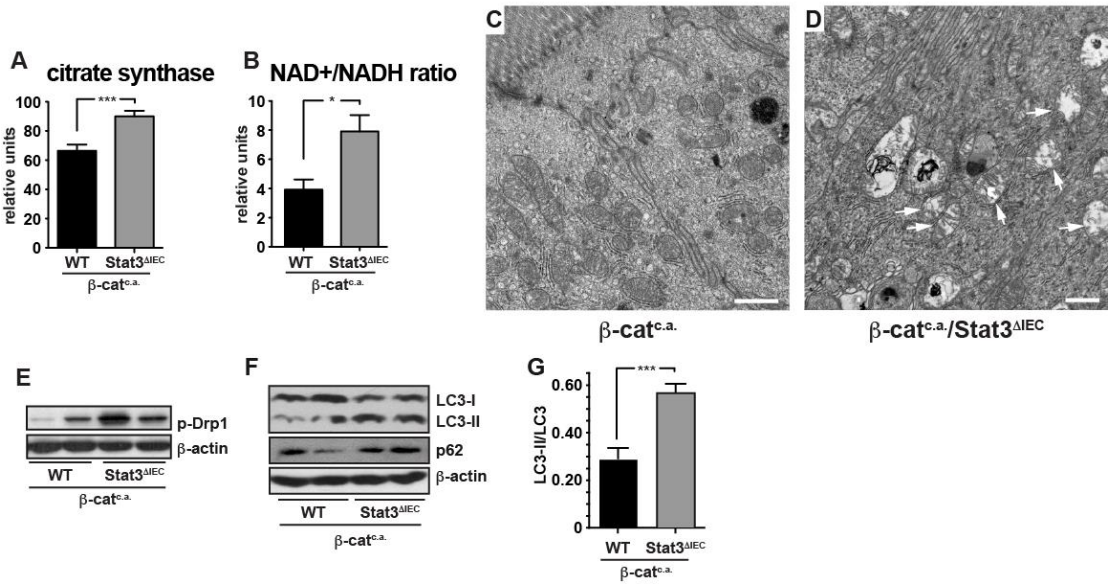

Figure 4.21: Altered Mitochondrial Ultrastructure in Stat3-Deficient IEC. (A) Enzymatic activity of citrate synthase in mitochondrial isolates of IEC of *β-cat*$^{c.a.}$ and *β-cat*$^{c.a.}$/*Stat3*$^{\Delta IEC}$ mice 3 days after the start of tamoxifen administration. Samples were normalized to total protein content and measured in triplicates of 6 mice each. **(B)** Ratio of NAD^+ to NADH in the small intestine of *β-cat*$^{c.a.}$ and *β-cat*$^{c.a.}$/*Stat3*$^{\Delta IEC}$ mice 3 days after the start of tamoxifen administration ($n \geq 4$, * $p<0.05$ by Student's t-test). **(C, D)** Representative electron micrograph of epithelial cells of the small intestine of *β-cat*$^{c.a.}$ (C) and *β-cat*$^{c.a.}$/*Stat3*$^{\Delta IEC}$ (D) mice; arrows = mitochondria undergoing cristolysis, scale bar = 1 µm. **(E)** Immunoblot analysis of phosphorylated Drp1 protein in lysates of IEC of *β-cat*$^{c.a.}$ and *β-cat*$^{c.a.}$/*Stat3*$^{\Delta IEC}$ mice 3 days after the start of tamoxifen administration. **(F, G)** Immunoblot analysis of LC3 and p62 (F) and quantification of LC3-II/LC3 conversion ratio (G) in *β-cat*$^{c.a.}$ and *β-cat*$^{c.a.}$/*Stat3*$^{\Delta IEC}$ mice 15 days after the start of tamoxifen administration. (n=2, *** $p<0.001$ by Student's t-test.)

4.4.4 *Chelation of Lysosomal Iron or Inhibition of Mitophagy Prevents LMP and T Cell Activation in vitro and in vivo*

In order to confirm the functional relevance of intralysosomal iron(II) accumulation for enhanced LMP Stat3-deficient cells, we used the iron chelator deferoxamine (DFO) known to be taken up by cells via the endocytic pathway and, therefore, primarily acts within the lysosomal compartment (Lloyd et al., 1991; Terman et al., 2006). Treatment of CMT cells with DFO prior to the H_2O_2 challenge was sufficient to prevent LMP (Figure 4.22A-I). In contrast, treatment of CMT93-cells with antimycin A or rotenone, which inhibit complex III and I of the respiratory chain, respectively, and induce mitophagy (Fang et al., 2014), prior to H_2O_2 challenge resulted in increased lysosomal iron(II) load and sensitized CMT93 cells to H_2O_2 induced LMP, which could be prevented by DFO (Fig. 4.23J-M).

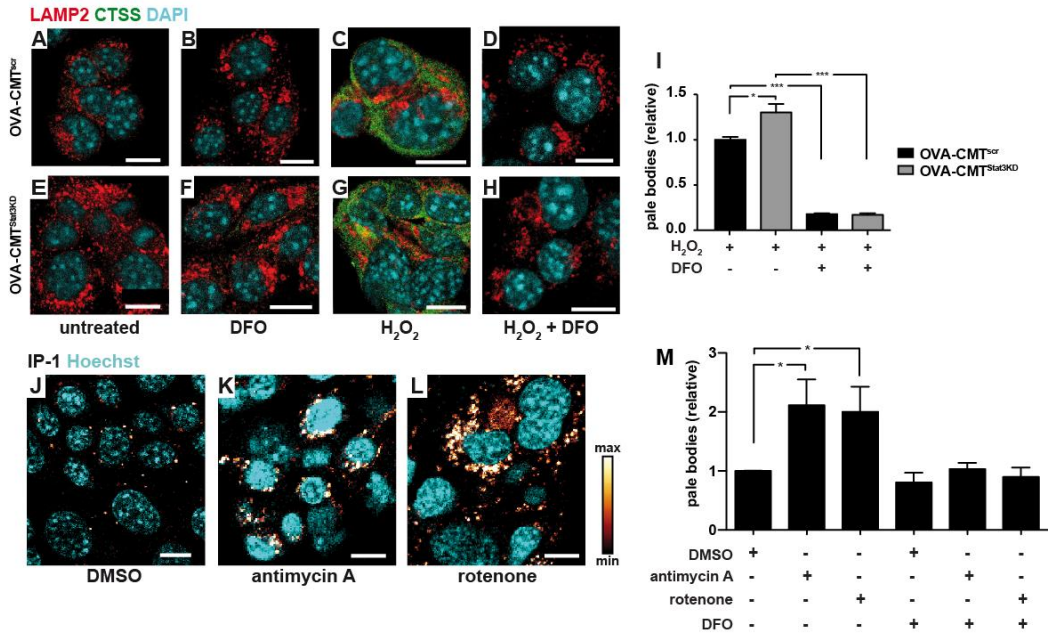

Figure 4.22: LMP is a Consequence of Mitophagy and Lysosomal Iron Accumulation. (A-H) Confocal analysis of immunostainings of OVA-CMT^{scr} (A-D) and OVA-CMT^{Stat3KD} (E-H) cells against cathepsin S (green) and the lysosomal marker LAMP2 (red) after pre-treatment with DFO (1 mM) overnight and H_2O_2 (1 mM) for 2 hours and additional incubation in conventional medium for another 6 hours as indicated. Scale bar = 10 µm. **(I)** Relative fraction of OVA-CMT^{scr} and OVA-CMT^{Stat3KD} cells with low red fluorescence upon acridine orange staining (*pale bodies*) as analyzed by flow cytometry. Where indicated cells were pretreated overnight with deferoxamine (DFO; 1 mM) and treated with H_2O_2 (1 mM) for 2 hours and analyzed after 6 additional hours cultured in conventional medium (n=4 of two independent experiments, * $p<0.05$, *** $p<0.001$ by Student's t-test). **(J-L)** Iron content of OVA-CMT cells was measured by confocal live cell microscopy and the fluorescent Fe^{2+}-specific probe IP-1 after overnight stimulation with antimycin A (100 µM) or rotenone (25 µM). The intensity of IP-1 is shown by a red-yellow LUT depicted on the right-hand side. Scale bar = 10 µm. **(M)** Relative fraction of OVA-CMT cells with low red fluorescence upon acridine orange staining (*pale bodies*) as analyzed by flow cytometry. Where indicated cells were incubated overnight with the mitophagy-inducers rotenone (25 µM) or antimycin A (100 µM) or DMSO before incubation with DFO (1 mM) and treated with H_2O_2 (1 mM) for 2 hours and analyzed after 6 additional hours cultured in conventional medium (n=6 of two independent experiments, * $p<0.05$ by Student's t-test).

In addition, RNAi-mediated gene knockdown of *Pink1*, a kinase responsible for the degradation of damaged mitochondria in the Pink1-Parkin pathway, in OVA-CMT^{Stat3KD} cells normalized lysosomal iron levels and prevented elevated IFNγ production in the OT-I co-culture system (Figure 4.23A-F). Taken together this data strongly suggests that increased LMP levels were a function of lysosomal iron and mitophagy in Stat3-deficient cells and this effect is in direct control of T cell activation *in vitro*.

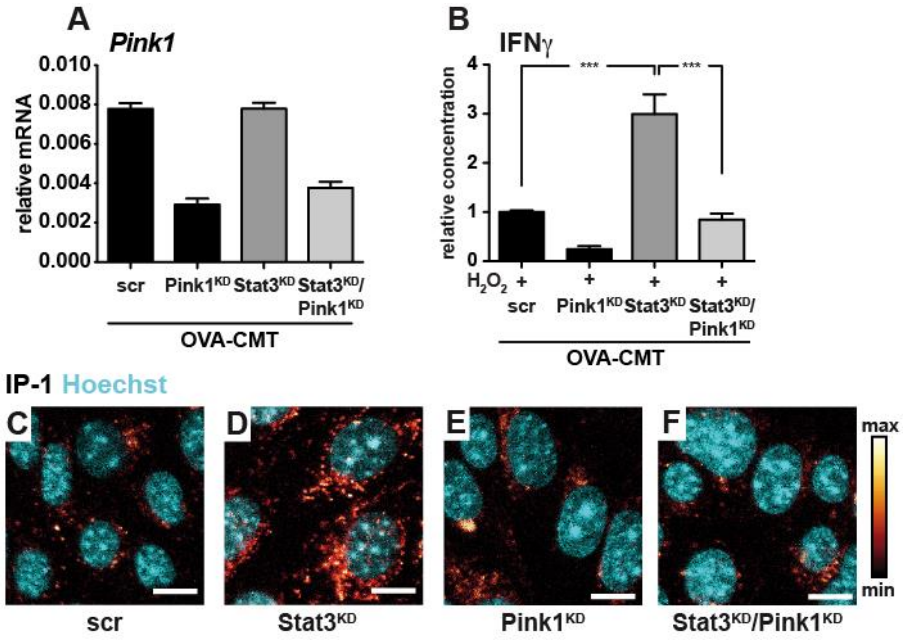

Figure 4.23: Inhibition of Mitophagy Reduces T Cell Activation and Lysosomal Iron Load. (A) OVA-CMT cells have been transfected with the indicated siRNA and analyzed 2 days later for the expression of *Pink1* (n=3 each). **(B)** IFNγ levels in supernatants of OT-I splenocytes that had been co-cultured for 48 hours with H_2O_2 stimulated OVA-CMT cells with siRNA-mediated knockdown of Pink1 and/or Stat3 genes (n=6 from 2 independent experiments, *** $p<0.001$ by Student's t-test). **(C-F)** Iron content of OVA-CMT cells was measured by confocal live cell microscopy and the fluorescent Fe^{2+}-specific probe IP-1 3 days after transfection with siRNA as indicated. The intensity of IP-1 is shown by a red-yellow LUT depicted on the right-hand side. Scale bar = 10 µm.

To confirm the contribution of lysosomal iron(II) in T cell activation *in vivo*, we performed DFO administration to *β-cat*$^{c.a.}$ and *β-cat*$^{c.a.}$/*Stat3*$^{\Delta IEC}$ mice and this treatment prevented *Ifng* upregulation in *β-cat*$^{c.a.}$/*Stat3*$^{\Delta IEC}$ mice and abrogated the survival benefit of *β-cat*$^{c.a.}$/*Stat3*$^{\Delta IEC}$ mice over control animals (Figure 4.24A, B). These findings further support the notion that accumulation of intralysosomal iron was essential for the anti-tumor cell immune phenotype observed in these animals. In contrast, pharmacological suppression of autophagy using either 3-methyladenine, an established inhibitor of autophagosome formation via the inhibition of class III PI3K (Wu et al., 2010), or genetic ablation of *Atg7* did not prevent IFNγ upregulation in lamina propria of *β-cat*$^{c.a.}$/*Stat3*$^{\Delta IEC}$ mice but instead increased it even further (Figure 4.24C, D), indicating compensation by redundant mechanisms in mitophagy.

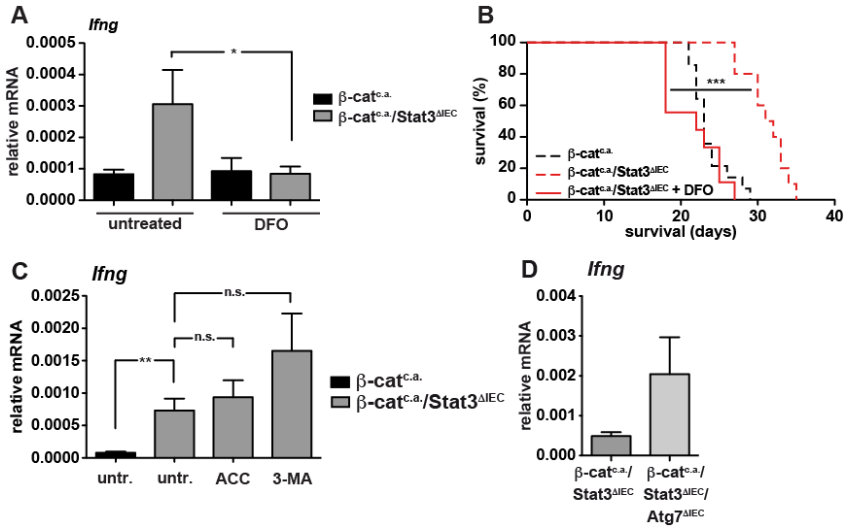

Figure 4.24: Lysosomal Iron is Required for T Cell Activation in *β-cat*$^{c.a.}$/*Stat3*$^{\Delta IEC}$ Mice. (A) Relative amount of *Ifng*-mRNA in the small intestine of *β-cat*$^{c.a.}$ and *β-cat*$^{c.a.}$/*Stat3*$^{\Delta IEC}$ mice 15 days after the start of tamoxifen administration treated with the iron-chelator DFO (400 mg/kg bodyweight) or control (n≥5, * p<0.05 by Student's t-test). **(B)** Kaplan-Meier survival curve of *β-cat*$^{c.a.}$/*Stat3*$^{\Delta IEC}$ mice (n=9) treated with DFO. Note that dashed lines have been reproduced from Fig. 1N for better comparison; *** p<0.001 by log-rank test. **(C)** Relative mRNA expression of *Ifng* in small intestinal mucosa of untreated, ACC- or 3-MA treated *β-cat*$^{c.a.}$ and *β-cat*$^{c.a.}$/*Stat3*$^{\Delta IEC}$ mice 15 days after the start of tamoxifen administration (n≥3 each). **(D)** Relative mRNA expression of *Ifng* in small intestinal mucosa of *β-cat*$^{c.a.}$/*Stat3*$^{\Delta IEC}$ and *β-cat*$^{c.a.}$/*Stat3*$^{\Delta IEC}$/*Atg7*$^{\Delta IEC}$ mice 15 days after the start of tamoxifen administration (n=3 each).

4.5 Negative Correlation of STAT3-Activation and T Cell Infiltration in Human CRC

A newly established immune score based on the gene expression levels of several key immune-related genes can efficiently predict tumor recurrence and disease-free survival in CRC patients (Fridman et al., 2012; Tosolini et al., 2011). In particular the presence of $CD8^+$ T cells and high expression levels of IFNγ are associated with a better prognosis (Figure 1.6). Therefore, we examined whether STAT3 activation was involved in the infiltration of cytotoxic T cells into cancer tissue. We analyzed a cohort of CRC specimen and found a significant inverse correlation between the accumulation of S727-phosphorylated STAT3 in cancer cells and the frequency of infiltrating $CD8^+$ T cells (Figure 4.25A-E) suggesting that

STAT3 may also be functionally involved in the suppression of $CD8^+$ T cell recruitment in human CRC.

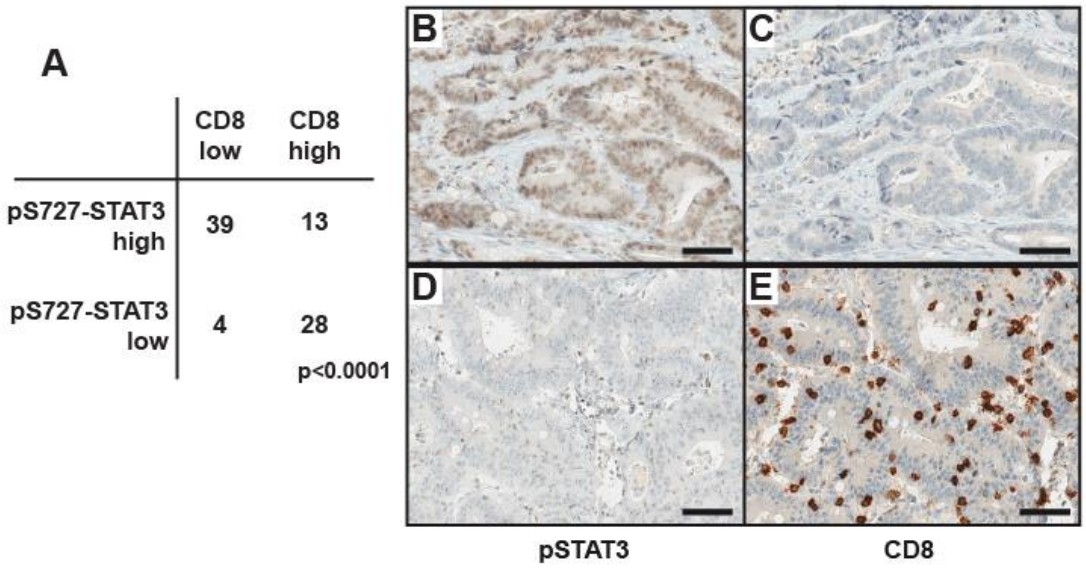

Figure 4.25: Negative Correlation between Serine-Phosphorylation of STAT3 and T Cell Infiltration in CRC Specimen. (A) Correlation of pS727-STAT3 expression and presence of $CD8^+$ T cells in human colorectal cancer (CRC, n=84; χ^2-test, p<0.0001). **(B-E)** Representative immunohistochemical analysis of pS727-STAT3 (left) and CD8 (right) in human CRC indicating inverse correlation. Scale bar = 50 µm.

5 Discussion

Cancer development depends on various biological capabilities tumor cells acquire during the multistep process of tumorigenesis, dubbed the *Hallmarks of Cancer* (Hanahan and Weinberg, 2011). These features are acquired by two so-called enabling characteristics, tumor-promoting inflammation and genome instability. The transcription factor STAT3 has been described as a key element in signal transduction of tumor-promoting inflammation (Bollrath and Greten, 2009) and we aimed to evaluate its role in a model of sporadic carcinogenesis, i.e. tumorigenesis triggered by mutagenic events following the classical pathway of colon carcinogenesis proposed by Vogelstein (Fearon and Vogelstein, 1990). We identified a previously unrecognized complex process spanning altered metabolic functions and lysosomal proteases in tumor cells and antigen-presentation and anti-tumor immunity (Figure 5.1). We have shown that increased mitochondrial turnover in response to altered energy metabolism yields an increase of lysosomal iron, thereby increasing the vulnerability of the lysosomal compartment to ROS molecules and triggering LMP. The lysosomal iron chelator DFO protected cells from lysosomal membrane permeabilization and attenuated activation of T cells *in vivo*, highlighting the causative role of lysosomal iron in LMP induction. Release of proteases into the cytoplasm as a consequence of LMP resulted in increased antigen presentation of tumor cells and triggered an effective anti-tumor response by cytotoxic T cells.

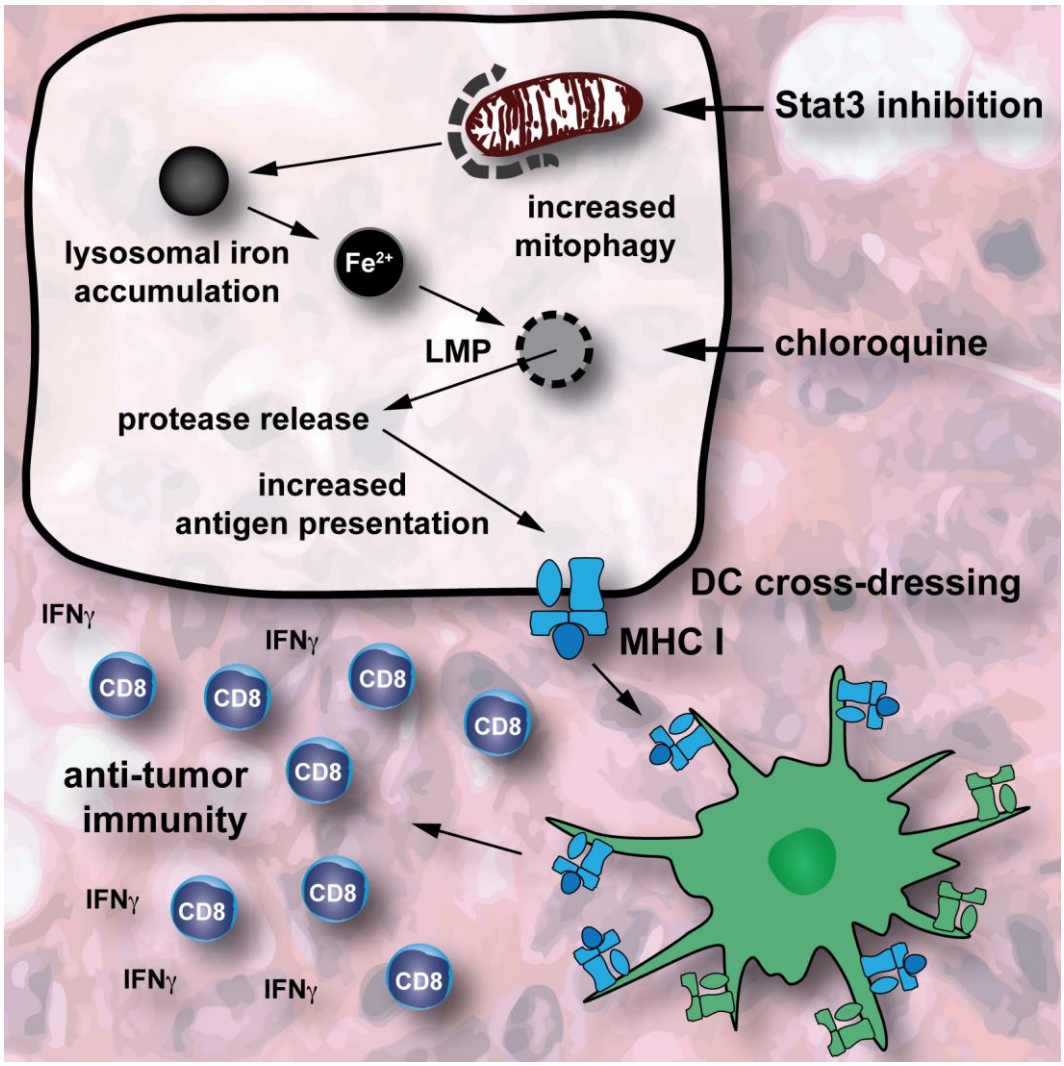

Figure 5.1: Schematic Overview. Stat3-loss or LMP-induction during early tumor development can increase antigen-processing and trigger anti-tumor adaptive immunity mediated by DC cross-dressing.

Though our study primarily focuses on the effects of STAT3 we demonstrate that chloroquine, a lysosomotropic agent known to induce LMP, can trigger this pathway in a similar way suggesting a novel role of lysosomes in regulating the immunogenicity of tumor cells. The lysosomal proteases cathepsin S and L have been linked to antigen-generation mainly in the MHC-II pathway and our experiments show that these proteases are required for antigen-processing *in vitro* using a model antigen, whereas *in vivo* their loss can be compensated. Nonetheless, using a broad-spectrum inhibitor of cysteine-proteases we demonstrate that lysosomal proteases are

responsible for antigen-generation following LMP induction in Stat3-deficient cells *in vitro* as well as *in vivo*. This finding was surprising given the numerous observations of protein-turnover by the proteasomal pathway as primary source of antigens for presentation by the MHC-I pathway. However, in order to bind to the α-chain of MHC-I a peptide needs certain chemical features such as the correct length and presence of certain anchor residues rather than cleavage by a certain protease as demonstrated before (Craiu et al., 1997). Moreover, neoantigens as the primary targets for T cells in cancer are thought to originate from novel protein sequences produced by somatic mutations in the genome of cancer cells (Schumacher and Schreiber, 2015). In our study we could detect pronounced T cell activation in the intestinal epithelium two weeks after initiating Wnt-signaling activation and Stat3 loss-of-function. This rather short time period together with the aberrant presence of lysosomal proteases within the cytoplasm raises the possibility that alterations in the protease spectrum of cancer cells could constitute an additional source of neoantigens.

In addition to TCR-stimulation the activation of T cells requires additional signals, which are most commonly supplied by DC. In recent years the transfer of antigen-MHC complexes from a so-called antigen-donor cell onto the plasma membrane of DC has been observed and termed DC cross-dressing (Nakayama, 2014; Yewdell and Haeryfar, 2005). In our experiments we have investigated whether cross-dressing can enhance the anti-tumor T cell response following LMP induction. Therefore, we have used antigen donor cells and DC from mouse strains with distinct MHC haplotypes and observed transfer of MHC-molecules from tumor cells to DC and tumor cell derived antigen-MHC-I complexes were responsible for the activation of T cells. This strongly supports DC cross-dressing as the predominant mechanism in T cell activation following Stat3-loss and LMP induction in tumor cells. Most likely,

T cells react to antigen-MHC complexes generated by the tumor cells and presented by DC that provide additional co-stimulation as suggested previously (Cerovic et al., 2015).

Interestingly, the beneficial effect of chloroquine-induced LMP in *β-cat*$^{c.a.}$ mice is much greater than benefits from loss of *Stat3* in IEC. Chloroquine can enhance human $CD8^+$ T cell responses against soluble antigens by inhibiting endosomal acidification in DC (Accapezzato et al., 2005), therefore we assume additional effects of chloroquine on DC and potentially other cell types within the intestinal mucosa further supporting survival of *β-cat*$^{c.a.}$ mice. However, these effects seem to converge on cytotoxic T cells as their depletion reverts the entire effect of chloroquine on survival.

STAT3 has been recognized as a key mediator of cancer promoting inflammation by activating the transcription of genes involved in tumor cell proliferation and survival (Bollrath and Greten, 2009). In addition, STAT3 has been suggested to confer transcription-independent functions including the regulation of mitochondrial activity (Meier and Larner, 2014). STAT3 has been found to interact with GRIM-19, a subunit of complex I of the respiratory chain and this interaction was dependent on serine-phosphorylation of STAT3 (Tammineni et al., 2013). On the functional level mitochondrial STAT3 has been associated with decreased ETC activity, mainly complex I, II and V (Gough et al., 2009; Wegrzyn et al., 2009) or complex III and IV activity (Meier and Larner, 2014). In contrast, overexpression of a constitutively active form of *Stat3* (*Stat3C*) in MEFs supports a shift from oxidative phosphorylation towards glycolysis (Warburg effect; Demaria et al., 2010) by controlling various glycolysis-associated genes on the transcriptional level together with HIF-1α. Taken together this data highlights the pleiotropic role of Stat3 in

controlling mitochondrial activity in a highly context-sensitive way and there are probably various links between nuclear and mitochondrial STAT3 in metabolic control.

Our data suggest that enhanced oxidative phosphorylation triggers mitochondrial turnover by mitophagy. Interestingly, Stat3-deficient cells harbor more mitochondria and enhanced oxidative phosphorylation than Stat3-proficient control cells. Using pulse-chase analysis we've detected increased mitochondrial turnover and, using a gene knockdown approach of the direct regulator of mitophagy *Pink1*, we have found evidence that mitophagy is directly involved in lysosomal iron accumulation and T cell activation. Whether turnover of mitochondria is simply a consequence of enhanced activity and exhaustion or mitophagy in Stat3-deficient cells is a controlled process has to be determined.

Our study has a wide range of possible clinical implications. T cells are thought to be an important contributor to future cancer therapy as demonstrated by the promising results of PD-1/PD-L1- or CTLA-4 inhibition, CAR-T cell therapy (Lim and June, 2017; Sukari et al., 2016). Our work suggests modulation of antigen processing and presentation by tumor cells as an additional therapeutic approach in cancer patients. Potential targets could be inhibition of STAT3 or STAT3-inducing kinases such as JAK1, as well as lysosomes or mitochondrial turnover, which might be easier targets for pharmacological intervention (Boya and Kroemer, 2008; de Duve et al., 1974; Villamil Giraldo et al., 2014).

6 References

Accapezzato, D., Visco, V., Francavilla, V., Molette, C., Donato, T., Paroli, M., Mondelli, M.U., Doria, M., Torrisi, M.R., and Barnaba, V. (2005). Chloroquine enhances human CD8+ T cell responses against soluble antigens in vivo. J Exp Med *202*, 817-828.

Akkari, L., Gocheva, V., Quick, M.L., Kester, J.C., Spencer, A.K., Garfall, A.L., Bowman, R.L., and Joyce, J.A. (2016). Combined deletion of cathepsin protease family members reveals compensatory mechanisms in cancer. Genes & development *30*, 220-232.

Alexandrov, L.B., Nik-Zainal, S., Wedge, D.C., Aparicio, S.A., Behjati, S., Biankin, A.V., Bignell, G.R., Bolli, N., Borg, A., Borresen-Dale, A.L., *et al.* (2013). Signatures of mutational processes in human cancer. Nature *500*, 415-421.

Anagnostou, V., Smith, K.N., Forde, P.M., Niknafs, N., Bhattacharya, R., White, J., Zhang, T., Adleff, V., Phallen, J., Wali, N., *et al.* (2017). Evolution of Neoantigen Landscape during Immune Checkpoint Blockade in Non-Small Cell Lung Cancer. Cancer Discov *7*, 264-276.

Antunes, F., Cadenas, E., and Brunk, U.T. (2001). Apoptosis induced by exposure to a low steady-state concentration of H2O2 is a consequence of lysosomal rupture. Biochem J *356*, 549-555.

Asano, T., Komatsu, M., Yamaguchi-Iwai, Y., Ishikawa, F., Mizushima, N., and Iwai, K. (2011). Distinct mechanisms of ferritin delivery to lysosomes in iron-depleted and iron-replete cells. Mol Cell Biol *31*, 2040-2052.

Au-Yeung, H.Y., Chan, J., Chantarojsiri, T., and Chang, C.J. (2013). Molecular imaging of labile iron(II) pools in living cells with a turn-on fluorescent probe. J Am Chem Soc *135*, 15165-15173.

Barker, N., van de Wetering, M., and Clevers, H. (2008). The intestinal stem cell. Genes Dev *22*, 1856-1864.

Beers, C., Burich, A., Kleijmeer, M.J., Griffith, J.M., Wong, P., and Rudensky, A.Y. (2005). Cathepsin S controls MHC class II-mediated antigen presentation by epithelial cells in vivo. J Immunol *174*, 1205-1212.

Boehm, U., Klamp, T., Groot, M., and Howard, J.C. (1997). Cellular responses to interferon-gamma. Annu Rev Immunol *15*, 749-795.

Bollrath, J. (2010). Diverse functions of Stat3 in intestinal epithelial cells during inflammation-associated and sporadic carcinogenesis. In Wissenschaftszentrum Weihenstephan für Ernährung, Landnutzung und Umwelt (München: Technische Universität).

Bollrath, J., and Greten, F.R. (2009). IKK/NF-kappaB and STAT3 pathways: central signalling hubs in inflammation-mediated tumour promotion and metastasis. EMBO Rep *10*, 1314-1319.

Bollrath, J., Phesse, T.J., von Burstin, V.A., Putoczki, T., Bennecke, M., Bateman, T., Nebelsiek, T., Lundgren-May, T., Canli, O., Schwitalla, S., *et al.* (2009). gp130-mediated Stat3 activation in enterocytes regulates cell survival and cell-cycle progression during colitis-associated tumorigenesis. Cancer Cell *15*, 91-102.

Boya, P., Gonzalez-Polo, R.A., Poncet, D., Andreau, K., Vieira, H.L., Roumier, T., Perfettini, J.L., and Kroemer, G. (2003). Mitochondrial membrane permeabilization is a critical step of lysosome-initiated apoptosis induced by hydroxychloroquine. Oncogene *22*, 3927-3936.

Boya, P., and Kroemer, G. (2008). Lysosomal membrane permeabilization in cell death. Oncogene *27*, 6434-6451.

Brand, K.A., and Hermfisse, U. (1997). Aerobic glycolysis by proliferating cells: a protective strategy against reactive oxygen species. FASEB J *11*, 388-395.

Cancer Genome Atlas, N. (2012). Comprehensive molecular characterization of human colon and rectal cancer. Nature *487*, 330-337.

Carpenter, R.L., and Lo, H.W. (2014). STAT3 Target Genes Relevant to Human Cancers. Cancers (Basel) *6*, 897-925.

Cerovic, V., Houston, S.A., Westlund, J., Utriainen, L., Davison, E.S., Scott, C.L., Bain, C.C., Joeris, T., Agace, W.W., Kroczek, R.A., *et al.* (2015). Lymph-borne CD8alpha+ dendritic cells are uniquely

able to cross-prime CD8+ T cells with antigen acquired from intestinal epithelial cells. Mucosal immunology *8*, 38-48.

Chan, T.L., Zhao, W., Leung, S.Y., Yuen, S.T., and Cancer Genome, P. (2003). BRAF and KRAS mutations in colorectal hyperplastic polyps and serrated adenomas. Cancer Res *63*, 4878-4881.

Cox, M.A., Kahan, S.M., and Zajac, A.J. (2013). Anti-viral CD8 T cells and the cytokines that they love. Virology *435*, 157-169.

Craiu, A., Gaczynska, M., Akopian, T., Gramm, C.F., Fenteany, G., Goldberg, A.L., and Rock, K.L. (1997). Lactacystin and clasto-lactacystin beta-lactone modify multiple proteasome beta-subunits and inhibit intracellular protein degradation and major histocompatibility complex class I antigen presentation. J Biol Chem *272*, 13437-13445.

Cruz, F.M., Colbert, J.D., Merino, E., Kriegsman, B.A., and Rock, K.L. (2017). The Biology and Underlying Mechanisms of Cross-Presentation of Exogenous Antigens on MHC-I Molecules. Annu Rev Immunol *35*, 149-176.

de Duve, C. (1959). Lysosomes, a new group of cytoplasmic particles in subcellular particles. In Subcellular particles; a symposium held during the meeting of the Society of General Physiologists at the Marine Biological Laboratory, Woods Hole, Massachusetts, June 9-11, 1958, T. Hayashi, ed. (New York: The Ronald Press Co.), pp. 128–159.

de Duve, C., de Barsy, T., Poole, B., Trouet, A., Tulkens, P., and Van Hoof, F. (1974). Commentary. Lysosomotropic agents. Biochemical pharmacology *23*, 2495-2531.

Decker, T., and Kovarik, P. (2000). Serine phosphorylation of STATs. Oncogene *19*, 2628-2637.

Demaria, M., Giorgi, C., Lebiedzinska, M., Esposito, G., D'Angeli, L., Bartoli, A., Gough, D.J., Turkson, J., Levy, D.E., Watson, C.J., *et al.* (2010). A STAT3-mediated metabolic switch is involved in tumour transformation and STAT3 addiction. Aging (Albany NY) *2*, 823-842.

Dolan, B.P., Gibbs, K.D., Jr., and Ostrand-Rosenberg, S. (2006). Dendritic cells cross-dressed with peptide MHC class I complexes prime CD8+ T cells. J Immunol *177*, 6018-6024.

Eaden, J.A., Abrams, K.R., and Mayberry, J.F. (2001). The risk of colorectal cancer in ulcerative colitis: a meta-analysis. Gut *48*, 526-535.

Ehrlich, P. (1909). Über den jetzigen Stand der Karzinomforschung. Nederlands Tijdschrift voor Geneeskunde *53*, 273-290.

el Marjou, F., Janssen, K.P., Chang, B.H., Li, M., Hindie, V., Chan, L., Louvard, D., Chambon, P., Metzger, D., and Robine, S. (2004). Tissue-specific and inducible Cre-mediated recombination in the gut epithelium. Genesis *39*, 186-193.

Engelhard, V.H. (1994). Structure of peptides associated with MHC class I molecules. Curr Opin Immunol *6*, 13-23.

Fang, E.F., Scheibye-Knudsen, M., Brace, L.E., Kassahun, H., SenGupta, T., Nilsen, H., Mitchell, J.R., Croteau, D.L., and Bohr, V.A. (2014). Defective mitophagy in XPA via PARP-1 hyperactivation and NAD(+)/SIRT1 reduction. Cell *157*, 882-896.

Fearon, E.R. (2011). Molecular genetics of colorectal cancer. Annu Rev Pathol *6*, 479-507.

Fearon, E.R., and Vogelstein, B. (1990). A genetic model for colorectal tumorigenesis. Cell *61*, 759-767.

Ferrington, D.A., and Gregerson, D.S. (2012). Immunoproteasomes: structure, function, and antigen presentation. Prog Mol Biol Transl Sci *109*, 75-112.

Forum, W.E. and Health, H.U.S.o.P. (2011). Prognostizierte Anzahl neuer Krebserkrankungen in reichen und armen Ländern sowie weltweit nach Krebsart im Jahr 2030 (in 1.000). Statista: https://de.statista.com/statistik/daten/studie/204611/umfrage/anzahl-neuer-krebserkrankungen-in-reichen-und-armen-laendern-nach-krebsart-2030/ (abgerufen am 14.08.2018).

Freeman, B.E., Hammarlund, E., Raue, H.P., and Slifka, M.K. (2012). Regulation of innate CD8+ T-cell activation mediated by cytokines. Proc Natl Acad Sci U S A *109*, 9971-9976.

Fridman, W.H., Galon, J., Pages, F., Tartour, E., Sautes-Fridman, C., and Kroemer, G. (2011). Prognostic and predictive impact of intra- and peritumoral immune infiltrates. Cancer Res *71*, 5601-5605.

Fridman, W.H., Pages, F., Sautes-Fridman, C., and Galon, J. (2012). The immune contexture in human tumours: impact on clinical outcome. Nature reviews *12*, 298-306.

Galon, J., Costes, A., Sanchez-Cabo, F., Kirilovsky, A., Mlecnik, B., Lagorce-Pages, C., Tosolini, M., Camus, M., Berger, A., Wind, P., *et al.* (2006). Type, density, and location of immune cells within human colorectal tumors predict clinical outcome. Science *313*, 1960-1964.

Gamrekelashvili, J., Kruger, C., von Wasielewski, R., Hoffmann, M., Huster, K.M., Busch, D.H., Manns, M.P., Korangy, F., and Greten, T.F. (2007). Necrotic tumor cell death in vivo impairs tumor-specific immune responses. J Immunol *178*, 1573-1580.

Gardner, A., and Ruffell, B. (2016). Dendritic Cells and Cancer Immunity. Trends Immunol *37*, 855-865.

Gatenby, R.A., and Gillies, R.J. (2004). Why do cancers have high aerobic glycolysis? Nat Rev Cancer *4*, 891-899.

Geissler, C., and Singh, M. (2011). Iron, meat and health. Nutrients *3*, 283-316.

Gogvadze, V., Orrenius, S., and Zhivotovsky, B. (2008). Mitochondria in cancer cells: what is so special about them? Trends Cell Biol *18*, 165-173.

Golubovskaya, V., and Wu, L. (2016). Different Subsets of T Cells, Memory, Effector Functions, and CAR-T Immunotherapy. Cancers (Basel) *8*.

Gough, D.J., Corlett, A., Schlessinger, K., Wegrzyn, J., Larner, A.C., and Levy, D.E. (2009). Mitochondrial STAT3 supports Ras-dependent oncogenic transformation. Science *324*, 1713-1716.

Greten, F.R., Eckmann, L., Greten, T.F., Park, J.M., Li, Z.W., Egan, L.J., Kagnoff, M.F., and Karin, M. (2004). IKKbeta links inflammation and tumorigenesis in a mouse model of colitis-associated cancer. Cell *118*, 285-296.

Grivennikov, S., Karin, E., Terzic, J., Mucida, D., Yu, G.Y., Vallabhapurapu, S., Scheller, J., Rose-John, S., Cheroutre, H., Eckmann, L., *et al.* (2009). IL-6 and Stat3 are required for survival of intestinal epithelial cells and development of colitis-associated cancer. Cancer Cell *15*, 103-113.

Grivennikov, S.I., Greten, F.R., and Karin, M. (2010). Immunity, inflammation, and cancer. Cell *140*, 883-899.

Groden, J., Gelbert, L., Thliveris, A., Nelson, L., Robertson, M., Joslyn, G., Samowitz, W., Spirio, L., Carlson, M., Burt, R., *et al.* (1993). Mutational analysis of patients with adenomatous polyposis: identical inactivating mutations in unrelated individuals. Am J Hum Genet *52*, 263-272.

Guermonprez, P., Valladeau, J., Zitvogel, L., Thery, C., and Amigorena, S. (2002). Antigen presentation and T cell stimulation by dendritic cells. Annu Rev Immunol *20*, 621-667.

Guinney, J., Dienstmann, R., Wang, X., de Reynies, A., Schlicker, A., Soneson, C., Marisa, L., Roepman, P., Nyamundanda, G., Angelino, P., *et al.* (2015). The consensus molecular subtypes of colorectal cancer. Nat Med *21*, 1350-1356.

Hanahan, D., and Weinberg, R.A. (2011). Hallmarks of cancer: the next generation. Cell *144*, 646-674.

Harada, N., Tamai, Y., Ishikawa, T., Sauer, B., Takaku, K., Oshima, M., and Taketo, M.M. (1999). Intestinal polyposis in mice with a dominant stable mutation of the beta-catenin gene. Embo J *18*, 5931-5942.

Heinrich, P.C., Behrmann, I., Haan, S., Hermanns, H.M., Muller-Newen, G., and Schaper, F. (2003). Principles of interleukin (IL)-6-type cytokine signalling and its regulation. Biochem J *374*, 1-20.

Hernandez, G., Thornton, C., Stotland, A., Lui, D., Sin, J., Ramil, J., Magee, N., Andres, A., Quarato, G., Carreira, R.S., *et al.* (2013). MitoTimer: a novel tool for monitoring mitochondrial turnover. Autophagy *9*, 1852-1861.

Hogquist, K.A., Jameson, S.C., Heath, W.R., Howard, J.L., Bevan, M.J., and Carbone, F.R. (1994). T cell receptor antagonist peptides induce positive selection. Cell *76*, 17-27.

Honey, K., Nakagawa, T., Peters, C., and Rudensky, A. (2002). Cathepsin L regulates CD4+ T cell selection independently of its effect on invariant chain: a role in the generation of positively selecting peptide ligands. J Exp Med *195*, 1349-1358.

Hutchins, A.P., Diez, D., and Miranda-Saavedra, D. (2013). The IL-10/STAT3-mediated anti-inflammatory response: recent developments and future challenges. Brief Funct Genomics *12*, 489-498.

Janeway, C.A., Travers, P., Walport, M., and Shlomchik, M.J. (2001). Immunobiology - The Immune System in Health and Disease, 5th edn (New York: Garland Science).

Katz, D.H., Hamaoka, T., and Benacerraf, B. (1973). Cell interactions between histoincompatible T and B lymphocytes. II. Failure of physiologic cooperative interactions between T and B lymphocytes from allogeneic donor strains in humoral response to hapten-protein conjugates. J Exp Med *137*, 1405-1418.

Kindt, T.J., Goldsby, R.A., Osborne, B.A., and Kuby, J. (2007). Kuby immunology, 6th edn (New York: W.H. Freeman).

Komatsu, M., Waguri, S., Ueno, T., Iwata, J., Murata, S., Tanida, I., Ezaki, J., Mizushima, N., Ohsumi, Y., Uchiyama, Y., *et al.* (2005). Impairment of starvation-induced and constitutive autophagy in Atg7-deficient mice. The Journal of cell biology *169*, 425-434.

Kotiadis, V.N., Duchen, M.R., and Osellame, L.D. (2014). Mitochondrial quality control and communications with the nucleus are important in maintaining mitochondrial function and cell health. Biochim Biophys Acta *1840*, 1254-1265.

Kurz, T., Terman, A., Gustafsson, B., and Brunk, U.T. (2008). Lysosomes in iron metabolism, ageing and apoptosis. Histochem Cell Biol *129*, 389-406.

Lehninger, A.L., Nelson, D.L., and Cox, M.M. (2008). Lehninger principles of biochemistry, 5th edn (New York: W.H. Freeman).

Levine, B., and Kroemer, G. (2008). Autophagy in the pathogenesis of disease. Cell *132*, 27-42.

Levy, D.E., and Lee, C.K. (2002). What does Stat3 do? J Clin Invest *109*, 1143-1148.

Li, L., Kim, S., Herndon, J.M., Goedegebuure, P., Belt, B.A., Satpathy, A.T., Fleming, T.P., Hansen, T.H., Murphy, K.M., and Gillanders, W.E. (2012). Cross-dressed CD8alpha+/CD103+ dendritic cells prime CD8+ T cells following vaccination. Proc Natl Acad Sci U S A *109*, 12716-12721.

Lim, W.A., and June, C.H. (2017). The Principles of Engineering Immune Cells to Treat Cancer. Cell *168*, 724-740.

Lin, Y., Epstein, D.L., and Liton, P.B. (2010). Intralysosomal iron induces lysosomal membrane permeabilization and cathepsin D-mediated cell death in trabecular meshwork cells exposed to oxidative stress. Invest Ophthalmol Vis Sci *51*, 6483-6495.

Linder, M.C. (2013). Mobilization of stored iron in mammals: a review. Nutrients *5*, 4022-4050.

Lloyd, J.B., Cable, H., and Rice-Evans, C. (1991). Evidence that desferrioxamine cannot enter cells by passive diffusion. Biochemical pharmacology *41*, 1361-1363.

Loschko, J., Heink, S., Hackl, D., Dudziak, D., Reindl, W., Korn, T., and Krug, A.B. (2011). Antigen targeting to plasmacytoid dendritic cells via Siglec-H inhibits Th cell-dependent autoimmunity. J Immunol *187*, 6346-6356.

Lunt, S.Y., and Vander Heiden, M.G. (2011). Aerobic glycolysis: meeting the metabolic requirements of cell proliferation. Annual review of cell and developmental biology *27*, 441-464.

Luzio, J.P., Pryor, P.R., and Bright, N.A. (2007). Lysosomes: fusion and function. Nat Rev Mol Cell Biol *8*, 622-632.

Mach, N., Gillessen, S., Wilson, S.B., Sheehan, C., Mihm, M., and Dranoff, G. (2000). Differences in dendritic cells stimulated in vivo by tumors engineered to secrete granulocyte-macrophage colony-stimulating factor or Flt3-ligand. Cancer Res *60*, 3239-3246.

Medema, J.P., and Vermeulen, L. (2011). Microenvironmental regulation of stem cells in intestinal homeostasis and cancer. Nature *474*, 318-326.

Meier, J.A., and Larner, A.C. (2014). Toward a new STATe: the role of STATs in mitochondrial function. Semin Immunol *26*, 20-28.

Mellman, I., and Steinman, R.M. (2001). Dendritic cells: specialized and regulated antigen processing machines. Cell *106*, 255-258.

Mishra, P., and Chan, D.C. (2016). Metabolic regulation of mitochondrial dynamics. The Journal of cell biology *212*, 379-387.

Mizushima, N., Yoshimori, T., and Ohsumi, Y. (2011). The role of Atg proteins in autophagosome formation. Annual review of cell and developmental biology *27*, 107-132.

Mojic, M., Takeda, K., and Hayakawa, Y. (2017). The Dark Side of IFN-gamma: Its Role in Promoting Cancer Immunoevasion. Int J Mol Sci *19*.

Monakhov, N.K., Neistadt, E.L., Shavlovskil, M.M., Shvartsman, A.L., and Neifakh, S.A. (1978). Physicochemical properties and isoenzyme composition of hexokinase from normal and malignant human tissues. J Natl Cancer Inst *61*, 27-34.

Moolenbeek, C., and Ruitenberg, E.J. (1981). The "Swiss roll": a simple technique for histological studies of the rodent intestine. Lab Anim *15*, 57-59.

Moreno-Sanchez, R., Rodriguez-Enriquez, S., Marin-Hernandez, A., and Saavedra, E. (2007). Energy metabolism in tumor cells. FEBS J *274*, 1393-1418.

Myant, K.B., Cammareri, P., McGhee, E.J., Ridgway, R.A., Huels, D.J., Cordero, J.B., Schwitalla, S., Kalna, G., Ogg, E.L., Athineos, D., *et al.* (2013). ROS production and NF-kappaB activation triggered by RAC1 facilitate WNT-driven intestinal stem cell proliferation and colorectal cancer initiation. Cell stem cell *12*, 761-773.

Nakagawa, T., Roth, W., Wong, P., Nelson, A., Farr, A., Deussing, J., Villadangos, J.A., Ploegh, H., Peters, C., and Rudensky, A.Y. (1998). Cathepsin L: critical role in Ii degradation and CD4 T cell selection in the thymus. Science (New York, NY *280*, 450-453.

Nakayama, M. (2014). Antigen Presentation by MHC-Dressed Cells. Front Immunol *5*, 672.

Ni, H.M., Williams, J.A., and Ding, W.X. (2015). Mitochondrial dynamics and mitochondrial quality control. Redox Biol *4*, 6-13.

Noffsinger, A.E. (2009). Serrated polyps and colorectal cancer: new pathway to malignancy. Annu Rev Pathol *4*, 343-364.

Parham, P. (1992). Immunology. Deconstructing the MHC. Nature *360*, 300-301.

Parham, P., Lomen, C.E., Lawlor, D.A., Ways, J.P., Holmes, N., Coppin, H.L., Salter, R.D., Wan, A.M., and Ennis, P.D. (1988). Nature of polymorphism in HLA-A, -B, and -C molecules. Proc Natl Acad Sci U S A *85*, 4005-4009.

Pavlova, N.N., and Thompson, C.B. (2016). The Emerging Hallmarks of Cancer Metabolism. Cell Metab *23*, 27-47.

Putoczki, T.L., Thiem, S., Loving, A., Busuttil, R.A., Wilson, N.J., Ziegler, P.K., Nguyen, P.M., Preaudet, A., Farid, R., Edwards, K.M., *et al.* (2013). Interleukin-11 Is the Dominant IL-6 Family Cytokine during Gastrointestinal Tumorigenesis and Can Be Targeted Therapeutically. Cancer Cell *24*, 257-271.

Rock, K.L., Farfan-Arribas, D.J., and Shen, L. (2010). Proteases in MHC class I presentation and cross-presentation. J Immunol *184*, 9-15.

Rose-John, S. (2018). Interleukin-6 Family Cytokines. Cold Spring Harb Perspect Biol *10*.

Rupar, C.A., Albo, S., and Whitehall, J.D. (1992). Rat liver lysosome membranes are enriched in alpha-tocopherol. Biochem Cell Biol *70*, 486-488.

Sandhu, U., Cebula, M., Behme, S., Riemer, P., Wodarczyk, C., Metzger, D., Reimann, J., Schirmbeck, R., Hauser, H., and Wirth, D. (2011). Strict control of transgene expression in a mouse model for sensitive biological applications based on RMCE compatible ES cells. Nucleic Acids Res *39*, e1.

Schulz, M.D., Atay, C., Heringer, J., Romrig, F.K., Schwitalla, S., Aydin, B., Ziegler, P.K., Varga, J., Reindl, W., Pommerenke, C., *et al.* (2014). High-fat-diet-mediated dysbiosis promotes intestinal carcinogenesis independently of obesity. Nature *514*, 508-512.

Schumacher, T.N., and Schreiber, R.D. (2015). Neoantigens in cancer immunotherapy. Science *348*, 69-74.

Schweizer, U., Gunnersen, J., Karch, C., Wiese, S., Holtmann, B., Takeda, K., Akira, S., and Sendtner, M. (2002). Conditional gene ablation of Stat3 reveals differential signaling requirements for survival of motoneurons during development and after nerve injury in the adult. The Journal of cell biology *156*, 287-297.

Schwitalla, S., Fingerle, A.A., Cammareri, P., Nebelsiek, T., Goktuna, S.I., Ziegler, P.K., Canli, O., Heijmans, J., Huels, D.J., Moreaux, G., *et al.* (2013a). Intestinal tumorigenesis initiated by dedifferentiation and acquisition of stem-cell-like properties. Cell *152*, 25-38.

Schwitalla, S., Ziegler, P.K., Horst, D., Becker, V., Kerle, I., Begus-Nahrmann, Y., Lechel, A., Rudolph, K.L., Langer, R., Slotta-Huspenina, J., *et al.* (2013b). Loss of p53 in enterocytes generates an inflammatory microenvironment enabling invasion and lymph node metastasis of carcinogen-induced colorectal tumors. Cancer Cell *23*, 93-106.

Sevenich, L., Hagemann, S., Stoeckle, C., Tolosa, E., Peters, C., and Reinheckel, T. (2010). Expression of human cathepsin L or human cathepsin V in mouse thymus mediates positive selection of T helper cells in cathepsin L knock-out mice. Biochimie *92*, 1674-1680.

Shen, L., Sigal, L.J., Boes, M., and Rock, K.L. (2004). Important role of cathepsin S in generating peptides for TAP-independent MHC class I crosspresentation in vivo. Immunity *21*, 155-165.

Shi, G.P., Sukhova, G.K., Kuzuya, M., Ye, Q., Du, J., Zhang, Y., Pan, J.H., Lu, M.L., Cheng, X.W., Iguchi, A., *et al.* (2003). Deficiency of the cysteine protease cathepsin S impairs microvessel growth. Circ Res *92*, 493-500.

Shi, G.P., Villadangos, J.A., Dranoff, G., Small, C., Gu, L., Haley, K.J., Riese, R., Ploegh, H.L., and Chapman, H.A. (1999). Cathepsin S required for normal MHC class II peptide loading and germinal center development. Immunity *10*, 197-206.

Singh, N.J. (2016). Self-reactivity as the necessary cost of maintaining a diverse memory T-cell repertoire. Pathog Dis *74*.

Som, P., Atkins, H.L., Bandoypadhyay, D., Fowler, J.S., MacGregor, R.R., Matsui, K., Oster, Z.H., Sacker, D.F., Shiue, C.Y., Turner, H., *et al.* (1980). A fluorinated glucose analog, 2-fluoro-2-deoxy-D-glucose (F-18): nontoxic tracer for rapid tumor detection. J Nucl Med *21*, 670-675.

Sukari, A., Nagasaka, M., Al-Hadidi, A., and Lum, L.G. (2016). Cancer Immunology and Immunotherapy. Anticancer Res *36*, 5593-5606.

Takeda, K., Kaisho, T., Yoshida, N., Takeda, J., Kishimoto, T., and Akira, S. (1998). Stat3 activation is responsible for IL-6-dependent T cell proliferation through preventing apoptosis: generation and characterization of T cell-specific Stat3-deficient mice. J Immunol *161*, 4652-4660.

Tammineni, P., Anugula, C., Mohammed, F., Anjaneyulu, M., Larner, A.C., and Sepuri, N.B. (2013). The import of the transcription factor STAT3 into mitochondria depends on GRIM-19, a component of the electron transport chain. J Biol Chem *288*, 4723-4732.

Tanaka, T., Kohno, H., Suzuki, R., Yamada, Y., Sugie, S., and Mori, H. (2003). A novel inflammation-related mouse colon carcinogenesis model induced by azoxymethane and dextran sodium sulfate. Cancer science *94*, 965-973.

Terman, A., Kurz, T., Gustafsson, B., and Brunk, U.T. (2006). Lysosomal labilization. IUBMB Life *58*, 531-539.

Tholen, M., Hillebrand, L.E., Tholen, S., Sedelmeier, O., Arnold, S.J., and Reinheckel, T. (2014). Out-of-frame start codons prevent translation of truncated nucleo-cytosolic cathepsin L in vivo. Nat Commun *5*, 4931.

Thommen, D.S., and Schumacher, T.N. (2018). T Cell Dysfunction in Cancer. Cancer Cell *33*, 547-562.

Tomasetti, C., Li, L., and Vogelstein, B. (2017). Stem cell divisions, somatic mutations, cancer etiology, and cancer prevention. Science *355*, 1330-1334.

Toor, A.A., Toor, A.A., Rahmani, M., and Manjili, M.H. (2016). On the organization of human T-cell receptor loci: log-periodic distribution of T-cell receptor gene segments. J R Soc Interface *13*, 20150911.

Tosolini, M., Kirilovsky, A., Mlecnik, B., Fredriksen, T., Mauger, S., Bindea, G., Berger, A., Bruneval, P., Fridman, W.H., Pages, F., *et al.* (2011). Clinical impact of different classes of infiltrating T cytotoxic and helper cells (Th1, th2, treg, th17) in patients with colorectal cancer. Cancer Res *71*, 1263-1271.

Tran Janco, J.M., Lamichhane, P., Karyampudi, L., and Knutson, K.L. (2015). Tumor-infiltrating dendritic cells in cancer pathogenesis. J Immunol *194*, 2985-2991.

Turk, B., and Turk, V. (2009). Lysosomes as "suicide bags" in cell death: myth or reality? J Biol Chem *284*, 21783-21787.

Turk, V., Turk, B., and Turk, D. (2001). Lysosomal cysteine proteases: facts and opportunities. EMBO J *20*, 4629-4633.

Urlinger, S., Baron, U., Thellmann, M., Hasan, M.T., Bujard, H., and Hillen, W. (2000). Exploring the sequence space for tetracycline-dependent transcriptional activators: novel mutations yield expanded range and sensitivity. Proc Natl Acad Sci U S A *97*, 7963-7968.

Van Kaer, L., Ashton-Rickardt, P.G., Ploegh, H.L., and Tonegawa, S. (1992). TAP1 mutant mice are deficient in antigen presentation, surface class I molecules, and CD4-8+ T cells. Cell *71*, 1205-1214.

Vander Heiden, M.G., Cantley, L.C., and Thompson, C.B. (2009). Understanding the Warburg effect: the metabolic requirements of cell proliferation. Science *324*, 1029-1033.

Verdegaal, E.M., de Miranda, N.F., Visser, M., Harryvan, T., van Buuren, M.M., Andersen, R.S., Hadrup, S.R., van der Minne, C.E., Schotte, R., Spits, H., *et al.* (2016). Neoantigen landscape dynamics during human melanoma-T cell interactions. Nature *536*, 91-95.

Villamil Giraldo, A.M., Appelqvist, H., Ederth, T., and Ollinger, K. (2014). Lysosomotropic agents: impact on lysosomal membrane permeabilization and cell death. Biochemical Society transactions *42*, 1460-1464.

Vogelstein, B., Fearon, E.R., Hamilton, S.R., Kern, S.E., Preisinger, A.C., Leppert, M., Nakamura, Y., White, R., Smits, A.M., and Bos, J.L. (1988). Genetic alterations during colorectal-tumor development. N Engl J Med *319*, 525-532.

Voskoboinik, I., Whisstock, J.C., and Trapani, J.A. (2015). Perforin and granzymes: function, dysfunction and human pathology. Nat Rev Immunol *15*, 388-400.

Wakim, L.M., and Bevan, M.J. (2011). Cross-dressed dendritic cells drive memory CD8+ T-cell activation after viral infection. Nature *471*, 629-632.

Wang, J., and Pantopoulos, K. (2011). Regulation of cellular iron metabolism. Biochem J *434*, 365-381.

Wang, T., Niu, G., Kortylewski, M., Burdelya, L., Shain, K., Zhang, S., Bhattacharya, R., Gabrilovich, D., Heller, R., Coppola, D., *et al.* (2004). Regulation of the innate and adaptive immune responses by Stat-3 signaling in tumor cells. Nat Med *10*, 48-54.

Warburg, O. (1956). On respiratory impairment in cancer cells. Science *124*, 269-270.

Warburg, O., Poesner, K., and Negelein, E. (1924). On the Metabolism of Carcinoma Cells. Biochemische Zeitschrift, 309-344.

Wegrzyn, J., Potla, R., Chwae, Y.J., Sepuri, N.B., Zhang, Q., Koeck, T., Derecka, M., Szczepanek, K., Szelag, M., Gornicka, A., *et al.* (2009). Function of mitochondrial Stat3 in cellular respiration. Science *323*, 793-797.

Wei, H., Kim, S.J., Zhang, Z., Tsai, P.C., Wisniewski, K.E., and Mukherjee, A.B. (2008). ER and oxidative stresses are common mediators of apoptosis in both neurodegenerative and non-neurodegenerative lysosomal storage disorders and are alleviated by chemical chaperones. Hum Mol Genet *17*, 469-477.

WHO (2014a). Anteil der häufigsten Krebsarten an der weltweiten Zahl der Krebstodesfälle im Jahr 2012 (Häufigkeitsverteilung). Statista: https://de.statista.com/statistik/daten/studie/286575/umfrage/anteil-der-haeufigsten-krebsarten-an-der-weltweiten-zahl-der-krebstodesfaellen/ (abgerufen am 14.08.2018).

WHO (2014b). Zahl der Krebsneuerkrankungen weltweit nach Krebsart im Jahr 2012. Statista: https://de.statista.com/statistik/daten/studie/286545/umfrage/zahl-der-krebsneuerkrankungen-weltweit/ (abgerufen am 14.08.2018).

WHO (2014c). Zahl der Krebstodesfälle weltweit nach Krebsart im Jahr 2012. Statista: https://de.statista.com/statistik/daten/studie/286584/umfrage/zahl-der-krebstodesfaelle-nach-krebsart-weltweit/ (abgerufen am 14.08.2018).

Williams, T.M. (2001). Human leukocyte antigen gene polymorphism and the histocompatibility laboratory. J Mol Diagn *3*, 98-104.

Willimsky, G., and Blankenstein, T. (2005). Sporadic immunogenic tumours avoid destruction by inducing T-cell tolerance. Nature *437*, 141-146.

Willimsky, G., Czeh, M., Loddenkemper, C., Gellermann, J., Schmidt, K., Wust, P., Stein, H., and Blankenstein, T. (2008). Immunogenicity of premalignant lesions is the primary cause of general cytotoxic T lymphocyte unresponsiveness. J Exp Med *205*, 1687-1700.

Wu, Y.T., Tan, H.L., Shui, G., Bauvy, C., Huang, Q., Wenk, M.R., Ong, C.N., Codogno, P., and Shen, H.M. (2010). Dual role of 3-methyladenine in modulation of autophagy via different temporal patterns of inhibition on class I and III phosphoinositide 3-kinase. J Biol Chem *285*, 10850-10861.

Yang, S., Farraye, F.A., Mack, C., Posnik, O., and O'Brien, M.J. (2004). BRAF and KRAS Mutations in hyperplastic polyps and serrated adenomas of the colorectum: relationship to histology and CpG island methylation status. Am J Surg Pathol *28*, 1452-1459.

Yewdell, J.W., and Haeryfar, S.M. (2005). Understanding presentation of viral antigens to CD8+ T cells in vivo: the key to rational vaccine design. Annu Rev Immunol *23*, 651-682.

Yewdell, J.W., Reits, E., and Neefjes, J. (2003). Making sense of mass destruction: quantitating MHC class I antigen presentation. Nat Rev Immunol *3*, 952-961.

York, I.A., and Rock, K.L. (1996). Antigen processing and presentation by the class I major histocompatibility complex. Annu Rev Immunol *14*, 369-396.

Youle, R.J., and Narendra, D.P. (2011). Mechanisms of mitophagy. Nat Rev Mol Cell Biol *12*, 9-14.

Zhang, Y., Mikhael, M., Xu, D., Li, Y., Soe-Lin, S., Ning, B., Li, W., Nie, G., Zhao, Y., and Ponka, P. (2010). Lysosomal proteolysis is the primary degradation pathway for cytosolic ferritin and cytosolic ferritin degradation is necessary for iron exit. Antioxid Redox Signal *13*, 999-1009.

Ziegler, P.K., and Greten, F.R. (2015). Übersicht – Zelluläre und molekulare Grundlagen des Kolonkarzinoms. TumorDiagnostik & Therapie *36*, 446-449.

Zinkernagel, R.M., and Doherty, P.C. (1974). Restriction of in vitro T cell-mediated cytotoxicity in lymphocytic choriomeningitis within a syngeneic or semiallogeneic system. Nature *248*, 701-702.

Zong, J., Keskinov, A.A., Shurin, G.V., and Shurin, M.R. (2016). Tumor-derived factors modulating dendritic cell function. Cancer Immunol Immunother *65*, 821-833.

7 Acknowledgment

If I have seen further it is by standing on the shoulders of giants.
Isaac Newton

The work presented here would not have been possible without the unconditional support of my supervisor Professor Florian Greten. His keen sense for this project, his continuous guidance and constructive criticism not only made this work possible but, moreover, taught me how to think and work in a scientific way. I will benefit from that outstanding education over my lifetime, I'm convinced.

In addition, I am very grateful to the members of my PhD-committee, Professors Bernhard Holzmann and Thomas Korn. Their precious suggestions were a key determinant of success in this work.

I'd like to thank to my fellow colleagues in the laboratory in Munich and Frankfurt, most notably Özge Canlı, Tiago De Oliveira, Julia Bollrath, Charles Pallangyo, Michaela Diamanti, Mallika Ramakrishnan, Fatih Ceteci, Birgit Ritter, Jalaj Gupta, Julia Varga, Sarah Schwitalla, Marina Pesic, Claire Conche, Verawan Boonsanay-Michel, Çiğdem Atay, Olga Goncharova, Arun Mankan, Franziska Romrig, Manon Schulz, Jessica Heringer and more, who constantly supported my work with valuable suggestions or generous help with experimental work.

This work greatly benefited from excellent technical assistance by Kerstin Burmeister, Kristin Retzlaff, Kathleen Mohs, Natalia Delis, Tefik Merovci, Hana Kunkel, Eva Rudolf, Preeti Gupta, Saskia Ettl, Semra Ceteci and Petra Dinse, whose contribution is gratefully acknowledged.

I am grateful to the scientific community at the Georg-Speyer-Haus, especially Stefan Stein, Lisa Sevenich, M. Canan Arkan, Ursula Dietrich, Professor Winfried Wels, Madina Karimova, Hind Medyouf, Henner Farin, Professor Daniela Krause, Herbert Kühnel, Nina Müller and Boris Brill, who supported my project with helpful

discussion, valuable suggestions and material. Furthermore, they continuously create a welcoming atmosphere for scientists of all stages of education and enable their work.

Furthermore, I enjoyed great collaboration with several external partners, including Professor Matthias Ernst, Tracy Putoczki, Professor David Horst, Stefan Dröse, Professor Dagmar Wirth, Professor Tim F. Greten, Jaba Gamrekelashvili, Professor Thomas Reinheckel, Professor Emmanouil Fokas, Professor Andrew C. Larner, Professor Thomas Blankenstein, Julia Slotta-Huspenina, Susanna Müller, Professor Chris Chang, Gene Dubowchik, Takaji Matsutani and Professor Josef Müller-Höcker, who contributed valuable discussion or material to my study.

I also like to thank my new colleagues at Senckenberg Institute of Pathology of the University of Frankfurt, Professor Peter J. Wild, Professor Hans-Michael Kvasnicka, Falko Schulze, Verena Tischler, Lisa Völkl, Professor Sylvia Hartmann, Kati Kiil, Kevin Smith, and many more, who greatly supported my transition to my new position and provide an inspiring environment for my specialist medical training.

In addition, I'd like to thank my academic mentors Professor Bruno Luckow, Florian Horn, Professor Anne Krug, Roger Vogelmann, Philipp Jost, Professor Jürgen Schlegel, Professor Claudia Traidl-Hoffmann, Professor Alois Moosmüller and others, who contributed to my medical and personal education.

I am especially grateful for the continuous support by my beloved wife, M. Gülfem Öner-Ziegler. Her love and encouragement greatly contributed to the success of this project and I dedicate this work to her.

In addition, for my lifetime I greatly profit from the ongoing support of my family, foremost my parents Christine and Ernst Ziegler and my grandmother Maria Harrer. Their help in all aspects of life made my education possible.

8 Publication List

Peer Reviewed Scientific Articles

1. Ziegler, P. K., Bollrath, J., Pallangyo, C. K., Matsutani, T., Canli, Ö., De Oliveira, T., ...Greten, F. R. (2018). Mitophagy in Intestinal Epithelial Cells Triggers Adaptive Immunity during Tumorigenesis. **Cell** 174(1), 88–101.
2. Pallangyo, C.K., Ziegler, P.K., and Greten, F.R. (2015). IKKbeta acts as a tumor suppressor in cancer-associated fibroblasts during intestinal tumorigenesis. **The Journal of experimental medicine** *212*, 2253-2266.
3. Rokavec, M., Oner, M.G., Li, H., Jackstadt, R., Jiang, L., Lodygin, D., Kaller, M., Horst, D., Ziegler, P.K., Schwitalla, S., … Hermeking, H. (2014). IL-6R/STAT3/miR-34a feedback loop promotes EMT-mediated colorectal cancer invasion and metastasis. **The Journal of clinical investigation** *124*, 1853-1867.
4. Schulz, M.D., Atay, C., Heringer, J., Romrig, F.K., Schwitalla, S., Aydin, B., Ziegler, P.K., Varga, J., Reindl, W., Pommerenke, C., … Arkan, M.C. (2014). High-fat-diet-mediated dysbiosis promotes intestinal carcinogenesis independently of obesity. **Nature** *514*, 508-512.
5. Putoczki, T.L., Thiem, S., Loving, A., Busuttil, R.A., Wilson, N.J., Ziegler, P.K., Nguyen, P.M., Preaudet, A., Farid, R., Edwards, K.M., … Ernst, M. (2013). Interleukin-11 Is the Dominant IL-6 Family Cytokine during Gastrointestinal Tumorigenesis and Can Be Targeted Therapeutically. **Cancer Cell** *24*, 257-271.
6. Schwitalla, S., Fingerle, A.A., Cammareri, P., Nebelsiek, T., Goktuna, S.I., Ziegler, P.K., Canli, O., Heijmans, J., Huels, D.J., Moreaux, G., ...Greten, F. R. (2013a). Intestinal tumorigenesis initiated by dedifferentiation and acquisition of stem-cell-like properties. **Cell** *152*, 25-38.
7. Schwitalla, S., Ziegler, P.K., Horst, D., Becker, V., Kerle, I., Begus-Nahrmann, Y., Lechel, A., Rudolph, K.L., Langer, R., Slotta-Huspenina, J., ...Greten, F. R. (2013b). Loss of p53 in enterocytes generates an inflammatory microenvironment enabling invasion and lymph node metastasis of carcinogen-induced colorectal tumors. **Cancer Cell** *23*, 93-106.
8. Mankan, A.K., Canli, O., Schwitalla, S., Ziegler, P., Tschopp, J., Korn, T., and Greten, F.R. (2011). TNF-alpha-dependent loss of IKKbeta-deficient myeloid progenitors triggers a cytokine loop culminating in granulocytosis. **Proceedings of the National Academy of Sciences of the United States of America** *108*, 6567-6572.

Review Article

1. Ziegler, P.K., and Greten, F.R. (2015). Zelluläre und molekulare Grundlagen des Kolonkarzinoms. **TumorDiagnostik & Therapie** *36*, 446-449.

Book Chapters

1. Paul Ziegler: Die Niere; in: Biochemie des Menschen, Florian Horn, et al.; 6. Aufl. 2015; Thieme, Stuttgart.
2. Paul Ziegler: Der Säure-Basen-Haushalt; in: Biochemie des Menschen, Florian Horn, et al.; 6. Aufl. 2015; Thieme, Stuttgart.
3. Paul Ziegler: DNA-Seqenzierung; in: Biochemie des Menschen, Florian Horn, et al.; 6. Aufl. 2015; Thieme, Stuttgart.